TR diss
2826 3

Stellingen

behorende bij het proefschrift:

Hydrogen and helium in selected fusion reactor materials

1. De voorspelling van Kögel et al. dat helium dissocieert van vacatures in Nb (groep 5-metaal) bij 990 K (bij een uitgloeitempo van 0.011 K/s), gebaseerd op de helium desorptie analogie bij Mo (groep 6-metaal) blijkt onjuist.

   G. Kögel, P. Sperr, J. Strömer en W. Trifthäuser, Condens. Matter ***5*** *(1993) 3987 en hoofdstuk 7 van dit proefschrift.*

2. De waarden 1.3 (±0.3) eV en 1.2 (±0.3) eV voor de migratie-energie van vacatures in vanadium die respectievelijk zijn bepaald door Maier et al. en Janot et al. zijn minstens 0.5 eV te hoog.

   K. Maier, M.Peo, B. Saile, H.E. Schaefer en A. Seeger, Phil. Mag ***A40*** *(1979) 701, C. Janot, B. George en P. Delcroix, J. Phys.* ***F12*** *(1982) 47 en hoofdstuk 7 van dit proefschrift.*

3. Waterstofgasdesorptie is een geschikte methode om op niet-destructieve wijze vacatureclusters en microholten aan te tonen in metalen.

   Dit proefschrift

4. Door het uitvoeren van een permeatiestudie in wolfraam met behulp van 3 keV D_3^+ ionen is het wel degelijk mogelijk dat defecten gecreëerd worden, in tegenstelling tot de verwachting van Anderl et al. Dit kan verklaard worden door energie-overdracht via een intermediaire botsing met zuurstof ($D \rightarrow O \rightarrow W$).

   R.A. Anderl, D.F. Holland, G.R. Longhurst, R.J. Pawelko, C.L. Trybus and C.H. Sellers, Fusion Technology ***21*** *(1992) 745 en hoofdstuk 4 van dit proefschrift.*

5. De energieën van een waterstofatoom in een vacature en aan het buitenoppervlak van een kristal komen overeen, aangezien het waterstofatoom een specifieke elektronendichtheid opzoekt dichtbij een metaalatoom. Dit gaat niet op in het geval van wolfraam.

P. Nordlander, J.K. Nørskov en F. Besenbacher, J. Phys. ***F16*** *(1986) 1161 en hoofdstukken 3,4 en 5 van dit proefschrift.*

6. Het verdient aanbeveling om in Nederland meer aandacht te besteden aan warmtetransportsystemen gebaseerd op waterstof-adsorptie en -desorptie. Hiermee kan de industriële restwarmte op zeer efficiënte wijze over tientallen kilometers getransporteerd worden.

   I. Fuijiwara et al., International Symposium on Metal Hydrogen Systems, Les Diablerets, Zwitserland, augustus 25-30, 1996.

7. Voor het modelleren van de ozonconcentratie op leefniveau is de terreinhoogte-parameter een zeer belangrijke factor. Het verdient dan ook de aanbeveling deze nader te onderzoeken.

   H. Eleveld, E.J.J. Kirchner, J.P. Beck, F.A.A.M. de Leeuw en W.A.J. van Pul, RIVM-rapport nr. 722401010.

8. Lokale NO_x-emissies verlagen de ozonconcentratie*. In het geval van smog-episodes is het dus aan te bevelen om het verkeer niet stil te leggen.

   **F.A.A.M. de Leeuw, Nationale Milieuverkenning 2, RIVM (1991) 167.*

9. Door het toepassen van processen bij de olieraffinaderijen die gericht zijn op het verminderen van de NO_x- en SO_2-emissies neemt de uitstoot van het broeikasgas CO_2 sterk toe.

   P. Ladeur en H. Bijwaard, Oil&Gas Journal (26 apr. 1993) 64.

10. Het is onjuist te veronderstellen dat in de toekomst het wereldrecord bij de vrouwen beter zou zijn dan dat bij de mannen op een willekeurige loopafstand. Door het verkeerd toepassen van een extrapolatie van de ontwikkeling van de atletiekwereldrecords meenden Whipp en Ward dat te kunnen concluderen.

    B.J. Whipp en S.A. Ward, Nature ***355*** *(1992) 25.*

11. Beleidsmatig gezien is het verstandig om te geloven in het versterkt broeikaseffect. Of het wetenschappelijk juist is, valt nog te bezien.

Harry Eleveld oktober 1996.

TR diss
2826

Hydrogen and helium in selected fusion reactor materials

H. Eleveld

CIP-GEGEVENS KONINKLIJKE BIBLIOTHEEK, DEN HAAG

Eleveld, Harm

Hydrogen and helium in selected fusion reactor materials /
Harry Eleveld. - Delft : Interfacultair Reactor Instituut,
Technische Universiteit Delft. - I11.
Proefschrift Technische Universiteit Delft - Met lit. opg. -
Met samenvatting in het Nederlands.
ISBN 90-73861-44-6
NUGI 812
Trefw.: materiaalonderzoek; waterstof; helium; wolfraam; vanadium; beryllium.

Copyright © 1996 by H. Eleveld

Hydrogen and helium in selected fusion reactor materials

PROEFSCHRIFT

ter verkrijging van de graad van doctor
aan de Technische Universiteit Delft,
op gezag van de Rector Magnificus Prof. ir. K.F. Wakker,
in het openbaar te verdedigen ten overstaan van een commissie,
door het College van Dekanen aangewezen,
op donderdag 31 oktober 1996 te 10.30 uur
door

Harm ELEVELD

BIBLIOTHEEK TECHNISCH

doctorandus in de natuurkunde
geboren te Veendam

Dit proefschrift is goedgekeurd door de promotoren:
Prof. dr. A. van Veen
Prof. dr. ir. H. van Dam

Samenstelling promotiecommissie:

Rector Magnificus,	voorzitter
Prof. dr. A. van Veen,	TU Delft, promotor
Prof. dr. ir. H. van Dam,	TU Delft, promotor
Prof. dr. ir. F. Tuinstra,	TU Delft
Prof. dr. ir. A. van den Beukel,	TU Delft
Dr. B.J. Thijsse,	TU Delft
Prof. dr. J. Th. M. de Hosson,	RU Groningen
Dr. J.H. Evans,	Royal Holloway University of London, U.K.

aan Mary-Anne en Daan,
aan mijn ouders.

Table of contents

1. Introduction 19
1.1 Nuclear fusion reactors 19
1.2 Selected fusion reactor materials 23
1.2.1 Tungsten 23
1.2.2 Beryllium 24
1.2.3 Vanadium 25
1.3 Developed and employed techniques 26

2. Experimental methods for gas-defect studies 29
2.1 Introduction 29
2.2 The thermal gas desorption spectrometers, a technical description 30
2.2.1 Vacuum chamber, UHV pumps and baking 30
2.2.2 The applied target holder and design and construction of a new target holder 33
2.2.3 Ion sources and gas supply 36
2.2.4 Auger electron spectroscopy and the EELS option 44
2.3 Thermal desoprtion calibration methods and control of surface coverage 47
2.3.1 Calibration for helium 47
2.3.2 Calibration for hydrogen 47
2.3.3 Effects of the angular distribution of desorbed particles on the detection sensitivity 48
2.3.4 Gas coverage control 50
2.4 Other analysis 51
2.4.1 Positron annihilation 51
2.4.2 Neutron depth profiling 53
2.5 Sample preparation 55
2.5.1 Tungsten 55
2.5.2 Beryllium 58
2.5.3 Vanadium and niobium 58

3. Modelling of hydrogen desorption from defects in metals 63
3.1 Introduction 63
3.2 Hydrogen defect interactions 64
3.3 Diffusion and rate theory 67

3.4 Chemisorbed and molecular hydrogen in microcavities 70
3.5 Results of model calculations 72
3.6 Discussion 78

4. Hydrogen, nitrogen and carbon interactions with the surface and point defects in tungsten 81
4.1 Introduction 81
4.2 Deuterium adsorption experiments 82
4.3 Vacancy type defects, clean and oxygen covered surfaces 86
4.4 Model for deuterium desorption from subsurface defects 90
4.5 Simulations of the adsorption and low energy D_2 irradiation experiments 92
4.6 Vacancy type defects, nitrogen covered surfaces 96
4.6.1 Nitrogen desorption 96
4.6.2 Deuterium desorption from nitrogen covered surfaces ... 97
4.7 N-V dissociation 99
4.8 C-V dissociation 101
4.9 Conclusions 104

5. Vacancy cluster growth in tungsten 109
5.1 Introduction 109
5.2 Hydrogen interaction with voids, surface impurity coverage related trapping 109
5.3 Positron annihilation experiments 115
5.4 Results of atomistic calculations on vacancy clusters 116
5.5 Nitrogen filled vacancy clusters 116
5.6 Deuterium interactions with helium bubbles 119
5.7 Deuterium interactions with defects using diffusional rate theory 122
5.8 Discussion 125
5.9 Conclusions 129

6. Helium interaction with beryllium 133
6.1 Introduction 133
6.2 Experimental 133
6.3 THDS results of helium irradiated beryllium 135
6.4 Neutron depth profiling results of post irradiation anneals 137
6.5 Scanning electron microscopy results 140

6.6 Positron annihilation results of post-irradiation anneals 142
6.7 Discussion 143
6.8 Conclusions 145

7. Helium interaction with V and Nb 149
7.1 Introduction 149
7.2 Energy considerations of the He-O-V(/Nb) system 150
7.3 Vanadium 151
7.3.1 Dose variation of 1 keV helium 151
7.3.2 Helium energy variation 154
7.3.3 Helium filling of vacancies produced by 1 keV He^+ 156
7.3.4 Annihilation of vacancy type defects by self-interstitial implantation 157
7.3.5 Impurity delayed vacancy migration 157
7.3.6 Results of irradiation at temperatures ranging from 115 to 700 K 159
7.3.7 Vacancy mobility in vanadium 161
7.3.8 Ne, Ar and Kr irradiation of the vanadium crystal 162
7.4 Niobium 164
7.4.1 Helium in monovacancies 164
7.4.2 Oxygen migration and OV dissociation in niobium 165
7.5 Conclusions 166

Summary 171
Samenvatting 175
Nawoord 179
Curriculum vitae 181

List of publications related to this thesis

[1] H. Eleveld, A.T. Dijksman and A. van Veen, *The release of deuterium from clean and impurity covered tungsten,* Proc. 16th Symp. on Fusion Technology (SOFT, London, 1990, Eds. B.E. Keen, M. Huguet, R. Hemsworth, Elsevier Science Publishers BV), 376-380.

[2] H. Eleveld and A. van Veen, *Deuterium interaction with impurities in tungsten studied with TDS,* J. Nucl. Mater. **191-194** (1992) 433-438.

[3] H. Eleveld and A. van Veen, *Void growth and thermal desorption of deuterium from voids in tungsten,* J. Nucl. Mater. **212-215** (1994) 1421-1425.

[4] H. Eleveld, A. van Veen, F. Labohm and M.W. de Moor, *Thermal desorption of helium irradiated beryllium studied by THDS, NDP, PA and SEM,* J. Nucl. Mater. **212-215** (1994) 971-975.

[5] H. Eleveld, A. van Veen, M. Clement and M. de Moor, *Helium defect interactions in vanadium and beryllium,* Plasma Devices and Operations **3**, (1994) 65-78.

[6] A. van Veen, H. Eleveld and M. Clement, *Helium impurity interactions in vanadium and niobium,* J. Nucl. Mater. **212-215** (1994) 287-292.

[7] A. van Veen, H. Eleveld, J. Partanen, F. Labohm and H. Schut, *Thermal annealing of light ion irradiated tungsten and beryllium,* Mat. Sci. For. **175-178** (1995) 229.

List of publications

Chapter 1

Introduction

1.1 Nuclear fusion reactors

Magnetic fusion is a possible option to supplement known energy-sources. The current resources can be used until the middle of the next century. When fusion of light elements becomes economically achievable, the oceans will supply the fuel. It is clearly important to continue research on sustainable resources, because of environmental point of view.

One of the possibilities lies in laser fusion, with its origins in the American weapon industry. Now that the veil of secrecy has been lifted this can be a potential candidate as a fusion reactor [1,2]. Magnetic confinement of plasmas is an option that has been investigated for about four decades. World wide there are many experimental fusion reactors. The three largest tokamaks are Joint European Torus (JET) at Culham, UK [3], The Princeton University's (USA) Tokamak Fusion Test Reactor (TFTR) [4], and JT-60 (Japan) [5]. All three have reached conditions near break-even.

JET achieved its goals set in 1975 [6], with reactor relevant temperatures (up to 30 keV), densities (up to $4x10^{20}$ m^{-3}) and energy confinement times (up to 1.7 s) in different plasma discharges [7]. In November 1991, the experiments culminated in the JET Preliminary Tritium Experiment (PTE). In this experiment, during 2 seconds of the high power phase, 1.7 MW at the peak was produced and 2 MJ of energy. The influence of the PTE, including a series of experiments on the vessel wall with respect to the tritium inventory, one of the main problems, is described by Andrew et al. [8]. A new 'world record' was set by the American Tokamak Fusion Test Reactor (TFTR) in December 1993. In that experiment 6 MW of fusion power was produced, comparable with the output of a medium-sized jet engine [9].

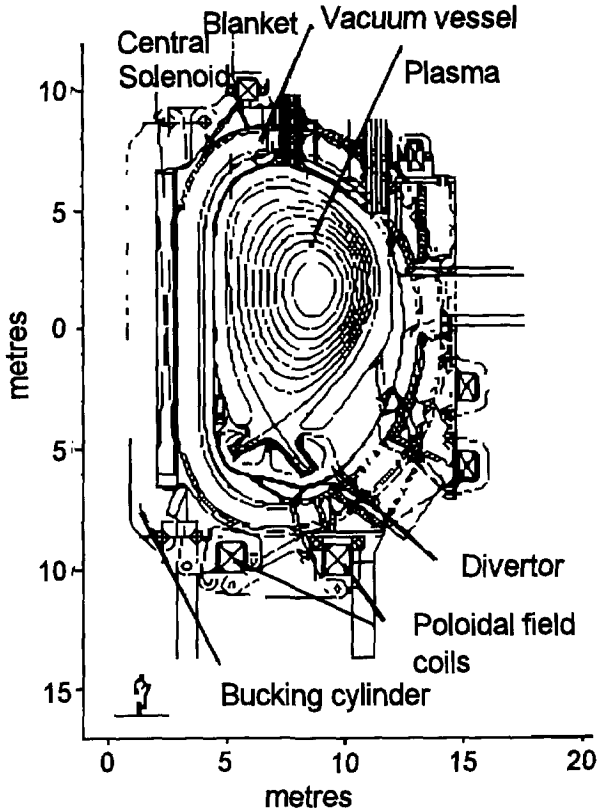

Fig. 1.1. Toroidal cross section of the ITER/EDA design, from Ref. 14.

To follow up experiments with the three largest fusion devices, an International Thermonuclear Experimental Reactor (ITER) is underway. The four international partners, being Europe, US, Japan and the Russian Federation, have decided to develop a reactor that shows the technical and environmental viability of fusion within this project. DEMO is a planned demonstration reactor and successor of ITER. The reactor will be a fusion energy device satisfying economic criteria.

Fusion research, being Big Science, is of public concern. Therefore the financial issue must not be underestimated [10-13].

Key research areas of ITER are the first wall (the plasma facing wall), blanket (coolant, ^{3}H breeder), shield (protective plate for the blanket) and divertor (plasma cleaning device) [14]. In figure 1.1 the ITER-

configuration is shown. The design process, which continues to evolve, is guided along the lines of [14]:

- flexibility commensurate with the long time until actual operation of the device;
- reliability necessary to assure a long period of operation with high availability;
- safety required for a nuclear facility;
- cost control, with respect to other energy resources;
- simplicity;
- low waste disposal.

The proposed ITER/EDA (Engineering Design Activities) parameters [14,15] can be found in table 1.1.

The ITER machine is designed for operation in two phases, the basis performance phase (BPP), and the extended performance phase (EPP). At this moment it is not clear if the two phases are competitive options, otherwise EPP will be a follow up of the BPP. The BPP is described as an initial phase requiring a water cooled shield at 423-473 K, at moderate pressures of 2-2.5 MPa. The structure is based on steel side walls and a Cu front surface with Be as a plasma facing material. The EPP will operate in a high temperature mode so that the coolant is expected to run at 973 K and at a relatively low pressure, ~1 MPa. The reactor vessel structure will be made of a vanadium alloy with natural liquid lithium as a coolant and breeder. V-5Cr-5Ti is the primary V-alloy candidate chosen for its better resistance against high heat fluxes and better waste disposal properties, i.e. lower activation, than austenitic and martensitic steels. Also, in this case beryllium will be the plasma facing component.

Table 1.1 ITER/EDA design parameters

Parameter		Design value
Nominal major radius		7.75 m
Minor radius		2.8 m
Elongation		1.6
Divertor configuration		single null
Toroidal field at 7.75 m		6 T
Max. Toroidal field ripple at plasma edge		2%
Fusion power	-normal operation	~1500 MW
	-beta limit	~3000 MW
Burn time		1000 s
Plasma current		24 MA
Plasma temperature (core)		25 keV
Plasma density (core)		10^{20} m^{-3}
Years of operation		20 years

The divertor, a magnetic limiter diverting the plasma at the edge, is used to improve the energy confinement time and fusion plasma purity. Plasma outside the central current (the scrape off layer) is transported, by atomic processes such as radiation, charge exchange, recombination and gas conduction, to shields added to the vacuum vessel. At the shields, the impurities are captured [14,16,17,18]. Heat removal requires handling of 5 MW m^{-2} loading on the target plates. A design of the planned divertor in the vessel is shown in figure 1.2. For the in-vessel components, neutron wall loads of 1.5 MW m^{-2} (at fusion power > 2 GW) are expected. Cu and V-alloys are prime candidates for compatibility with the plasma. Thin layers of low Z material (Be/C) are required as plasma facing surfaces.

1.2 Selected fusion reactor materials

This section discusses the candidate materials for ITER on which the experiments described in this thesis have been carried out. Appropriate chapter references are given.

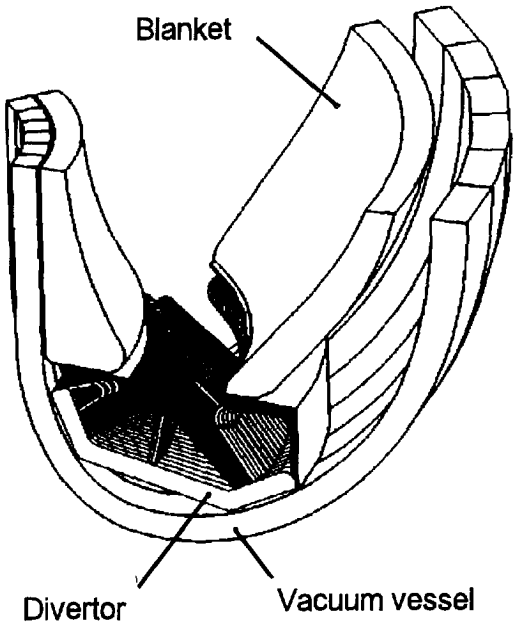

Fig. 1.2. Cut through the vacuum vessel and blanket with view of the divertor design. Only main elements are shown, from Ref. [14].

1.2.1 Tungsten

Twenty years ago, tungsten and molybdenum were considered two of the prime candidates for materials for limiters in large plasma physics experiments such as the fusion reactor [19]. However, it was later recognised that tungsten, being a high Z (Z=atomic number) material and thus causing cooling of the plasma due to brehmsstralung ($\propto Z^2$) and energy

loss by line radiation ($\propto Z^{3-4}$) [20], had some disadvantages. Nevertheless, in the past few years tungsten has again been regarded as a possible plasma facing material [17,21,22,23,24,25]. At low plasma edge temperatures (T_{edge}< 15 eV) tungsten shows almost no sputtering, whereas T_{edge} > 130 eV leads to runaway conditions causing severe problems. At relatively low T_{edge} the local redeposition of tungsten will be close to 100%, limiting the impurity influx, even by sputtering via carbon/beryllium [26,27]. Although hydrogen solubility is low, it can easily be loaded into the near surface region via ion induced damage, which creates deep traps for ^3H [27]. It is thus possible for a high tritium concentration to be formed. Molybdenum, which can be compared with tungsten, was tested as a limiter in TEXTOR experiments, and showed a good performance; only at high densities did the molybdenum limiter cause minor disruptions [28].

In chapters 4 and 5, a study on hydrogen trapping and release and void growth in tungsten is described.

1.2.2 Beryllium

Beryllium has been used in JET as a plasma facing material during the PTE-experiments [8]. Also for ITER Be is considered to be the top candidate for use as plasma facing surface material for the first wall, shields and divertor [14]. It is suitable as a cover because of its low Z value, high thermal conductivity, hydrogen recycling coefficient and it does not form stable hydrides above 573 K [14,22,29]. Due to the previously mentioned intrinsic properties, Be coating reduces plasma radiation, increases the density limit, reduces the incidence of disruption, and enhances deuteron pumping [30]. Also its neutron breeding potential is considered in a solid breeder blanket design. Beryllium can provide additional neutrons for tritium production in a lithium ceramics containing blanket [30]. The relevant two sequences of neutron energy dependent nuclear reactions are as follows:

$$^9Be + n \rightarrow {}^8Be + 2n, \qquad (1.1)$$

having an effective threshold energy of 2.7 MeV,

$$^{8}Be \rightarrow 2\ ^{4}He,$$

and

$$^{9}Be + n \rightarrow {}^{6}He + {}^{4}He, \qquad (1.2)$$

having an effective threshold energy of 1.4 MeV,

$$^{6}He \rightarrow {}^{6}Li,$$

$$^{6}Li + n \rightarrow {}^{4}He + {}^{3}H,$$

using predominantly thermal neutrons.
From reaction (1.1) follows that at high energy neutron bombardment a high helium production rate is to be expected. The problems with the radiation damage can be subdivided into displacement damage (i.e. point defect clustering, irradiation hardening and embrittlement) and transmutation (i.e. gas driven swelling and embrittlement at high temperatures).

The point defect properties and swelling behaviour as a result of post irradiation heating in beryllium are discussed in chapter 6.

1.2.3 Vanadium

As mentioned in section 1.1, vanadium alloys are considered prime candidates as a structural material for the first wall and blanket at high operation temperatures [14,31]. Due to their capacity to handle high heat fluxes, V-alloys, such as V-5Ti-5Cr and V-4Ti-4Cr [32] are a better choice than the austenitic and ferritic/martensitic steels. Other advantages /disadvantages of austenitic and ferritic/martensitic steels can be found in literature [14,31]. For waste disposal, a V-alloy is an excellent option because of its low degree of activation; it therefore falls into the class of the so called Low Activation Materials (LAM) [14,33,34]. A trend can be

found in the literature regarding research on reduced activation ferritic /martensitic steels [35-38]. A possibility concerning the environmental aspects is the multiple recycling via high vacuum melting/refining of the alloy [39]. The compatibility with Li as a coolant/breeder is very good, but reactions with impurities are a disadvantage of V-alloys because of hardening. There are indications that the radiation resistance in terms of swelling can be high [40]. Void formation/swelling can be reduced by Ti additions, and no intergranular helium embrittlement occurs at T < 973 K [31,40]. The high reactivity with oxygen is of great concern; consequently impurities as oxygen must be kept at a low level. Also, aqueous corrosion resistance is not high. The solubility and permeation of tritium are quite high, and can lead to high tritium inventory in the coolant.

To understand the properties of the V-alloys in terms of point defects and the early stages of helium bubble growth, we started to investigate vanadium. Also experiments with niobium, another group 5 element, were performed to support our ideas. In chapter 7 the experiments on vanadium and niobium are described. Follow up experiments on V-alloys are now being performed at the Reactor Physics department of the Interfaculty Reactor Institute.

1.3 Developed and employed techniques

For the purpose of this thesis several techniques are used: thermal gas desorption spectrometry, auger electron spectroscopy, positron annihilation and neutron depth profiling. Thermal gas desorption, also called temperature programmed desorption, is applied as the primary technique. The probe gases were hydrogen, helium, neon and argon. In literature, results on temperature programmed hydrogen release with respect to subsurface defect probing can hardly be found due to its adsorbing, sometimes absorbing, potential. Hydrogen release from defects and surface sites can often not easily be discriminated. Therefore the oxygen coverage trick is introduced (chapter 4).

In chapter two the techniques, and the hydrogen desorption technique in particular, are described.

Literature

[1] J. Glanz, Science **262**, (1993) 1811.

[2] G. Taubes, Science **262** (1993) 1504.

[3] The JET Team, Proc. 14th IAEA Conf. on Plasma Phys. and Controlled Nucl. Fusion Res., Würzburg, vol **1** (IAEA, Vienna, 1993) 15.

[4] TFTR-team, Proc. 14th IAEA Conf. on Plasma Phys. and Controlled Nucl. Fusion Res., Würzburg, vol **1** (IAEA, Vienna, 1993) 111.

[5] JT-60-team, Proc. 14th IAEA Conf. on Plasma Phys. and Controlled Nucl. Fusion Res., Würzburg, vol **1** (IAEA, Vienna, 1993) 57.

[6] The JET Team, The JET Project - Design Proposal, Rep. EUR-JEST-R5, CEC (1975), Brussels, Belgium.

[7] JET Team, Nuclear Fusion **32** (1992) 187.

[8] P. Andrew, J.P. Coad, J. Ehrenberg, D.H.J. Goodal, L.D. Horton, O.N. Jarvis, P.J. Lomas, M.J. Loughlin, G.M. McCracken, A.T. Peacock, M.A. Pick, G. Saibene, R. Satori, P.R. Thomas, Nuclear Fusion **33** (1993) 1389.

[9] J. Glanz, Science **262** (1993) 1966.

[10] P. Aldhous, Nature **353** (1991) 179.

[11] C. Macilwain, Nature **367** (1994) 669.

[12] J. Maddox, Nature **372** (1994) 127.

[13] A. Lawler, Science **267** (1995) 165.

[14] ITER Joint Central Team (presented by W.B. Gaustner), J. Nucl. Mater. **212-215** (1994) 3.

[15] J.W. Davies, D.E. Driemeyer, J.R. Haines and R.T. McGrath, J. Nucl Mater. **212-215** (1994) 1353.

[16] G. Janeshitz, R. König, L. Lauro-Taroni, J. Lingertat, G. Matthews, M. Stamp, G. Vlases, D. Campbell, S. Clement, L. De Kock, W. Eckstein, J. Ehrenberg, N. Gottardi, P. Harbour, L. Horton, H. Jäckel, M. Lesourd, A. Loarte, C. Lowry, J. Roth, G. Saibene, D. Summers, J.A. Tagle, P.R. Thomas and M. von Hellerman, J. Nucl. Mater. **196-198** (1992) 380.

[17] H.E. Prebble, C.B.A. Forty and G.J. Butterworth, J. Nucl.Mater. **191-194** (1992).

[18] M.A. Pick, E. Deksnis, K.J. Dietz, C. Lowry, W. Parsons and R.

Tivey, J. Nucl. Mater. **196-198** (1992) 215.
[19] S.K. Erents, Proc. 8th Symp. on Fusion Technology (SOFT), Utrecht, The Netherlands, 1974, p. 895.
[20] J. Winter, J. Nucl. Mater. **176&177** (1990) 14.
[21] J. Roth, C. Garcia-Rosales, R. Behrisch and W. Eckstein, J. Nucl. Mater. **191-194** (1992) 45.
[22] The JET-team (presented by P.R. Thomas), J. Nucl. Mater. **176&177** (1990) 3.
[23] J. Roth, J. Nucl. Mater. **176&177** (1990) 312.
[24] Discussion session 10.4, J. Nucl. Mater. **179-181** (1991) 1231.
[25] I.V. Gorynin, V.A. Ignatov, V.V. Rybin, S.A. Fabritsiev, V.A. Kazakov, V.P. Chakin, V.A. Tsykov, V.R. Barabasch and Y.G. Prokofyev, J. Nucl. Mater. **191-194** (1992) 421.
[26] C. Gracia-Rosales, J. Nucl. Mater. **212-215** (1994) 97.
[27] P.L. Andrew and M.A. Pick, J. Nucl. Mater. **212-215** (1994) 111.
[28] T. Tanabe, V. Philipps, Y. Ueda, B. Unterberg, A. Pospieszczyk, B. Schweer, P. Wienhold. M. Rubel and B. Emmoth, J. Nucl. Mater. **212-215** (1994) 1370.
[29] R. Satori, G. Saibene, D.H.J. Goodall, E. Usselman, P.Coad and D. Holland, J. Nucl. Mater. **176&177** (1990) 624.
[30] D.S. Gelles, G.A. Sernyaev, M. Dalle Donne and H. Kawamura, J. Nucl. Mater. **212-215** (1994) 24.
[31] M. Dalle Donne, D.R. Harries, G. Kalanin, R. Mattas and S. Mori, J. Nucl. Mater. **212-215** (1994) 69.
[32] H.M. Chung, B.A. Loomis and D.L. Smith, J. Nucl. Mater. **212-215** (1994) 772.
[33] P. Rocco and M. Zucchetti, J. Nucl. Mater. **212-215** (1994) 649.
[34] F. Andristos and M. Zucchetti, J. Nucl. Mater **212-215** (1994) 662.
[35] K. Ehrlich, S. Kelzenberg, H.D. Röhrig, L. Schäfer and M. Schirra, J. Nucl. Mater. **212-215** (1994) 678.
[36] A. Kawamura, H. Kayano, T. Misawa and H. Matsui, J. Nucl. Mater. **212-215** (1994) 690.
[37] D.S. Gelles, J. Nucl. Mater. **212-215** (1994) 714.
[38] R.L. Klueh and D.J. Alexander, J. Nucl. Mater. **212-215** (1994) 736.
[39] G.J. Butterworth, R.A. MCCarthy, G.R. Smolik, C.B.A. Forty, J. Nucl. Mater **212-215** (1994) 667.

Chapter 2.

Experimental methods for gas-defect studies

2.1 Introduction

Fusion reactor materials research is carried out in different ways. Some research is performed at tokamaks distributed internationally; one is also referred to chapter 1. In that way materials can be studied with selected fusion conditions giving irradiation of the wall by the plasma. A second approach is to irradiate the material with neutrons from fission reactors [1-5], or with particles from spallation sources and high energy accelerators [1,3,6-9]. Data from such experiments are mostly analysed in terms of macroscopic material properties as segregation phenomena [1], yield stress/strain [2], corrosion/ erosion rate [2,12], volume swelling [3,5], electrical conductivity [3], thermal conductivity [10], tritium retention/recovery [11]; but also microstructural evolution [4,6-8] is studied. Furthermore, in this way it is possible to get the appropriate He/dpa ratio to the end of the reactor life. The third type of materials research is done by performing small scale laboratory experiments [13-16] . With this type of experiments, early phases of defect development, such as nucleation and growth of defect clusters, can be studied. The fourth method of doing materials research are the computer experiments applied to defect evolution [17-20].

Here experiments of type 3 are described (in chapter 5 type 4 experiments will be quoted). The approach is to create defects by ion bombardment. The defects are probed by helium or hydrogen generally implanted at low energies. Thermal desorption of the probed material reveals the number and type of defects. On many occasions hydrogen and helium ions with energies from 0.1 to 3 keV may also serve as defect creating projectiles. Additional techniques that are employed are in-situ Auger Electron Spectroscopy (AES) for monitoring the condition of the sample surface, a Danfysik Ion Source system for delivering ions with energy to 30 keV, and to a lesser extent the ex-situ analysis techniques, positron beam analysis (PA) for depth profiling of the defects and neutron

depth profiling (NDP) for determining helium depth profiles.

In this chapter the apparatus and techniques used for the present research will be described:

section 2.2 the thermal gas desorption spectrometers, including the Danfysik ion source and AES

section 2.3 Calibration methods, and surface coverage control,

section 2.4 PA and NDP,

section 2.5 sample preparation.

2.2 The thermal gas desorption spectrometers, a technical description

The gas desorption experiments are conducted using five different gas desorption devices, the HDS1 (Helium Desorption Spectrometer 1), HDS2, HDS3, HDS4 and HDD (High Dose Desorption spectrometer). The devices represent three types of gas desorption spectrometers:

1) for helium desorption spectrometers (HDS1, HDS2 and HDS4) were used with a small desorption volume.
2) for hydrogen a desorption spectrometer with a large desorption volume (HDS3) was used. Line of sight detection, thereby avoiding desorption of hydrogen adsorbed at the wall, was applied.
3) for high dose experiments a desorption spectrometer equipped with a low pressure plasma was employed (HDD). The apparatus was also used for sputter cleaning the W and Be samples (see section 2.5).

Only the HDS3 apparatus is described here in some detail.

2.2.1 Vacuum chamber, UHV pumps and baking

The experimental setup is shown in figure 2.1 [21,22]. All the experiments are realized inside a vacuum chamber with background pressure lower than 1×10^{-7} Pa. TDS experiments are executed in a pumped system, therefore the measured partial pressure (P) is not directly related to the release rate (L) of the particles. The relation between L and P is given

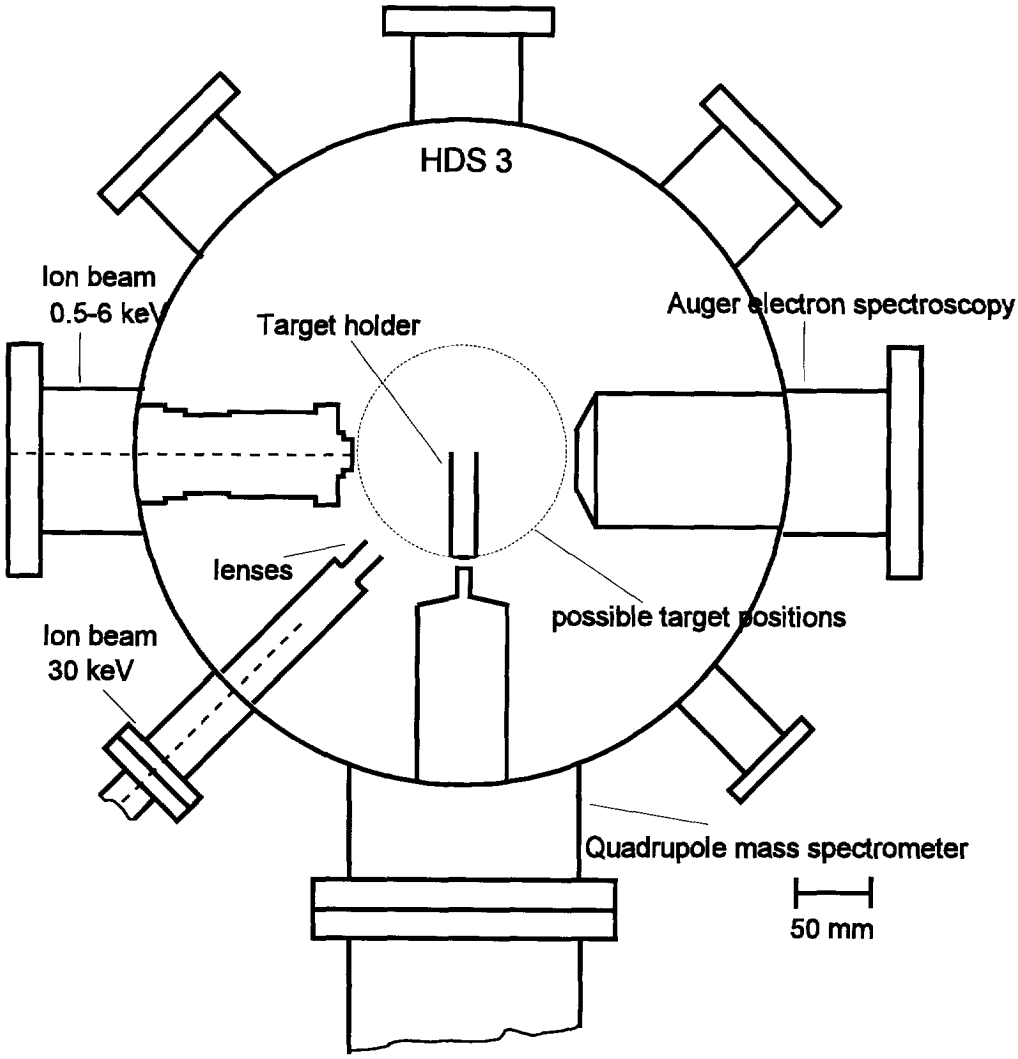

Fig. 2.1. Schematic top view of the HDS 3 UHV chamber for hydrogen desorption experiments. The target can be rotated to face a specific device as indicated by the dotted circle.

by [23]:

$$L = \frac{V}{Nk_B}\left(\frac{dP}{dt} + \frac{P}{\tau}\right) \tag{2.1}$$

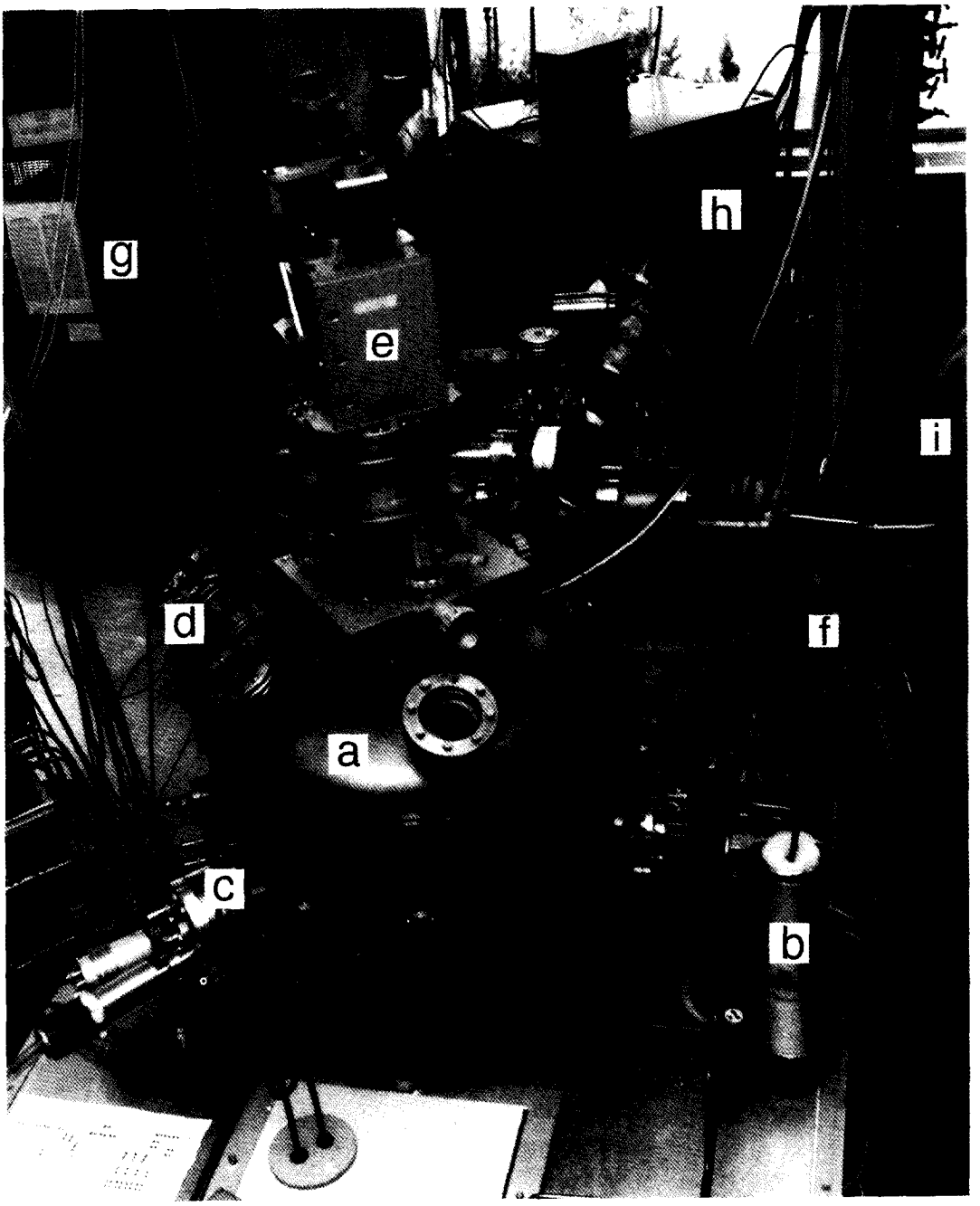

Fig. 2.2. Photograph of the experimental setup of the HDS3 and Danfysik. a) UHV chamber of HDS3, b) liquid nitrogen cooling of the gas supply-pipe, c) Auger Electron Spectroscopy, d) quadrupole mass analyser, e) crystal manipulator, f) ion source, g) Danfysik electronics, h) double focussing magnet of Danfysik, i) heating mantle.

where L is the gas desorption rate in particles per unit time, V the desorption volume, N Avogadro's constant, k_B Boltzmann's constant, P the pressure and τ the residence time.

The volume was estimated to be 0.108 m^3. The residence time τ= V/S (with S the pumping speed) measured by detecting the signal after a calibration pulse, was determined to be 1.24 s for deuterium. The spectra are corrected with eq. (2.1) to obtain the particle release rate.

When the vacuum chamber of the HDS3 has been exposed to air, in order to exchange a sample or change the experimental setup, the system has to be baked in order to reduce the water partial pressure and to remove some adsorbed particles from the parts in the vacuum vessel. Therefore the electrical connectors, after disconnecting the cables, and the viewports are protected with aluminium foil and the HDS3 is packed in a insulating mantle and heated to some 550 K. This is maintained for three days, while the pressure in the HDS3 is monitored. Before stopping the heating the pressure has to be below $3x10^{-5}$ Pa. When the HDS3 is cooled to room temperature, a mass spectrum is recorded to check the constituting gas component to the total pressure of about $1x10^{-7}$ Pa.

2.2.2 The applied target holder and design and construction of a new target holder

Applied target holder

The crystal is mounted on a manipulator, originally designed for ion channeling experiments [24]. The adapted target holder was constructed so that adsorption of gas atoms, such as hydrogen, was kept as low as possible in the vicinity of the sample. Therefore the design resulted in a open construction, as has been shown in figure 2.3. During a desorption experiment deuterium release from adsorption sites at the target holder was therefore suppressed.

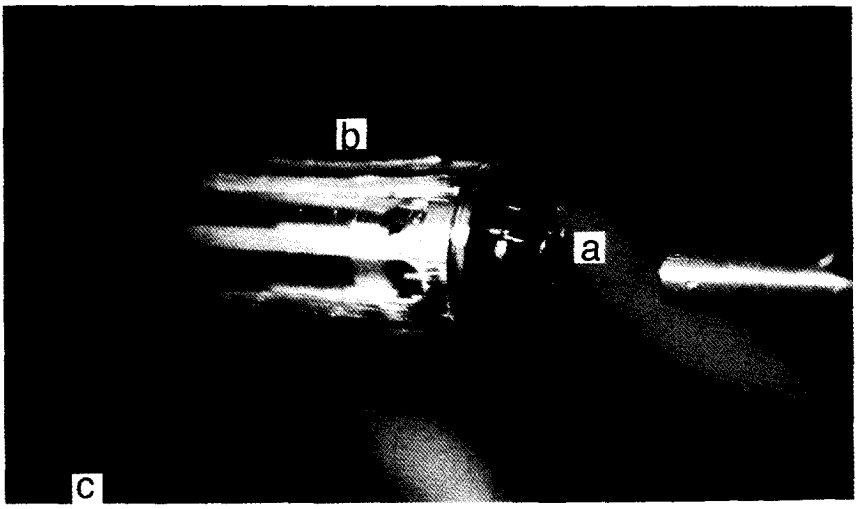

Fig. 2.3 Photograph of the target holder. a) W(100) crystal, b) tantalum holder, c) manipulator.

Design and construction of a new target holder

A multiple target holder was designed to be used on the HDS3 spectrometer. A holder to contain more than one sample is practical, because more crystals can benefit from the HDS3, without opening the vacuum chamber. In figure 2.4 the design and a photograph are shown. The multiple target holder can be rotated and moved linearly in three independent directions (xyz). One crystal at the time can be electrically connected by putting the socket at the end of the cables on the pins belonging to the desired crystal. Before any movement of the disk containing the samples is made, this connection must be removed by elevating the socket. The holder is equipped with two heating elements. One is placed facing the backside of the crystal when the crystal faces the pipe of the quadrupole mass analyser. The other heating element (heating by electron bombardment) faces the backside of the crystal when the crystal is irradiated with gas ions, to facilitate heating during bombardments.

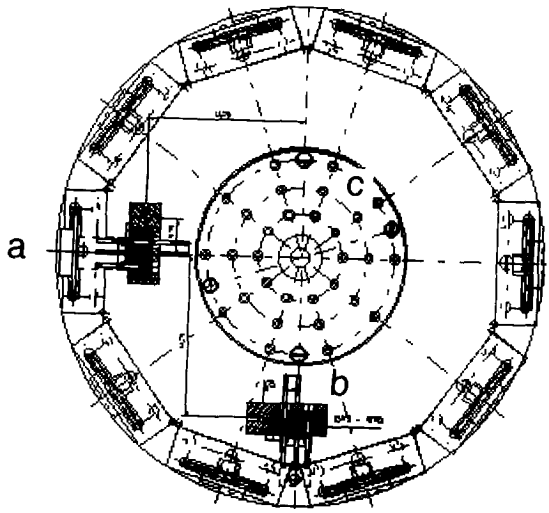

Fig. 2.4a. Technical design of the disk of the multiple target holder. a) one of the ten crystal positions, b) heating device of the sample, c) electrical connectors.

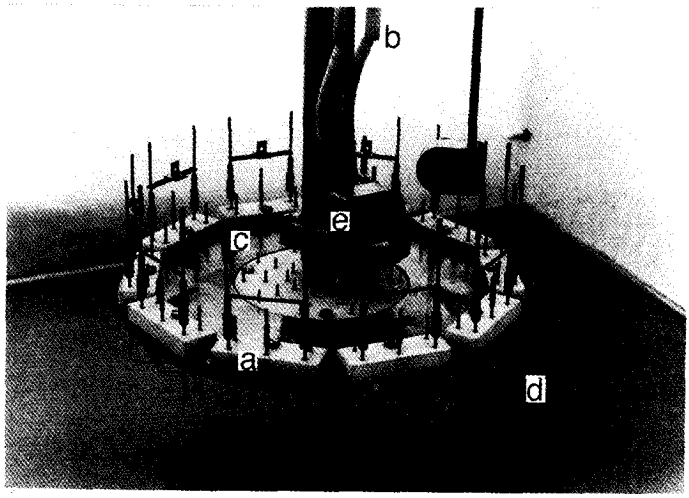

Fig. 2.4b. Photograph of the multiple target holder. The disk with the targetholders is connected to a Huntington PM-600-R manipulator. a) target holder, b) insulated wires connected to the Huntington manipulator feedthroughs and to the disk containing the samples, c) ceramic disk containing the target holders, d) electrical feedthroughs connecting the pins on the ceramic disk and the targetholders, e) heating of the samples via electron bombardment.

2.2.3 Ion sources and gas supply

The two ion sources, the low energy ion beam system and the Danfysik ion source, which can deliver ions in the HDS3 vacuum chamber as well as the gas supply are described in this subsection.

Low energy ion beam system (0.05 -6 keV)

For ion irradiation a low energy ion beam system, developed in our laboratory [21], is used. The design of the ion source is given in figure 2.5. The gas is ionized by electron bombardment and a low pressure ion plasma is formed. Then ions are extracted from the plasma and accelerated with the ion gun electrodes. On their path the ions pass a $\vec{E}x\vec{B}$ filter. This Wien-filter takes care of the velocity selection. Leaving out the problems of hysteresis

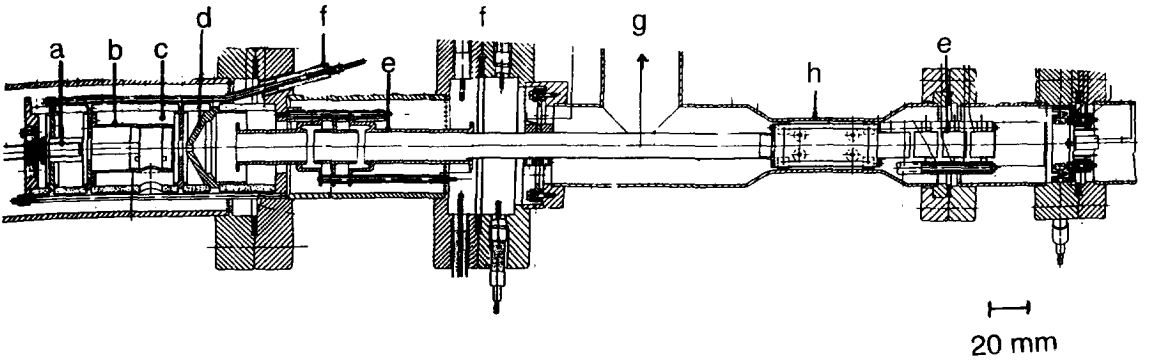

Fig. 2.5. Low energy ion beam system. The ion beam can deliver ions with energies varying from 0.05 to 6 keV. a) filament, b) ionisation electrodes, c) magnets, d) extraction lens, e) lenses, f) flange which allows connection of electric leads, g) to vacuum pumps, h) Wien filter.

and diverging fields at the edges of the filter the formula for the ions passing through the filter can be written as:

$$v = \frac{E}{B} = \frac{V}{NI\mu_0} = (2qE_{ion}/m)^{1/2}. \qquad (2.2)$$

Herein is v the velocity of the ion, E and B respectively the magnitude of the electric and magnetic field, V the potential between the plates of the Wienfilter, responsible for the electric field, and N the number of windings and I the current of the electromagnet, μ_0 the permeability of vacuum, q the charge of the ion, E_{ion} the potential energy of the ion and m the mass of the ion.

From the formula it is clear that particles with double mass (D_2^+ versus D^+) will pass the filter when the current of the electromagnet is increased by a factor $\sqrt{2}$ (fig.2.6). The resolution of this Wien filter M / δM is about 5, using (2.2) and figure 2.6. From the figure it is clear that a

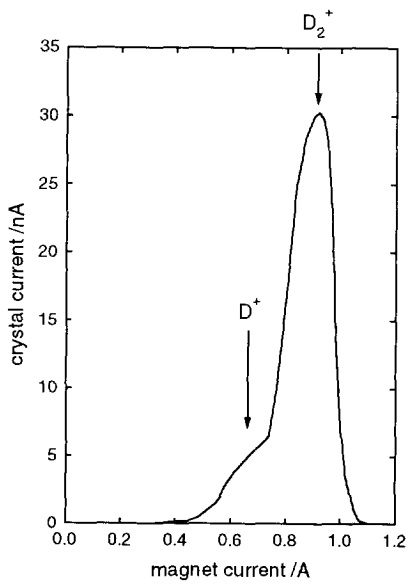

Fig. 2.6. Wien filter spectrum of 1 keV deuterium irradiation at tungsten. The sample current is shown versus the current through the electromagnet of the Wien filter, while the potential at the plates was kept at ± 150 V, giving an electric field of 1.5×10^4 V/m.

selection of ionized molecules instead of ionized atoms is possible. A uniform ion distribution over a certain part of the sample is achieved by ion beam sweeping. The diaphragm of $1x10^{-5}$ m^{-2} was at the exit of the ion source. The secondary electron emission is estimated to be 20% of the total current for the low (50 eV-6 keV) energy ion irradiation. The total current for D_2^+ could easily be manipulated between 0.05 and 2 μA cm^{-2} at an ion energy of 1 keV. The ion current during use was normally 1 μA cm^{-2}.

The effect of the target rotation on the measured ion current at the target, see figure 2.1, is displayed in figure 2.7. From the figure it can be seen that the measured ion current depends on the angle of normal of the crystal with respect to the ion beam. The measured ion current is at its maximum at an angle of 0^0 (±2.5), decreasing rapidly to lower values at other angles. That the ion current has its maximum at angles from -2.5^0 to

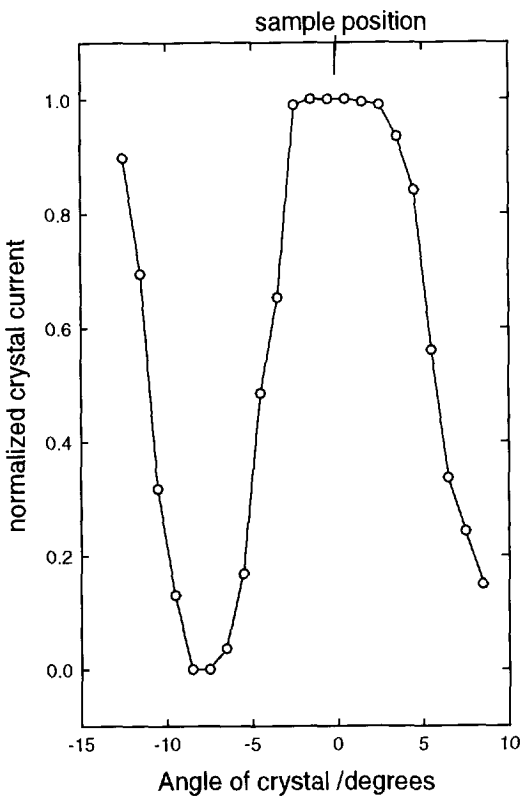

Fig. 2.7. The normalized sample current vs. crystal rotation. The line is used to guide the eye.

$+2.5^0$ can be explained by the dimensions of the diaphragm of the ion beam system and the crystal that rotates on a circle with an radius (r_h) of 70 mm. The diaphragm of the ion beam (d_b), which is circular, has a diameter of 3.5 mm and the diameter of the crystal (d_c) is 6.15 mm. A simple formula for estimating the total angle (θ_{max}) at which the crystal can be rotated, having the maximum ion current, is:

$$\theta_{max} = \frac{d_c}{d_b}\frac{d_b}{2\pi r_h^2}360^0 , \qquad (2.3)$$

with in this case $d_c > d_b$, otherwise the left term in the multiplication at the right hand side would be d_b/d_c. Also, the formula only holds at small angles. When the formula is applied, θ_{max} is calculated to be 5.0^0, as was found in the experiment.

At angles from -8^0 to -12^0 the measured ion current increases due to the irradiation of the target holder.

The Danfysik ion source and secondary electron emission problems

The 30 keV ion beam system based on a Danfysik 911A ion source, see figure 2.8, was used for injection of helium and deuterium ions. The ion source has been designed by Sidenius [25] and the ion beam system was described by van der Kolk [22]. The source is equipped with an oven to create metal vapour, which is ionized to form a metal ion beam.

The ion beam is led through a magnet, by which the beam is bent over 90 degrees. The magnet realizes the mass selection, with a resolution $M/\delta M > 200$. Point to one point projection is realised by the double focussing magnet. The Einzel lens L_1 diverges the beam coming from the extraction cone so that it enters the magnet as a parallel beam. After passing an aperture, the image of the extraction cone, the beam diverges again. At L_2 the beam is focussed on the sample. D_1 and D_2 are the plates which

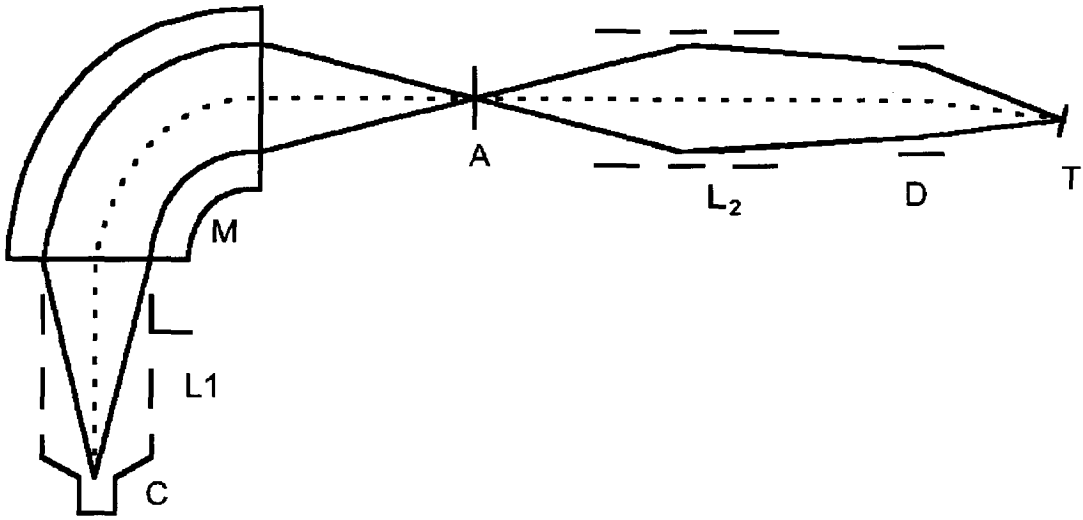

Fig. 2.8. Schematic design of the Danfysik 30 keV ion source. A = Aperture, C = extraction cone, D = deflection plates, L1, L2 = lenses, M = magnet.

accomplish a second deviation to suppress the neutral particles. The plates were also used to sweep the beam for homogeneous ion implantation.

The D_2 pressure at the ion source side during 30 keV implantation was kept at $4x10^{-3}$ Pa. A constant beam current can be achieved by keeping the ion source anode current below 0.8 A. An anode voltage of about 150 V and filament current (depending on the state of the filament) were applied. Keeping the ion source magnet current at a high value (25 A) was necessary to stabilize the anode current and at the same time the beam current.

For the 30 keV deuterium irradiation of tungsten (PA-sample) and 30 keV helium implantation in beryllium, a Faraday cage depicted in figure

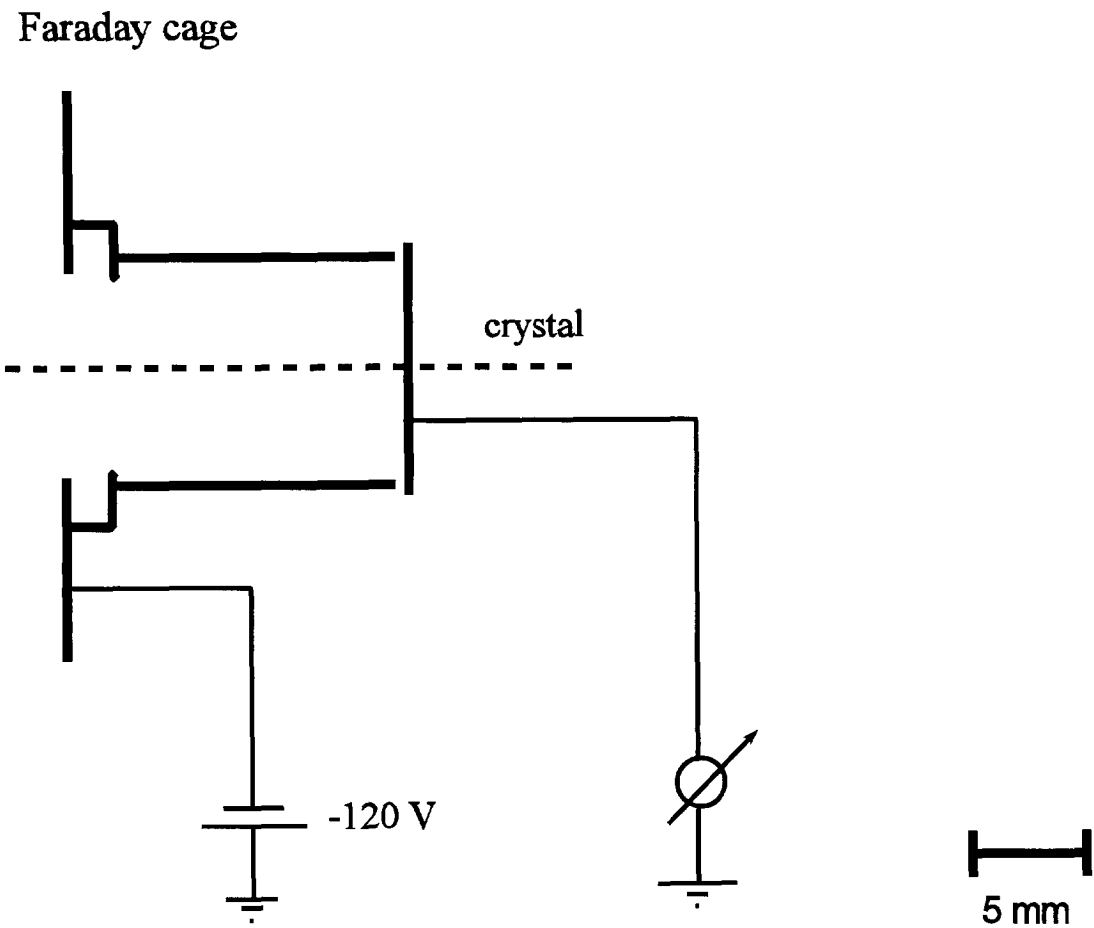

Fig. 2.9 Faraday cage applied for the 30 keV irradiations D_2^+ at W (PA sample) and 30 keV He ion irradiation of beryllium samples.

2.9 was used to neutralize the effect of secondary electrons [26], on the apparent ion current. Recent experiments on secondary electron emission related to hydrogen and fusion materials were performed by Pedgley et al. [27]. At energies of 30 keV the secondary electron emission can be 75% of the total sample current. The total dose measured by integrating the sample current could be verified with the implanted gas amount measured by Neutron Depth Profiling and an agreement within 5% was obtained.

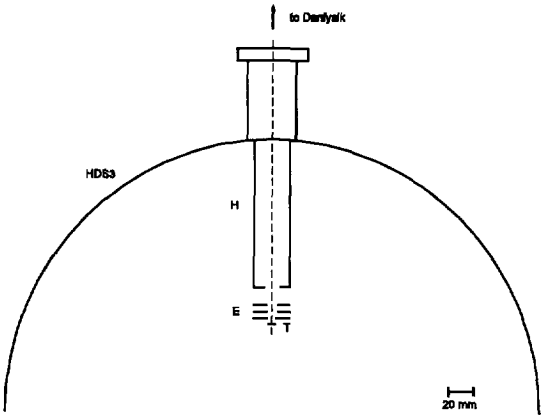

Fig. 2.10a Schematic design of the configuration of the lenses in the HDS3 which suppress the secondary electrons, resulting from the Danfysik ionbeam. H = holder of lenses, E = lenses, T= target.

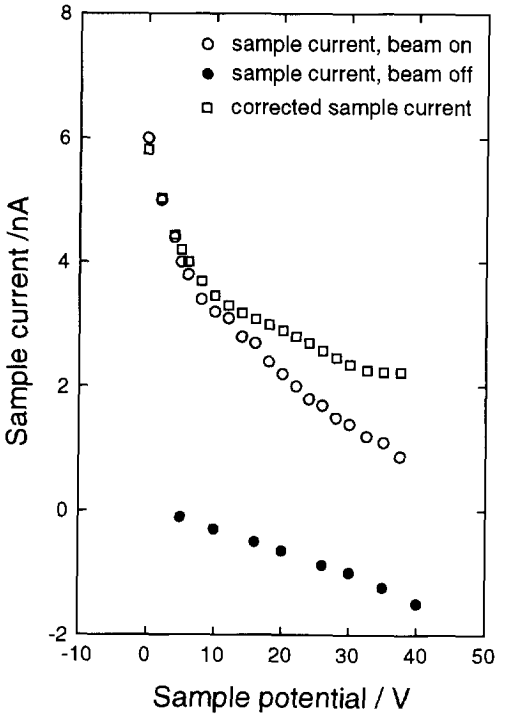

Fig. 2.10b. Results of varying the sample potential. The sample current is displayed versus the applied potential on the crystal.

The secondary electrons in the case of 30 keV D_2^+ irradiation of tungsten (in HDS3) were suppressed as follows. Because of deuterium adsorption, the Faraday cage option could not be employed in the deuterium tungsten experiments. Therefore, a series of diaphragms was used to estimate the secondary electron emission. In figure 2.10a the design and in figure 2.10b the results are given. The ion irradiations were carried out with a potential of +30 V on the sample (grounded to earth via 20 MΩ), while the diaphragm closest to the sample had a potential of -30 V and the succeeding two were grounded. The valve to the HDS3 was only opened during irradiation, causing a pressure rise to $1x10^{-6}$ Pa. Figure 2.10b shows that secondary electron emission is suppressed by the positive potential on the crystal, in combination with the negative potential on the diaphragm closest to the sample. When sample current was corrected for the (fitted) leak current, which was measured with the ion beam off, it was reduced with a factor ≈2.7 from V_{sample}= 0 to V_{sample}= 30 V This reveals a secondary electron emission contribution to the total current of ≈63 %.

Amelinckx et al. [26] showed that a positive bias voltage on the sample in a setup lacking a Faraday cage would not be sufficient itself to suppress the secondary electrons; a magnetic field should also be applied. The measurements of the secondary electrons, using the configuration of fig. 2.10a, showed that the used scheme is a reasonable alternative.

Gas supply

It is important to have pure gas to our disposal, with respect to target surface coverage control. The gas has a quoted 5N purity, which means 99.999 %. The gas is transported to the ion source which can deliver ions with energies varying from 50 eV to 6 keV. In order to obtain clean, for instance non-oxidized surfaces, it is necessary that the gas is oxygen or nitrogen free. This can be achieved with liquid nitrogen cooling of the supply-pipe. After ion-irradiation or gas exposure the surface can be analysed with the AES apparatus, section 2.2.4. We found that, using the above described technique, the oxygen coverage could be held below 0.1 monolayer during hydrogen irradiation. Hydrogen exposure revealed no increase of the oxygen coverage.

2.2.4 Auger electron spectroscopy and the EELS option

The contamination of the tungsten surface could be monitored by Auger electron analysis. A schematic setup of the AES apparatus is displayed in figure 2.11. An extensive review regarding Auger electron spectroscopy is given by Valeri [28]. Calibration was achieved with the help of data given by Davis et al. [29] and full oxygen coverage data at W(100) surfaces published by a number of authors [30-32]. We considered this a better gauge compared to calculations with respect to escape depths of the primary electrons [33,34]. The AES signal was monitored differentially via a Lock-In amplifier (figure 2.11), instead of differentiating digitally the total electron current versus electron energy. Meijer [35] compared the two methods. From his data it was clear that when the differentiation was digital only the sample current was significantly changed (from 30 μA to 1.2 μA). Thus it was not worthwile changing the system to differentiate digitally. Typical AES spectra can be seen in figure 2.14. The impurity coverage of the tungsten crystal was studied by the AES apparatus.

The crystal was positioned about 0.01 m from the AES apparatus. The primary electron energy was chosen to be 2 keV. The modulator voltage (the differentiator) was chosen to be 2 V, the frequency 2 kHz. We

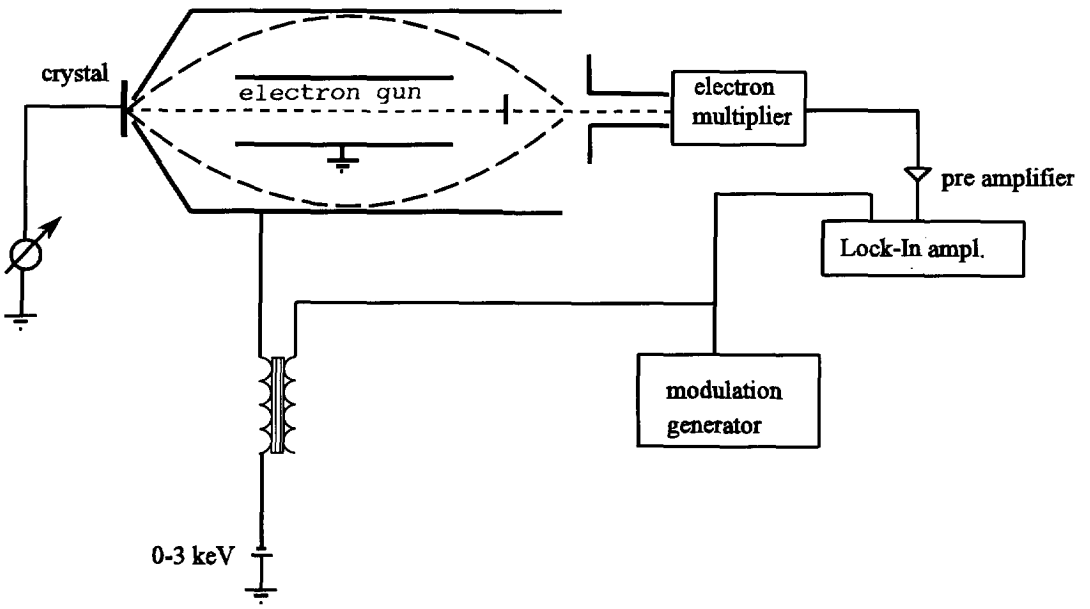

Fig. 2.11. Schematic setup of the Auger electron spectroscopy apparatus

found a resolution of 0.51 % for the 2 keV peak, resulting from the primary electrons (fig.2.12). Whereas a resolution was observed of 0.86% at the oxygen peak. It is important to note that the used AES method only reveals surface coverages of the order of $1x10^{-3}$ per surface atom and higher.
In figure 2.12 also extra peaks can be seen. These peaks caused by electrons which lost their energy to bulk plasmons.

The AES system could also be transformed in performing electron energy loss spectroscopy (EELS). The EELS technique is reviewed by Ibach and Mills [36]. To obtain an electron energy loss spectrum the energy of the

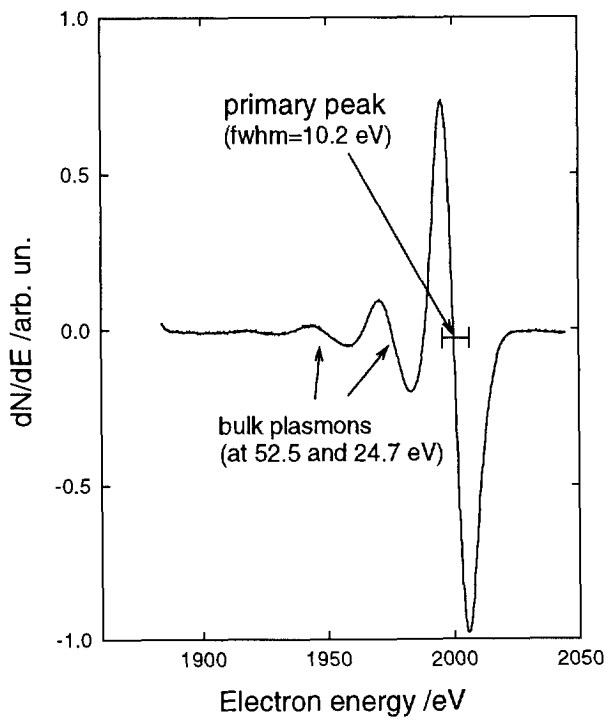

Fig. 2.12 Measured resolution of the Auger apparatus and bulk plasmons of W(100). The FWHM, determining the resolution, is taken at the the primary peak (2000 eV). The bulk plasmons are found at the indicated energies, relative to the primary peak.

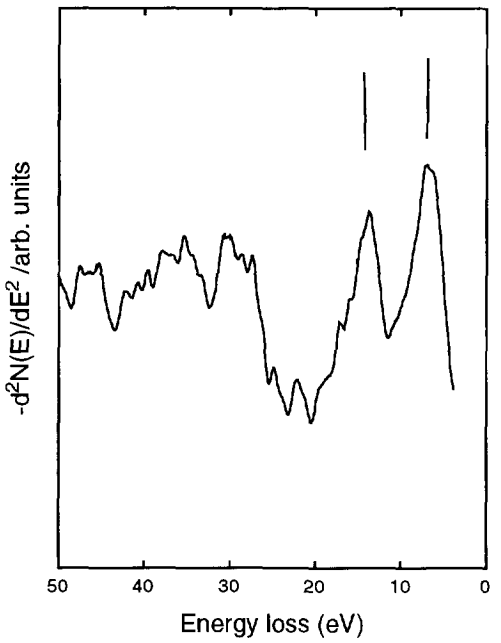

Fig. 2.13 Electron loss spectrum for oxygen covered W(100).

primary electrons was lowered to 200 eV, then the absolute energy resolution is better (2.0 eV ∝ 1.0%). The modulator voltage was lowered to 0.1 V. The EELS spectrum shown in figure 2.13 was formed by differentiating the obtained spectrum digitally, giving a second derivative. The position of the two loss peaks at 7.0 and 13.6 eV indicate a partial oxygen coverage of tungsten [37-40]. In order to observe hydrogen adsorption effects, which are invisible to AES, electron energy loss must be measured on meV scale [41]. For that purpose the energy of the primary electrons must be lowered to some 5 eV. This is not possible in the present setup.

2.3 Thermal desoprtion calibration methods and control of surface coverage

After irradiation the crystal is rotated to face the gas detector, which in our case is a quadrupole mass analyser. The gas release from the crystal is measured by this detector. Heating of the sample is realized by a beam of (1.5 keV) accelerated electrons. The temperature of the crystal was determined by a WRe3%-WRe25% thermocouple. In most thermal desorption experiments the heating rate is taken to be 10 K/s, which is regulated by a computer controlled feedback system [22]. In this subsection the calibration methods for helium and hydrogen will be discussed, as well as the surface coverage handling during hydrogen desorption experiments.

2.3.1 Calibration for helium

The calibration of the quadrupole mass analyser is normally performed as follows. A known amount of helium particles is released from a container. For the HDS systems the containers have a volume of about $1x10^{-6}$ m^3 and of a typical gas pressure of $\sim 10^{-3}$ Pa, so that about $2.4x10^{11}$ particles are set free. The sensitivity of the quadrupole mass analyser to helium is determined by summing the number of measured counts and divide it by the number of released helium atoms. Normally the sensitivity amounts to $1x10^6$ He/count.

2.3.2 Calibration for hydrogen

The calibration of the quadrupole mass analyser is performed in two ways. The first one is exactly the same as for the calibration for helium. The second one is new and is realized by deuterium exposure of a sample with a surface of known orientation and size. In the case of a clean tungsten surface, there will be at maximum 2 D atoms per W(100) surface atom adsorbed. Annealing of a deuterium saturated crystal to 650 K will deliver this amount of gas. Now, from the quadrupole mass analyser response the sensitivity can be derived, as in the case for helium release.

The extra check was done sometimes in addition to the regular calibration. After each experiment the sensitivity was measured. The sensitivity ranged from $1x10^6$ D_2 molecules per count at the output side of the electron multiplier to $5x10^{10}$ dependent on the experimental conditions. A high dose irradiation experiment demands a relatively low sensitivity, for the simple reason of the maximum count rate that is accepted by the pulse counting scaling system, typically 2^{16} per (time) channel. When an experiment is performed using $1x10^{15}$ D_2 particles injected into the crystal and it is assumed that these are distributed perfectly during desorption over 1024 channels, one can calculate that every channel has had 14 times an overflow, when the sensitivity is $1x10^6$ (molecules/count). At low dose, $5x10^{11}$ ions, it is common to accomplish the highest possible sensitivity.

2.3.3 Effects of the angular distribution of desorbed particles on the detection sensitivity

Directional effects were studied by rotating the crystal with respect to the opening of the quadrupole mass analyser. Directional effects could be expected for oxygen covered and clean surfaces, when deuterium chooses to go via different paths leaving the tungsten (100) surface. The opening of the QMA was $\sim 1.5x10^{-4}m^2$, the distance $3x10^{-2}m$ and desorption angle varied from 0° to +/- 20°.

For the experiments on deuterium interaction with point defects, we did not observe any dependence of the gas release on the polar angle of emission, so for deuterium no evidence was found for the so called magic angle desorption [42,43]. Probably the angle independence can be ascribed to the forming of a molecule at the surface before deuterium can leave the crystal.

Comsa and David [44] found a $\cos^8\theta$ behaviour of the D_2 molecules permeating through a Cu crystal and leaving the sample at a surface temperature of 1000 K. They claimed that this result indicated deuterium recombination and desorption from a subsurface site. The desorbing D_2 molecules obtain their kinetic energy from an activation barrier for *ab*sorption.

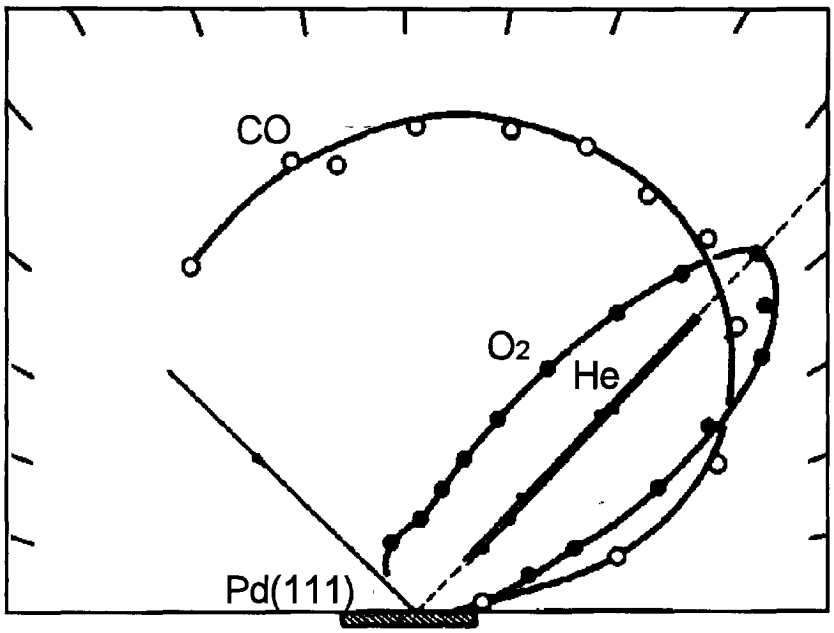

Fig. 2.14. Angular distribution of He, O_2 and CO scattered from a Pd (111) surface, from Ref. [45].

Zangwill [45] compared thermal desorption with scattering and stated that in an experiment published by Engel [46], Fig. 2.14 CO scattering at Pd (111) exhibits nearly isotropic angular distribution due to the fact that the molecule must come to thermal equilibrium with the palladium surface. The CO molecules were trapped into surface adsorption wells, came to equilibrium with the surface and desorbed back to the gas phase. The CO behaviour was in contrast with the helium behaviour, as most He elastically scattered into the specular beam. The CO experiments can well be compared with our deuterium desorption experiments, as deuterium, coming from the bulk or adsorbed at surface sites, must first form a molecule at the surface before it leaves the sample.

2.3.4 Gas coverage control

In performing hydrogen desorption experiments it is important to know the surface coverage with respect to adsorbed gases. Therefore it is equally important to control the coverage of the surface with those gases. In subsection 2.2.4 it is explained that AES is used to determine the impurity coverages of the surface.

There are several ways to handle the gas coverage of the surface; five of them are used and discussed in this subsection:

1) A thermal desorption experiments starts normally with cleaning the sample by flash desorption, heating the tungsten sample for a short time to 2200 K. The oxygen coverage which builds up during night time and in experiments is then removed, see also section 4.2.
2) As mentioned in subsection 2.2.3, in order to obtain clean, for instance non-oxidized surfaces, it is necessary that the gas is oxygen or nitrogen free. This was achieved with liquid nitrogen cooling of the supply-pipe. The surface was thereby free from impurities, i.e. the impurity surface coverage was lower than $1x10^{-2}$ gas atoms/surface atom after hydrogen ion bombardment. When the crystal was exposed to hydrogen no impurities could be detected, i.e. the impurity surface coverage was lower than $1x10^{-3}$ gas atoms/surface atom. This type of surface coverage control was used for almost all deuterium tungsten interaction experiments.
3) Carbon coverage was removed by annealing the tungsten sample to 1500 K at a oxygen pressure of $5x10^{-6}$ Pa for 90 minutes (section 2.5.2). Afterwards the oxygen coverage was eliminated by applying the first method.
4) Surface passivation by oxygen or nitrogen exposure of the crystal. In this way the tungsten surface was passivated so no deuterium could be accomodated at the surface. This allowed deuterium desorption from (subsurface) vacancy type defects to be revealed, which otherwise would be exceeded by deuterium desorption from adsorbed deuterium. This method of surface coverage control can be found in sections 4.3, 4.5 and 4.6.2.
5) A second manner of passivation of the surface is to anneal the tungsten crystal for 1 minute in a oxygen atmosphere of $1x10^{-4}$ Pa.

In this way deuterium is prevented from recombining at the surface during deuterium ion irradiation. This is important while oxygen coverage enhances the deuterium content of the crystal. By this type of passivation, the surface condition is kept constant during partial anneal experiments, otherwise the oxygen coverage can build up during the irradiation with the 30 keV probe dose. This type of surface coverage handling has been described in section 5.2

2.4 Other analysis

Positron annihilation and neutron depth profiling were used to complement the thermal desorption technique. The two techniques are the subjects of this section.

2.4.1 Positron annihilation

This method is based on the annihilation reaction of an electron with a positron. Two gammas are produced in the reaction, each with an energy of 511 keV emitted at an angle of 180°, when the electron-positron pair is at rest:

$$e^+ + e^- \rightarrow 2\gamma. \tag{2.4}$$

If the electron-positron pair has a momentum with respect to the laboratory frame, there will be a deviation from the 511 keV energy and 180° angle. First order approximation of the resulting energies of the gamma's gives $m_e c^2 \pm \Delta E$ with $\Delta E = \frac{1}{2} c p_l$, where ΔE is the energy deviation, c the speed of light and p_l the longitudinal component of the total momentum of the electron positron pair. The deviation from 511 keV is the Doppler broadening. The measured S-parameter follows from the Doppler broadening, as shown in figure 2.15. The parameter is defined as the ratio of the area A, from the central region of the peak, and the total area B. The absolute value of the S parameter has no physical meaning and must be used relatively. It is for instance dependent on the resolution of the gamma

detecting system. Usually, a high S-value can be related to cavities.

In our group a facility is available to inject positrons with variable energies [47-49]. VEPFIT analysis [49] of the S-data versus energy can reveal the depth dependent concentrations of micro-cavities, gas bubbles, interfaces etc. [50].

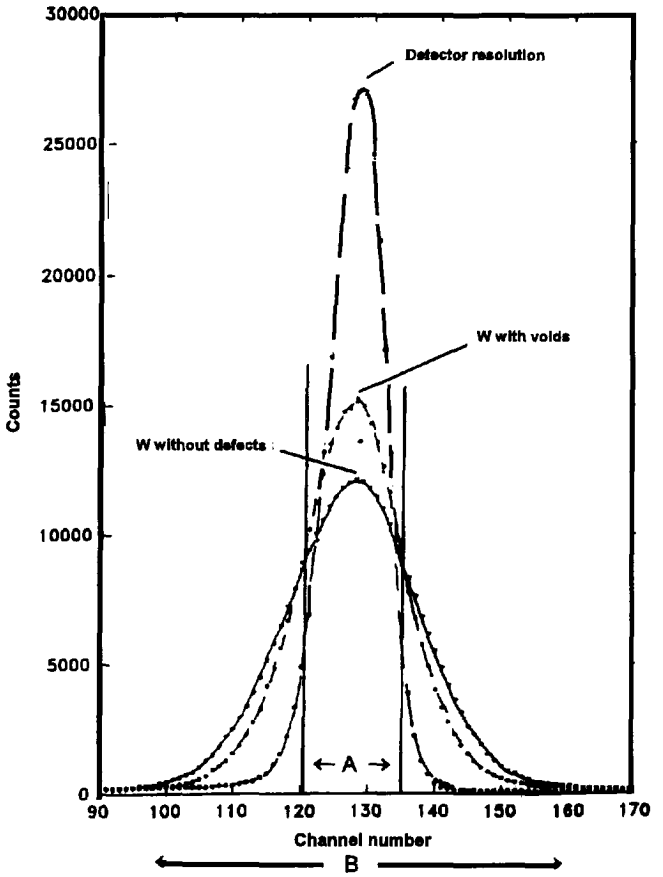

Fig. 2.15. Typical Doppler broadening spectra. The S parameter is determined by the ratio of area A and area B.

2.4.2 Neutron depth profiling

The NDP technique is one of the nuclear reaction techniques (NRA) for depth profiling elements in solid solution. When thermal neutrons are captured by some specific elements (^{3}He, ^{6}Li, ^{10}B and ^{14}N) other particles are created with unique energies. From the energy loss of the particles leaving the sample, the depth of the elements can be calculated. This technique is a quantitative and non destructive method.

The NDP facility, available at our institute, was applied to observe the helium depth profile versus temperature. The ^{3}He doped beryllium sample was irradiated with the thermal neutron beam of the research reactor HOR (Hoger Onderwijs Reactor) of the institute and the following reaction products were formed:

$$^{3}He + {}^{1}n \rightarrow {}^{1}H\ (572\ keV) + {}^{3}H\ (191\ keV) \qquad (2.5)$$

The energy loss distribution of the protons is used for measurement. In the tritium case the noise level is higher and thus less suitable. A typical spectrum is shown in figure 2.16.

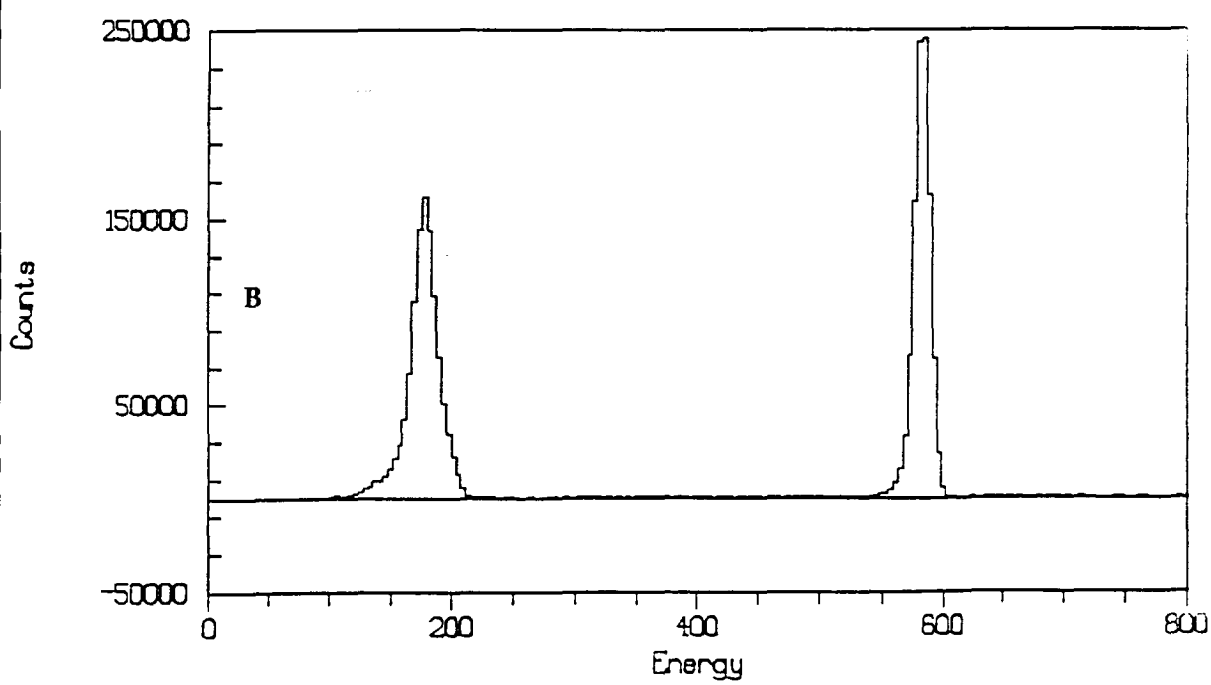

Fig. 2.16. Typical NDP spectrum, which is corrected for the background.

From the energy loss of the proton, the depth of the disintegrated ^{3}He (+n) can be estimated as follows:

$$x = \int_{E_0}^{E(x)} \frac{dE}{S(E)} , \tag{2.6}$$

where x is the depth of the ^{3}He particle, E_0 the initial energy of the proton, $E(x)$ is the detected energy of the proton and $S(E)=dE/dx$ the stopping power. The stopping power is energy and material dependent.

The count rate Z of reaction products, is linear with the total number of residing atoms N_{He}, the thermal neutron cross section σ_{He} (for ^{3}He: 5333 barn), the thermal neutron flux (ϕ_n= 3x10^{11} m^{-2}s^{-1}), and the solid angle of the detector Ω:

$$Z = N_{He}\sigma_{He}\phi_n\frac{\Omega}{4\pi} , \tag{2.7}$$

The depth resolution of the detector depends on the energy resolution of the detector and the stopping power. For the applied setup of ^{3}He in Be and 12 keV detector resolution, the depth resolution was determined to be 200 nm. The detection limit, being dependent on the cross section of thermal neutrons, stopping power, concentration profile and time was estimated to be 4x10^{17} ^{3}He m^{-2}.

To obtain depth profiles, the spectra must be deconvoluted. For this thesis a crude approach was followed to get the FWHM (full width at half maximum) of the helium profile. For both the NDP response function and helium concentration Gaussian profiles are assumed. When a Gaussian profile is convoluted with a Gaussian profile, the resulting profile will also be Gaussian:

$$FWHM^2_{measured} = FWHM^2_{helium} + FWHM^2_{NDP} \tag{2.8}$$

The apparatus response function originates from electronic noise of the system and energy straggling of the detected particle. The FWHM of the

helium profile could be resolved using formula (2.8) and fitting the measured profile with a Gaussian ($FWHM_{measured}$) and the above mentioned depth resolution resulting from the apparatus ($FWHM_{NDP}$). A more accurate deconvolution method is given by Maki et al. [51].

2.5 Sample preparation

In this section the preparation of the used tungsten, vanadium and niobium crystals and beryllium foils is discussed.

2.5.1 Tungsten

Three tungsten (100) crystals were used for the TDS experiments. One crystal was spark eroded from a rod and had a diameter of 6.15 mm and 1.65 mm thickness. The rod was delivered by Materials Research Corporation, claiming the purity to be 99.999 %. After mechanically polishing to 0.25 μm, the crystal was electrolytically polished in a NaOH solution [22]. This crystal was mainly used for experiments described in chapter 4.

The second crystal originating from the same rod as the previous one had the following dimensions: 5.6 mm diameter and a 0.6 mm thickness. After mechanically polishing (0.25 μm) and electrolytic polishing (in NaOH) the crystal was analyzed with AES, figure 2.17, and thermal helium desorption spectrometry (THDS), figure 2.18. Before the THDS experiments were performed, Auger analysis showed a high oxygen and carbon coverage of the surface. Flash desorption to 2200 K removed the oxygen coverage; however, the carbon contamination had been increased. The carbon could eventually be removed by 90 minutes anneal to 1500 K in a $5x10^{-6}$ Pa oxygen atmosphere. The carbon was still present in the bulk as the helium desorption spectra, recorded with 40 Ks^{-1} heating rate, resembled the spectra where a certain carbon concentration was in the bulk [22]. After a series of THDS experiments the carbon impurity concentration was lowered, as the helium desorption spectra improved and the H'-peak decreased. The experiments using this crystal are reported in chapter 5,

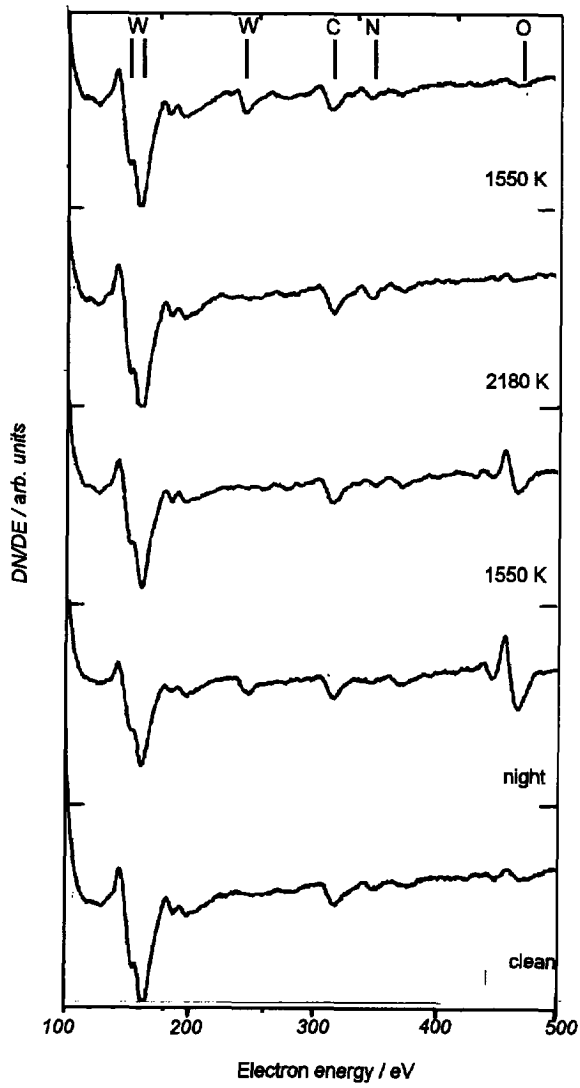

Fig. 2.17. AES spectra to monitor the cleaning of the W sample.

where the hydrogen interaction with cavities is treated.

The crystal W52 was mechanically polished to 3 μm and electropolished in NaOH. Subsequently the crystal was heated several times in $5x10^{-5}$ Pa to 1750 K. The sample W52 was injected with 30 keV $9.9x10^{19}$ D_2^+ m^{-2}, and was subjected to PA measurements.

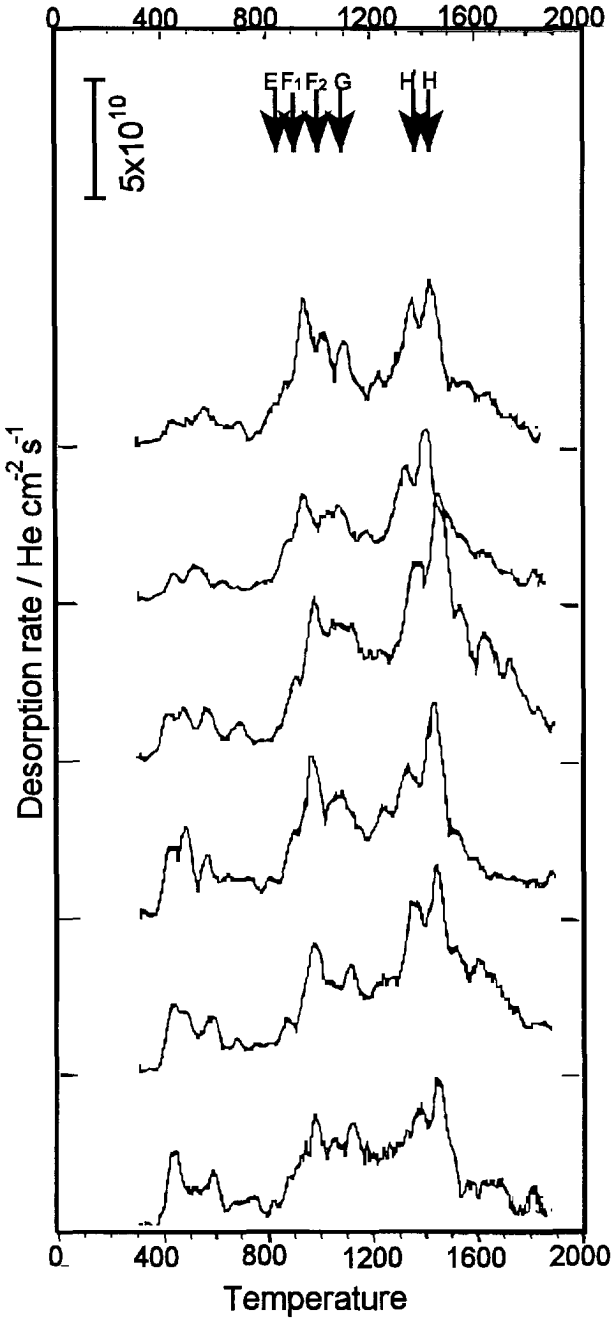

Fig. 2.18. Thermal helium desorption spectra during cleaning of the W(100) sample.

2.5.2 Beryllium

The beryllium samples were obtained from Highways International. The polycrystalline foils had the size 7x7x0.25 mm. The purity was quoted to be 99.5 weight percent, with 0.6 % BeO, being the major impurity . Helium desorption was carried out without cleaning the sample. The NDP- and PA samples were argon sputter cleaned. With 150 eV argon bombardment, a surface layer of 1 μm was removed. Subsequently the samples were annealed to ~900 K.

2.5.3 Vanadium and niobium

The first vanadium crystal with orientation (110) was mechanically polished to 3 μm and electropolished. It was annealed several times to 1400 K in $1x10^{-4}$ Pa before the experiments started. The second crystal, also with a (110) orientation, was treated identically as the first crystal, except that heating was applied in a vacuum system with a base pressure better than $1x10^{-8}$ Pa.

The niobium sample used in the experiments described in chapter 7 was 6.3 mm in diameter and had a thickness of 1.8 mm. It was mechanically polished to 0.25 μm and subsequently electropolished with a 90 % H_2SO_4 and 10% HF solution. The orientation was determined to be (111) by X-ray diffraction.

Literature

[1] I.M. Neklyudov and V.N. Voyevodin, J. Nucl. Mater. **212-215** (1994) 39.

[2] E.A. Kenik, R.H. Jones and G.E.C. Bell, J. Nucl. Mater. **212-215** (1994) 52.

[3] T. Shikama and G.P. Pells, J. Nucl. Mater. **212-215** (1994) 80.

[4] M. Kiritani, T. Yoshiie, M. Iseki, S. Kojima, K. Hamada, M. Horiki, Y. Kizuka, H. Inoue, T. Tada and Y. Ogasawara, J. Nucl. Mater. **212-215** (1994) 241.

[5] H.M. Chung, B.A. Loomis and D.L. Smith, J. Nucl. Mater. **212-215** (1994) 804.

[6] L. Boulanger, J. Chen, P. Jung and Y. Serruys, J. Nucl. Mater. **212-215** (1994) 118.

[7] B.A. Kalin and I.V. Reutov, J. Nucl. Mater. **212-215** (1994) 212.

[8] Q. Xu, H. Watanabe, T. Muroga and N.Yoshida, J. Nucl. Mater. **212-215** (1994) 266.

[9] M.S. Wechsler. R. Ramavarapu, E.L. Daugherty, R.C. Palmer, D.B. Bullen and W.F. Sommer, J. Nucl. Mater. **212-215** (1994) 1678.

[10] C.H. Wu, J.P. Bonal, B. Thiele, G. Tsotridis, H. Kwast, H. Werle, J.P. Coad, G. Federici and G. Vieider, J. Nucl. Mater. **212-215** (1994) 416.

[11] P.L. Andrew and M.A. Pick, J. Nucl. Mater. **212-215** (1994) 111.

[12] C. García-Rosales, J. Nucl. Mater. **212-215** (1994) 97.

[13] K. Hojou, H. Otsu, S. Furuno, K. Izui and T. Tsukamoto, J. Nucl. Mater. **212-215** (1994) 281.

[14] R.A. Anderl, R.J Pawelko, M.R. Hankins, G.R. Longhurst and R.A. Neiser, J. Nucl. Mater. **212-215** (1994) 1416.

[15] G.P. Tartaglia, M.I. de Vries, M.G. Horsten and R. Schmitt, J. Nucl. Mater. **212-215** (1994) 1655.

[16] P. Gondi, R. Montanari and A. Sili, J. Nucl. Mater. **212-215** (1994) 1688.

[17] H. Trinkaus, B.N. Singh and C.H. Woo, J. Nucl. Mater. **212-215** (1994) 18.

[18] H.L. Heinisch, B.N. Singh and T. Diaz de la Rubia, J. Nucl. Mater. **212-215** (1994) 127.

[19] V. Naundorf and H. Wollenberger, J. Nucl. Mater. **212-215** (1994) 226.

[20] H. Kamiyama, H. Rafii-Tabar, Y. Kawazoe and H. Matsui, J. Nucl. Mater. **212-215** (1994) 231.

[21] A. van Veen, A. Warnaar and L.M. Caspers, Vacuum 30 (1980) 109.

[22] G.J. van der Kolk, PhD. Thesis (1984), Delft University of Technology, The Netherlands.

[23] A.A. van Gorkum (1981), PhD. Thesis, Delft University of Technology, The Netherlands, and K.J. Close and J. Yarwood, Brit.

J. Appl. Phys. **18** (1967) 1593.

[24] A. van Veen, crystal-manipulator for UHV applications (1979), Delft University of Technology, The Netherlands.

[25] G. Sidenius , Proc. Int. Conf. on Electromagnetic Isotope Separators, Marburg, Germany (1990) 423.

[26] Defects in crystalline Solids, S. Amelinckx, R. Gevers and J. Nihoul (1973) North Holland publishing.

[27] J.M. Pedgley, G.M. McCracken, H. Farhang and B.H. Blott, J. Nucl. Mater. **196-198** (1992) 1053.

[28] S. Valeri, Surf. Sci. Reports **17** (1993) 85.

[29] L.E. Davis, N.C. MacDonald, P.W. Palmberg, G.E. Riach and R.E. Weber, Handbook of Auger Electron Spectroscopy (1976) Physical Electronics Industries, Eden Prairie, Minnesota.

[30] D.R. Mullins and S.H. Overbury, Surf. Sci. **210** (1989) 481.

[31] T.E. Madey, Surf. Sci **33** (1972) 355.

[32] E. Bauer, H. Poppa and Y. Viswanath, Surf. Sci **58** (1976) 517.

[33] L.C. Feldman and J.W. Mayer, Fundamentals of surface and thin film analysis (1989), North Holland.

[34] R. Memeo, F. Ciccaci, C. Mariani and S. Ossicini, Thin Solid Films **109** (1983) 159.

[35] G. Meijer, thesis University of Twente (1984), Enschede, The Netherlands.

[36] H. Ibach and D.L. Mills, Electron energy loss spectroscopy and surface vibrations (1982) Academic Press, London.

[37] J.H. Weaver, C.G. Olson and D.W. Lynch, Phys. Rev. **B12** (1975) 1293.

[38] P.E. Luscher, Surf. Sci. **66** (1977) 167.

[39] P.E. Luscher and F.M. Propst, J. Vac. Sci. Tech. **14** (1977) 400.

[40] R.S Shinar, T. Maniv and M. Folman, Surf. Sci. **141** (1984) 158.

[41] A. Sellidj and J.L Erskine, Surf. Sci. **220** (1989) 253.

[42] S.W. Pauls and C.T. Campbell, Surf. Sci. **226** (1990) 250.

[43] D.P. van der Werf (1994), PhD. Thesis, University of Groningen.

[44] G. Comsa and R. David, Surf. Sci. **117** (1982) 77.

[45] A. Zangwill, Physics at Surfaces, Cambridge University Press, Cambridge, UK (1990).

[46] T. Engel, J. Chem. Phys. **69** (1978) 373.

[47] H. Schut, PhD. Thesis (1990) Delft University of Technology, The Netherlands.

[48] A. van Veen, J. of Trace and Microprobe Techniques **8** (1990) 1.

[49] A. van Veen, H. Schut, J. de Vries, R.A. Hakvoort and M.R. IJpma, AIP Conf. Proc. **218** (AIP, New York, 1990) 171.

[50] R.A. Hakvoort, PhD. Thesis (1993) Delft University of Technology, The Netherlands.

[51] J.T. Maki, R.F. Fleming and D.H. Vincent, Nucl. Instr. and Meth. **B17** (1986) 147.

Chapter 3.

Modelling of hydrogen desorption from defects in metals

3.1 Introduction

Hydrogen isotope interactions with materials is an important issue in thermonuclear fusion research, as already mentioned in chapter 1 and 2. Tritium retention and recovery, thermal stability of the hydrogen isotopes at the surface or trapped in defects and cavity formation are therefore important topics. In their reviews, Myers et al. [1,2] and Möller and Roth [3] have supplied a theoretical framework and reported experimental data on hydrogen interactions with metals. Nørskov [4], Jacobsen et al. [5] and Nordlander et al. [6-8] developed and employed the Effective Medium Theory, which was used to calculate hydrogen vacancy enthalpies in various metals. Experimental results on hydrogen diffusion and recombination are reported by Pick and Sonnenberg [9,10] and Wampler [11-13].

In this chapter the thermal stability of hydrogen isotopes trapped in defects is described by diffusion and rate theory. The theory is applied to the deuterium tungsten system, but will, in principle, also be valid for hydrogen in beryllium. The effect of the concentration and depth profile of microcavities and the deuterium pressure in the microcavities on the thermal deuterium release is studied. In chapter 5 the theory is applied to vacancy cluster growth in tungsten.

Hydrogen defect interactions are described in section 3.2. Section 3.3 concentrates on diffusion and rate theory. The next section (3.4) is focussed on surface adsorbed hydrogen and hydrogen present in microcavities. Results of model calculations are shown in section 3.5, followed by discussion in section 3.6.

3.2 Hydrogen defect interactions

Hydrogen interactions with defects can be conveniently described using a potential diagram. For example, the enthalpy diagram of the deuterium tungsten system is displayed in figure 3.1. In fact, this diagram is also valid for hydrogen. The diagram shows several typical sites which can be occupied by deuterium entering and emerging from the crystal.

First, outside the metal, deuterium can be found in molecular ($\frac{1}{2}D_2$) and atomic (D) state. The dissociation enthalpy of D from the D_2 molecule is defined as $\frac{1}{2}H^D_{D_2}$. Secondly, at the surface, deuterium can occupy adsorption sites as an atom (with enthalpies H_1 and H_2 relative to deuterium

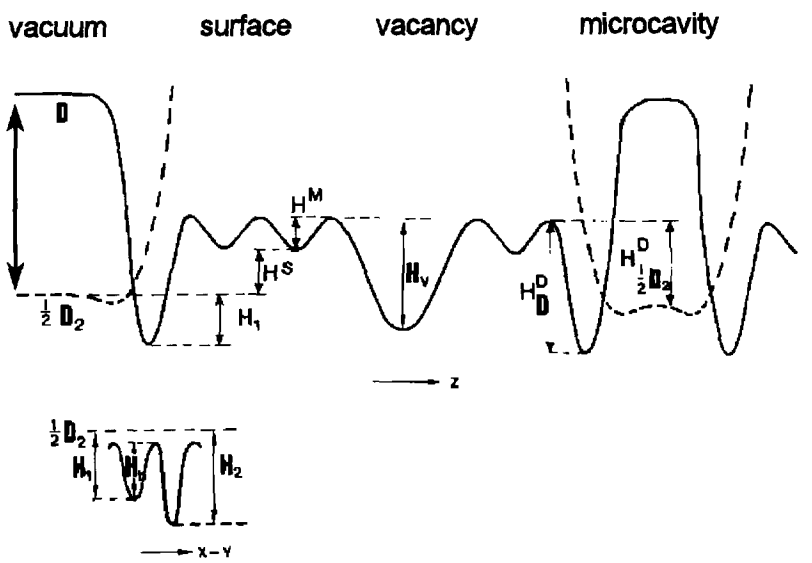

Fig. 3.1. Enthalpy diagram of the deuterium tungsten system for deuterium going from the vacuum into the bulk (z-direction) and of deuterium "hopping" at the surface between (un)reconstructed sites (x-y direction). H_1, H_2 = binding enthalpy of a deuterium atom at an adsorption site at the un- and reconstructed surface respectively. H_b = enthalpy barrier for deuterium going from site 1 to site 2, H^S= enthalpy of solution (1.0 eV), H^M = migration enthalpy, H_v = deuterium vacancy dissociation enthalpy, H^D_D=enthalpy of deuterium chemisorbed in a microcavity. $H^D_{\frac{1}{2}D_2}$= enthalpy of deuterium as a part of a molecule dissociating from a microcavity.

in the molecular state ½D_2). These adsorption sites will change when the surface is reconstructed (see chapter 4). Thirdly, deuterium atoms in solid solution (enthalpy H^S, relative to ½D_2) can migrate (enthalpy H^M) between tetrahedral and octahedral sites; their concentration is denoted as $c_{H,int}$. Trapping of deuterium atoms in vacancies is the fourth option. They dissociate from the vacancies with a dissociation enthalpy H_V, which depends on the number of hydrogen atoms in the vacancy (Nordlander et al. [8]). Deuterium atoms adsorbed at internal surfaces of microcavities, with H_D^D the dissociation enthalpy from the microcavity and $c_{H,ads}$ the concentration, is the fifth alternative. The last possibility is deuterium in

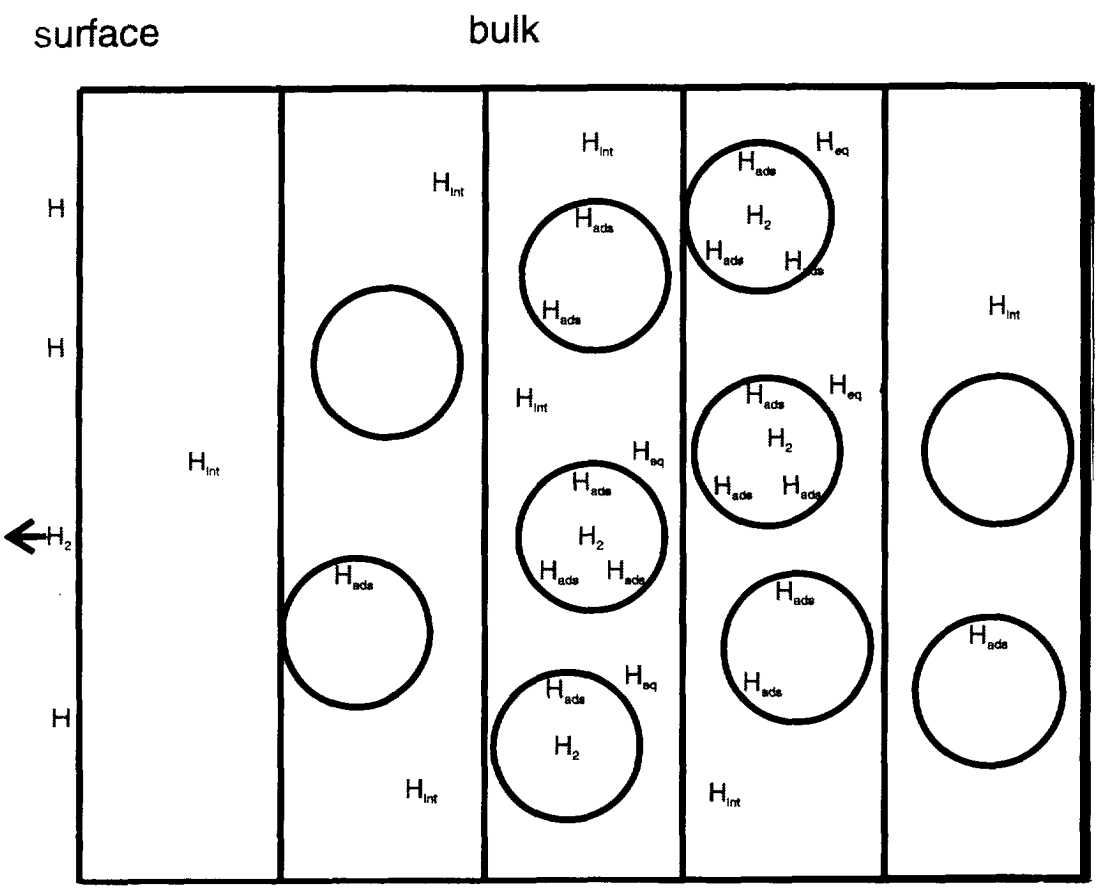
surface
bulk
H
H
H
H2
Hint
Hint
Hint

the molecular state in a microcavity, with $H^D_{½D_2}$ the dissociation enthalpy from the microcavity and c_{H,H_2} as the concentration. All concentrations are given in atomic fractions. Values of the above mentioned activation enthalpies for the deuterium tungsten system are given in table I.

From the low value of the migration enthalpy of deuterium given in table I, it is clear that deuterium interstitials are mobile at 300 K. The deuterium interstitials can be trapped in microcavities or migrate to the surface where recombination takes place. After recombination, deuterium desorbs from the crystal as molecules. Figure 3.2 shows a schematic setup of a sample with deuterium at various sites. The subdivision in strips is later used in calculating the desorption.

Deuterium interstitials in the vicinity of microcavities are expected to be in local equilibrium with the deuterium adsorbed at internal surfaces and deuterium in the molecular state. The concentration of these deuterium interstitials are denoted by $c_{H,eq}$. The equilibrium between deuterium in interstitial and chemisorption sites, with $\theta_{H,ads} = c_{H,\,ads}/N_s c_v$ (N_s = number of available deuterium adsorption sites per microcavity and c_v = concentration of microcavities) is given by the following expression [1]:

$$\frac{\theta_{H,ads}}{1-\theta_{H,ads}} = \frac{c_{H,eq}}{z-c_{H,eq}} \exp[(H_D^D - H^M)/kT] \ , \tag{3.1}$$

where z is the concentration of available sites for H interstitials. The equilibrium between deuterium in interstitial sites and in the molecular state can be described as:

$$\frac{c_{H,eq}}{z-c_{H,eq}} = c_{H,H_2} \exp[(-H^S + ½\mu)/kT] \ , \tag{3.2}$$

with μ the chemical potential of deuterium in the molecular state (see for a further explanation section 3.4).

The concentration $c_{H,t}$ is the total concentration of trapped deuterium in the microcavities:

$$c_{H,t} = c_{H,ads} + c_{H,H_2} \tag{3.3}$$

Table I. Activation enthalpies and their experimental or theoretical values of the deuterium tungsten system. The enthalpy symbols are explained in the text and in figure 3.1.

Activation enthalpy	eV	Reference
$\frac{1}{2}H^D_{D_2}$	2.3	[14]
H_1	0.48-0.76	table 1 of chapter 4
H_2	0.6-0.92	table 1 of chapter 4
H_b	?	-
H^S	1.0	[15]
H^M	0.39	[15]
H_V	1.43-1.55	[16,17]
$H^D_{\frac{1}{2}D_2}$	$\approx H_{1,2}+H^S \approx 1.4^*$	-
H^D_D	$\approx H_{1,2}+H^S+H^M \approx 1.9\text{-}2.2^*$	see also section 5.7

*The ≈ sign is used, because the chemisorption binding at the internal microcavity surfaces is not necessarily equal to $H_{1,2}$ $(=H_1$ *or* $H_2)$, which are defined for deuterium at the outer surface of the tungsten crystal.

3.3 Diffusion and rate theory

The deuterium particle in a 3-dimensional space can move from site to site, where it gets sometimes absorbed in vacancies or defect complexes, and sometimes released from those defects. When the deuterium atoms find the surface during their random walk, they must wait to recombine to molecules before being released from the crystal. This kind of particle behaviour is described by many authors [18-23]. Van Kampen [22] gives a thorough review with respect to stochastic processes. The diffusion equation is explained to be an approximation of the Fokker-Planck equation, jumps in all directions having the same probability. The Fokker-Planck equation already is an approximation of the Master equation as a second order Taylor expansion.

For low particle and (spherical) trap concentration the trapping rate

can be written [18,20] as follows:

$$-Kc_{H,int}\ c_V\ , \tag{3.4}$$

where $c_{H,int}$ is the concentration of diffusing deuterium particles and c_V the concentration of microcavities. $K = 4\pi RND$ is the reaction rate coefficient, with R the size of the microcavity, D the diffusion coefficient of interstitial deuterium and N the host (tungsten) atomic density. Similarly, the source term of particles dissociating from the traps is given by:

$$Kc_{H,eq}\ c_V. \tag{3.5}$$

The complete set of rate and diffusion equations describing the desorption of deuterium from defects is as follows:

$$\frac{\partial c_{H,int}(x,t)}{\partial t} = D\frac{\partial^2 c_{H,int}(x,t)}{\partial x^2} - Kc_V(x,t)[c_{H,int}(x,t) - c_{H,eq}(x,t)] \tag{3.6a}$$

$$\frac{\partial c_{H,t}(x,t)}{\partial t} = -Kc_V(x,t)[c_{H,eq}(x,t) - c_{H,int}(x,t)] \tag{3.6b}$$

Here $c_{H,T}$ is the concentration as described in formula (3.2). The boundary conditions of (3.6a and b) are chosen to be:

$$c_{H,int}(x=0,t) = c_{H,int}(x=L,t) = 0. \tag{3.6c}$$

This is correct with respect to the backside of the crystal ($x=L$), where it is reasonable that the deuterium concentration is zero. In fact, at the implantation side of the crystal, the value of the concentration of deuterium in equilibrium with surface adsorbed deuterium should be used. Therefore,

the deuterium loss due to diffusion of deuterium to the surface will be overestimated.

The flux released from the crystal to the vacuum, J_{out}, is written as follows [1]:

$$J_{out} = D\left(\frac{\partial c_{H,int}}{\partial x}\right)_{x\,0} = -K_L(Nc_o)^2 \,, \tag{3.7a}$$

with c_o the concentration of $c_{H,int}$ at the surface. The flux is expressed as atoms per unit area and time. K_L is the surface recombination coefficient, which can be written as:

$$K_L = \frac{2n_s\nu}{(zN)^2}\exp(-2H_{1,2}/kT), \tag{3.7b}$$

with n_s the areal density of surface chemisorption sites, ν the desorption attempt frequency and $H_{1,2}$ (=H_1 or H_2) the enthalpy needed for an atom to desorb from the surface, see fig.3.1 and section 4.4.

By solving the set of equations of (3.6) and (3.7) and the equilibrium equations (3.1) and (3.2), the thermal deuterium desorption from the tungsten crystal can be calculated. This is performed with a Fortran computer code written for this purpose. The code is written so that the crystal depth is divided into the earlier mentioned strips. Within a strip the set of equations is evaluated and the concentrations of deuterium in the specific states are determined. The diffusivity $D = D_0\exp(-H^M/kT)$ is taken from [15] (see also section 3.5). The defect enthalpies have been given in table I. In the following section an expression is derived for the chemical potential.

3.4 Chemisorbed and molecular hydrogen in microcavities

The relation between interstitial hydrogen ($c_{H,eq}$), chemisorbed ($c_{H,ads}$) and molecular hydrogen (c_{H,H_2}) in microcavities is described in sections 3.2 and 3.3. This section focusses on the hydrogen chemical potential μ of formula (3.2). The equilibrium implies that the chemical potentials of interstitial hydrogen and molecular hydrogen are equal:$\mu = \mu_{H,eq} = \frac{1}{2}\mu_{H_2}$. The chemical potential can be derived by microscopic considerations [24] with partition functions describing rotational and vibrational states, or macroscopically using an equation of state. The last option is used here. With G the Gibbs free energy:

$$G = \mu N_{H_2}, \tag{3.8}$$

$$dG = -SdT - VdP + \mu dN, \tag{3.9}$$

for two coexisting phases in local thermal dynamic equilibrium, i.e. H in the adsorbed phase and the gas phase, the Gibbs free energy must be at a minimum:

$$dG_H = dG_{\frac{1}{2}H_2} = 0. \tag{3.10}$$

When the chemical potential is defined relative to the ground state level of deuterium in the gas phase an expression for μ_{H_2} can be found using the Benedict type Equation Of State (EOS) [25]. The parameters of the EOS for D_2 are obtained from Mills et al. [26]. The EOS expresses the volume as a function of pressure and temperature for $2<P<20$ *kbar* and $75<T<300K$:

$$V = (a+bT+cT^{-1/2})P^{-1/3}+(d+eT)P^{-2/3}+(f+gT+hT^{-1/2}+iT^{-1})P^{-1} \quad cm^3 mole^{-1} \tag{3.11}$$

with the parameters:a=35.283, b=9.4704x10^{-4}, c=3.2843, d=-25.090,

e=6.3917x10^{-3}, f=13.65, g=0.069563, h=-1.5829x10^{2}, i=7.2x10^{2}. Because of the conditions during the experiments (T > 300 K), the EOS was extrapolated to higher temperatures. Mills et al. stated that extrapolation of the formula to lower pressures and extremely high pressures and temperatures agree reasonably with theoretical calculations and shock wave data.

At constant temperature (3.9), using (3.10), can be rewritten as:

$$\mu_{H_2} dN_{H_2} = V dp_{H_2}. \tag{3.12}$$

To a first order approximation,

$$\mu_{H_2} N_{H_2} = p_{H_2} V \tag{3.13}$$

is used, which proved to be adequate, with deviations of a factor varying from 0.6 to 1.7 with respect to the (3.12) integrated result, at temperatures ranging from 600 to 1000 K and pressures ranging from 1 to 20 kbar. At lower temperatures the deviation from the (3.12) integration due the used approximation is worse.

The chemical potential derived from (3.11) and (3.13) as a function of the number of D_2 molecules per microcavity and temperature is shown in Fig. 3.3.

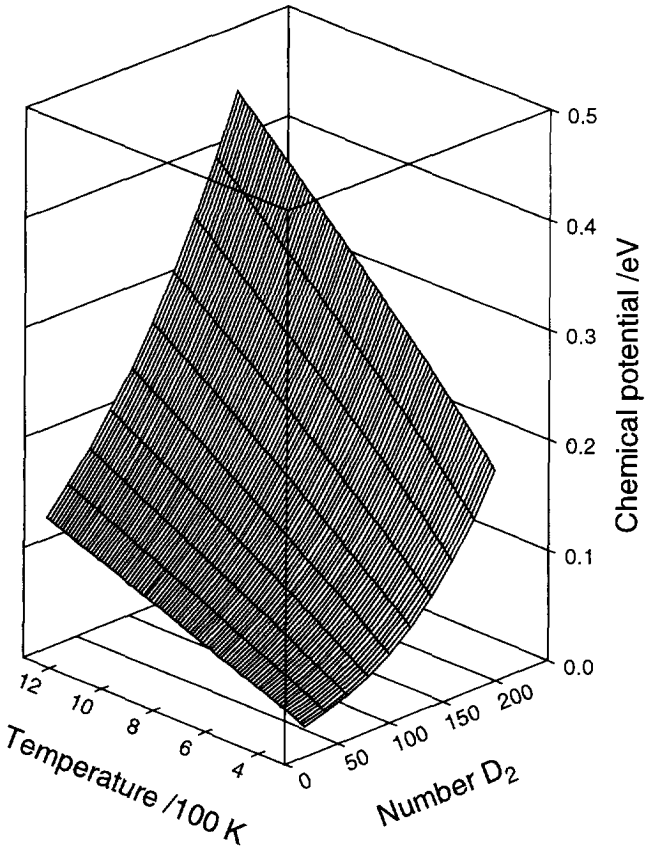

Fig. 3.3. The chemical potential μ_{H_2} as a function of the number D_2 molecules in a microcavity with radius 1nm and as a function of the temperature.

3.5 Results of model calculations

Model calculations were carried out in order to study the effects of microcavity distribution (profile and concentration), surface recombination, deuterium implantation profile at temperatures and deuterium pressure in microcavities. Calculations were done on a 80486/33 Mhz computer, using the Fortran PC-NAG-library (MARK 15), to solve the rate and diffusion equations. The model calculations are carried out with the computer code DIFFUSION.

The size of the slab was taken 0.26 mm, as to be sure that almost all deuterium was desorbed at one side, as in experimental situations.

Depth dependent microcavity distribution

The effect of two different microcavity depth distributions, a Gaussian distribution and a uniform distribution (i.e. from x=0 to x=L), on the deuterium desorption is shown in Fig. 3.4. In the figures 3.4-3.6 and 3.8 the deuterium desorption is normalized with respect to the injected dose in order to relate the spectra from samples injected with deuterium dose

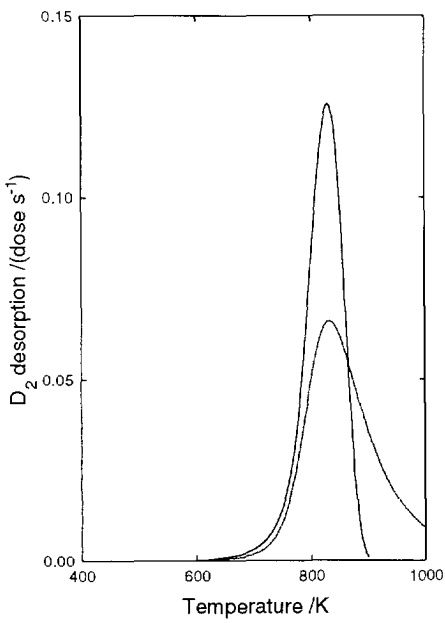

Fig. 3.4. The effect of the depth dependent microcavity concentration on the deuterium desorption. The number of injected deuterium is equal. The solid line: Gaussian microcavity distribution, dotted line: uniform distribution.

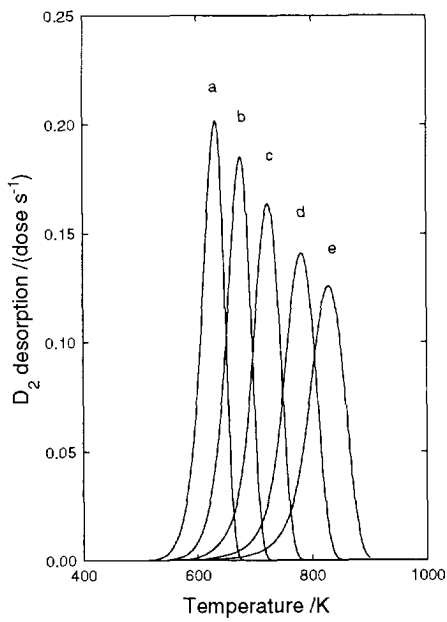

Fig. 3.5. Influence of the defect concentration variation on the deuterium desorption. The number of deuterium injected is equal, the microcavities are given a Gaussian profile. The defect concentrations (depth integrated) are: a) no retrapping, b) $5x10^{16}m^{-2}$, c) $5x10^{17}m^{-2}$, d) $5x10^{18}m^{-2}$, e) $2.6x10^{19}m^{-2}$.

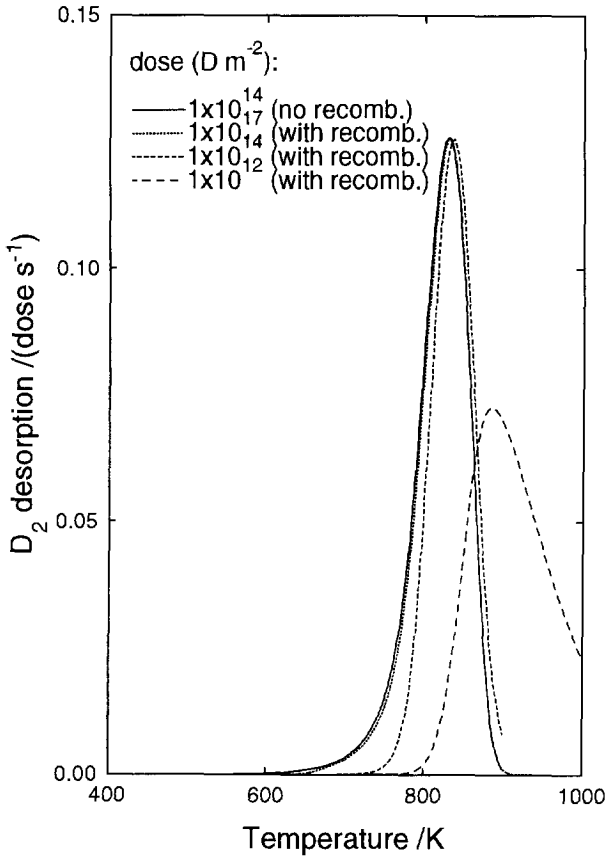

Fig. 3.6 Effect of recombination on the deuterium desorption. The deuterium dose is varied, the Gaussian microcavity distribution is constant in all situations. Note that the desorption rate is normalized with respect to the injected dose. Solid line : no recombination (dose = $1x10^{14}$D m^{-2}), i.e. direct desorption, dotted line: dose = $1x10^{17}$ D m^{-2}, medium dashed line: dose = $1x10^{14}$ D m^{-2}, long dashed line: dose = $1x10^{12}$ D m^{-2}.

ranging over several orders of magnitude. The microcavity concentration in the defect-zone (actually in the FWHM range) of the Gaussian distribution was taken the same as in the uniform case. For the parameters the following values are used: $D_0^H = 4.1x10^{-7}$ m^2s^{-1}, $H_H^M = 0.39$ eV, $H^S = 1.0$ eV, $H_D^D = 1.8$ eV, and the mean depth of the microcavities at 75 nm (straggling 34 nm). A heating rate of 10 Ks^{-1} was used in all calculations. In the following of this section these parameters are used, unless otherwise stated. From the figure it can be seen that the maximum desorption rate is at the

same temperature for both distributions. The simulation using a microcavity concentration that is independent of depth gives rise to the well known diffusion-type desorption, showing a long desorption tail at high temperatures. A Gaussian microcavity distribution leads to a spectrum that is narrower than the previous mentioned distribution. In fact it resembles spectra obtained for first order desorption, although first order desorption spectra are even narrower.

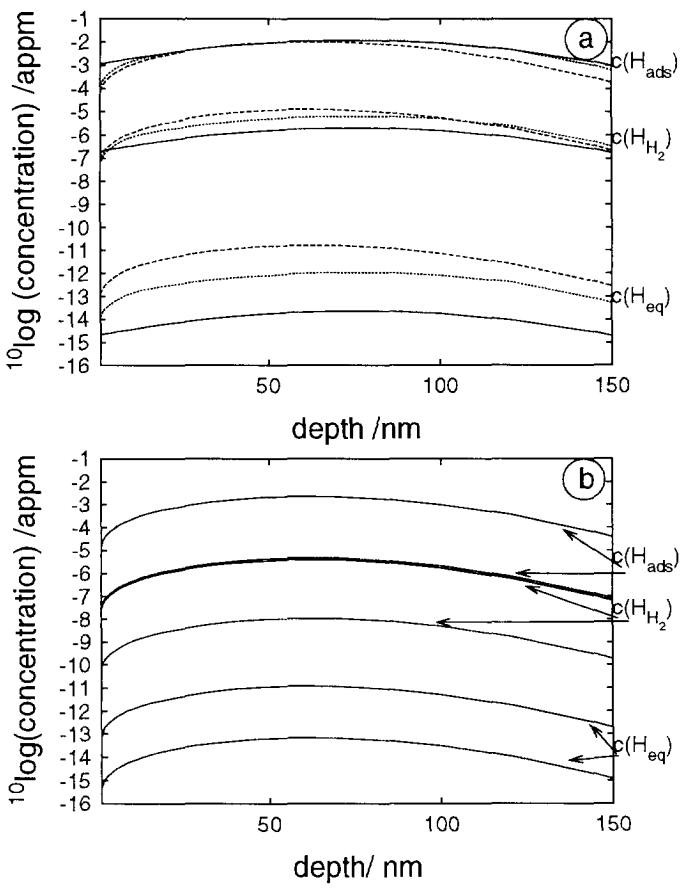

Fig. 3.7a and b Concentration profiles (in appm's) of D in various states and temperatures. Initially deuterium was inserted in the interstitial state. The microcavity concentration was 6 appm at 50 nm mean depth. a) $c(H_{ads})$, $c(H_{H2})$ and $c(H_{eq})$ at— 600 K, --- 700 K,···800 K, b) $c(H_{ads})$, $c(H_{H2})$ and $c(H_{eq})$ at —850 K and ···900 K.

Microcavity concentration variation

The influence of the microcavity concentration on the desorption spectra is given in figure 3.5. The parameters used in the calculations are given above. It can be seen that increasing the microcavity concentrations results in deuterium desorption at increased temperatures. This can be explained by the fact that the increased number of trapping sites give rise to increased number of trapping and detrapping possibilities per atom.

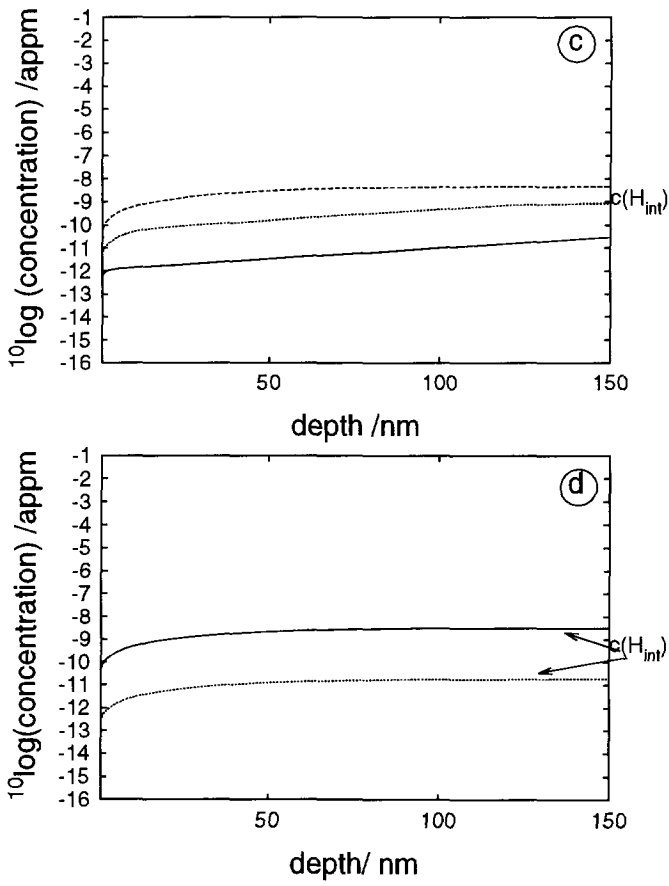

Fig. 3.7 c and d. Compare with 3.7a and b: c) c(H_{int}) at — 600 K, --- 700 K, ...800 K, d) c(H_{int}) at — 850 K and ··· 900 K.

Recombination effects

The influence of recombination is shown in figure 3.6. The surface was a tungsten (100) surface, i.e. $2x10^{19}$ m^{-2} possible deuterium surface sites, and the microcavities were distributed with a Gaussian profile ($2.6x10^{19}$ m^{-2}) at a mean depth of 75 nm (straggle of 34 nm). For deuterium injected doses as low as 10^{14} m^{-2} a temperature shift was calculated of 6 K. When the dose is lowered to 10^{12} m^{-2}, a clear shift is observed as well as a different shape. Obviously, the shape transforms from almost first order desorption to recombination dominated desorption. The concentration profiles of the deuterium in the four different states (including the above mentioned Gaussian microcavity distribution) is shown in figure 3.7. In the

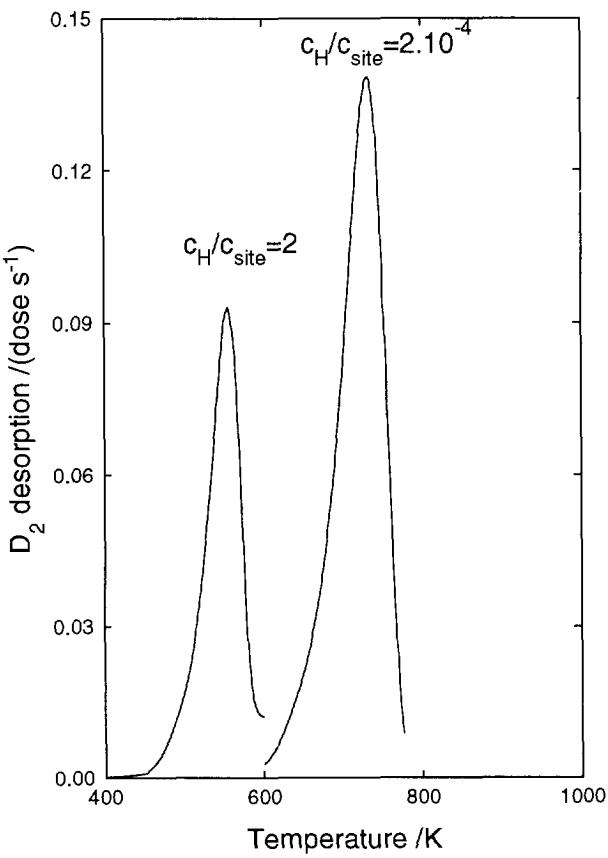

Fig 3.8. Calculated desorption spectra showing the effect of deuterium pressure build-up in the microcavities.

case of a deuterium/microcavity ratio, as has been used here, deuterium prefers to be in the adsorbed state at all temperatures, as expected. At temperatures up to 800 K the concentration of adsorbed deuterium decreases in favour of all the other states. At higher temperatures all concentrations drop to lower values.

At all temperatures the profile of the interstitial concentration is pronounced as it grows with increasing depth, where the deuterium interstitials can migrate freely without being trapped. The other concentrations ($c_{H,eq}$, $c_{H,ads}$, c_{H,H_2}) are confined to the microcavity region.

Influence of deuterium pressure in microcavities

The role of the deuterium pressure in microcavities on the desorption rate is demonstrated in figure 3.8. The deuterium concentration is varied and the microcavity concentration is kept at 5×10^{17} m^{-2}. In the case of a microcavity radius of 1 nm, 240 possible chemisorption sites will be available to hydrogen, assuming a maximum of 2 D/W at an internal surface site. In the calculations the ratio of the deuterium per chemisorption site, was varied from 2×10^{-4} to 2 at the start of the desorption. In fact, the deuterium in the chemisorbed state, $c_{H,ads}$, will be in equilibrium with the molecular and dissolved states, leaving a lower concentration of the $c_{H,ads}$ during the calculations.

The shift to lower temperatures in figure 3.8 at increasing D/microcavity ratio is a direct consequence of the EOS of formula (3.11). When the internal surface sites are covered with impurities like oxygen, the deuterium per remaining site ratio will be high. Thus, when the microcavities are decorated with impurities, deuterium is expected to desorb at lower temperatures.

3.6 Discussion

The model calculations on the desorption of deuterium from tungsten containing microcavities revealed considerable effects due to variations of the defect parameters. Simplified assumptions of the boundary conditions, and a first order approximation in the calculation of the chemical potential the model calculations are used. Calculations in order to evaluate the depth dependence of microcavity concentrations, showed a broader desorption

peak for an uniform depth profile than for Gaussian distributed microcavities. An increasing microcavity concentration resulted in a considerable decrease of deuterium desorption temperatures. Also the effect of recombination was considered. A shift to increasing temperatures at decreasing deuterium doses was observed. Furthermore, increasing the deuterium content of microcavities displayed a decrease of the deuterium desorption temperature. This is ascribed to the increase of the chemical potential of deuterium.

The results of diffusion and rate theory will be applied in chapters 4 and 5 for the deuterium tungsten system. Using different parameters the theory is also applicable to other hydrogen metal systems that can be characterized by a positive heat of solution, e.g. the hydrogen beryllium system.

Literature

[1] S.M. Myers, P.M. Richards, W.R. Wampler and F. Besenbacher, J. Nucl. Mater. **165** (1989) 9.

[2] S.M. Myers, M.I. Baskes, H.K. Birnbaum, J.W. Corbet, G.G. DeLeo, S.K. Estreicher, E.E. Haller, P.Jena, N.M. Johnson, R. Kirchheim, S.J. Pearton, M.J. Stavola, Rev. Mod. Phys. **64** (1992) 559.

[3] W. Möller and J. Roth, Physics of plasma wall interactions in Controlled Fusion (NATO ASI series, Plenum, New York, 1986) p.439.

[4] J.K. Nørskov, Phys. Rev. **B26** (1982) 2875.

[5] K.W. Jacobsen, J.K. Nørskov and M.J. Puska, Phys. Rev. **B35** (1987) 7423.

[6] P. Nordlander, S. Holloway and J.K. Nørskov, Surf. Sci. **136** (1984) 59.

[7] P. Nordlander, J.K. Nørskov and F. Besenbacher, J. Phys. **F16** (1986) 1164.

[8] P. Nordlander, J.K. Nørskov, F. Besenbacher and S.M. Myers, Phys. Rev. **B40** (1989) 1990.

[9] M.A. Pick and K. Sonnenberg, J. Nucl. Mater. **131** (1985) 208.

[10] M.A. Pick, J. Nucl. Mater. **145-147** (1987) 297.

[11] W.R. Wampler, Appl. Phys. Lett. **48** (1986) 405.
[12] W.R. Wampler, J. Nucl. Mater. **145-147** (1987) 313.
[13] W.R. Wampler, J. Appl. Phys. **65** (1989) 4040.
[14] Physical and Chemical Properties (1965).
[15] H. Jehn, H. Speck, E.Fromm and E. Gebhardt, in: *Gases und Kohlenstoff in Metallen*, eds. E. Fromm and E. Gebhardt (Springer Verlag, Berlin, 1976).
[16] H. Eleveld and A. van Veen, J. Nucl. Mater **191-194** (1992) 433.
[17] J.R. Fransens, M.S. Abd El Keriem and F. Pleiter, J. Phys. Cond. Matter. **3** (1991) 9871.
[18] M. von Smoluchowski, Z. Phys. Chem. **92** (1917) 129.
[19] S. Chandrasekar, Revs. Modern Phys. **15** (1943) 1.
[20] T.R. Waite, Phys. Rev. **107** (1957) 463.
[21] R.H.J. Fastenau, PhD. thesis, Delft University of Technology, The Netherlands (1982).
[22] N.G. van Kampen, *Stochastic Processes in Physics and Chemistry*, revised and enlarged edition (1992), North-Holland.
[23] A.A. van Gorkum and E.V. Kornelsen, Rad. Eff. 42 (1979) 93.
[24] L.E. Reichl, A modern course in Statistical Physics (1980), Univ. of Texas Press.
[25] M. Benedict, J. Am. Chem. Soc. 59, (1937) 2233.
[26] R.L. Mills, D.H. Liebenberg and J.C. Bronson, J. Chem. Phys. **68** (1978) 2663.

Chapter 4.

Hydrogen, nitrogen and carbon interactions with the surface and point defects in tungsten

4.1 Introduction

Tungsten is a candidate divertor material for the fusion reactor in ITER, as mentioned in chapter 1. Important aspects are the thermal stability of hydrogen and other impurity atoms at the surface or trapped in defects below the surface. Therefore, it is necessary to have data available on the interaction of hydrogen/deuterium with tungsten. Myers et al. [1,2] and Möller et al. [3] have given overviews on hydrogen defect interactions in a variety of metals, including interactions at subsurface traps. Most of the results have been obtained by depth profiling (nuclear reaction analysis). Interactions of back-diffusing implanted hydrogen with the surface, e.g. surface recombination, has been the topic of many studies. Pick et al. [4,5] have pointed to the influence of impurities on the recombination process. Wampler [6-8] has reported experimental results on the effects caused by oxygen coverage of iron.

In this chapter a rate diffusion model is used to describe deuterium detrapping from subsurface defects and the subsequent surface desorption. Experimental results concerning deuterium detrapping from point defects and from impurity related defects are presented. Of particular importance are the combined deuterium and oxygen adsorption experiments in which deuterium desorption is strongly influenced by the presence of oxygen influences. The oxygen coverage trick, to facilitate observation of desorbing deuterium from subsurface traps, is introduced. This chapter also includes the topic of impurity (nitrogen and carbon) interaction with vacancies studied with the THDS technique.

4.2 Deuterium adsorption experiments

In this section, desorption experiments are presented to show oxygen coverage related effects. The first experiments were conducted with clean surfaces achieved by flashing the sample to a high temperature before the deuterium exposure started. In figure 4.1 TDS results are shown after several exposures of deuterium at a clean W(100) surface. The exposures are expressed in Langmuir units (L), where one unit is defined as 10^{-6} Torr s (≡ 1.33×10^{-4} Pa s), i.e. one second exposure to a pressure of 10^{-6} Torr. It can be seen that at low deuterium exposure a desorption peak at 500 K is

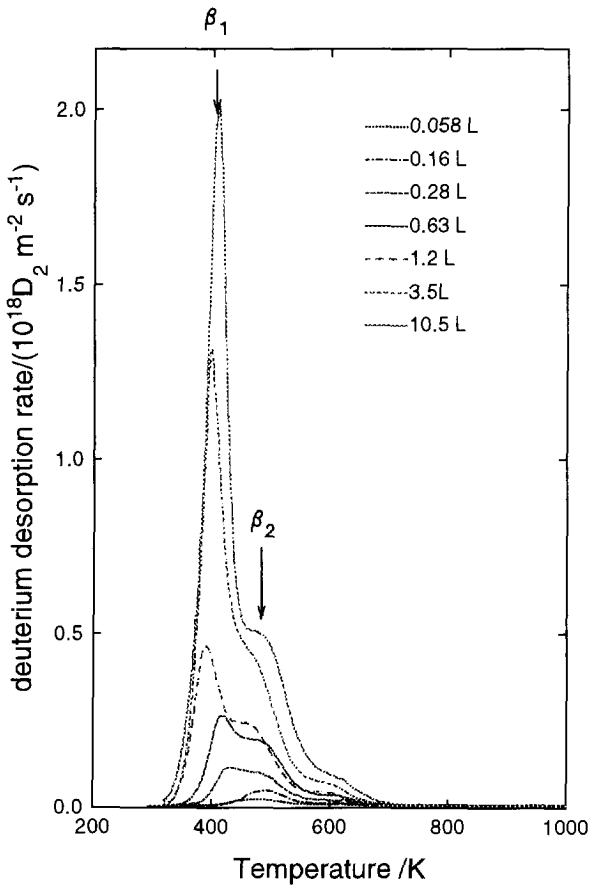

Fig. 4.1. Experimentally obtained D2 desorption spectra. The deuterium exposure is varied from 0.058 Langmuir (=7.73×10^{-6}Pa s) to 10.5 L.

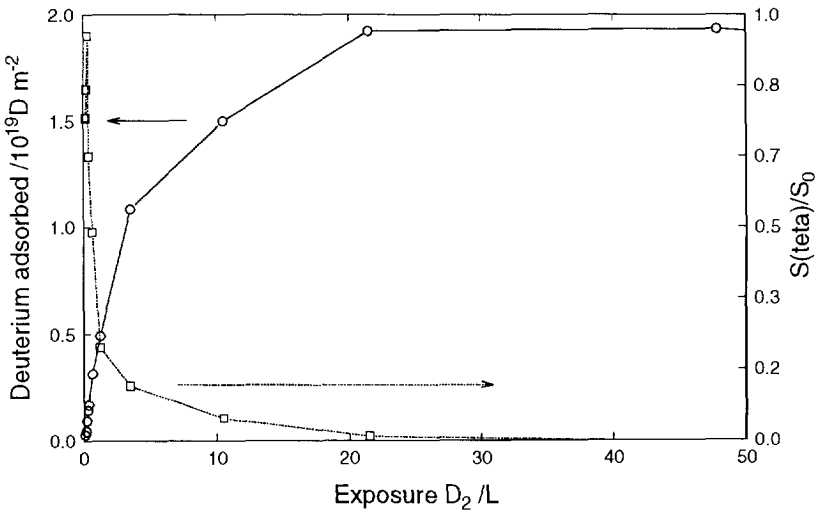

Fig.4.2. Deuterium adsorption experiments, total amount and sticking coefficient vs D_2 exposure. ○: the amount deuterium adsorbed, □ indicate the relative sticking coefficient.

present, denoted by β_2.

When the deuterium exposure is increased another peak rises, and shifts in temperature from ≈450 K to 400 K. This peak is called β_1. The β_1 and β_2 peaks are ascribed in literature to the unreconstructed (original W(100) surface) and reconstructed surfaces respectively [11-14]. Reconstruction occurs for a deuterium coverage lower than 0.5 D atoms per surface tungsten atom. Figure 4.2 shows the amount deuterium adsorbed as a function of D_2 exposure. In this figure the relative sticking coefficient vs D_2 exposure is also plotted. A rapid increase of the amount adsorbed at low exposure is observed with surface saturation at about 20 L. Two monolayers of D-atoms can be accommodated by the surface, i.e. two deuterium **atoms** per tungsten surface atom. The relative sticking coefficient dramatically drops to a low value at 1 L.

In figure 4.3, results are shown of oxygen coverage related deuterium desorption spectra. In this case the surface was cleaned by a temperature flash to 2200 K, and subsequently exposed to oxygen. The oxygen coverage of the surface was analyzed by Auger Electron Spectroscopy.

The last action included deuterium exposure at 180 L, more than sufficient to saturate a clean surface. From the figure it is clear that at about 1 monolayer oxygen coverage almost no deuterium desorption could be observed. Figure 4.4 shows the deuterium peak content versus oxygen coverage, at constant deuterium exposure. Both peak contents decrease with oxygen coverage. For the β_2 peak virtually no deuterium is released for an oxygen

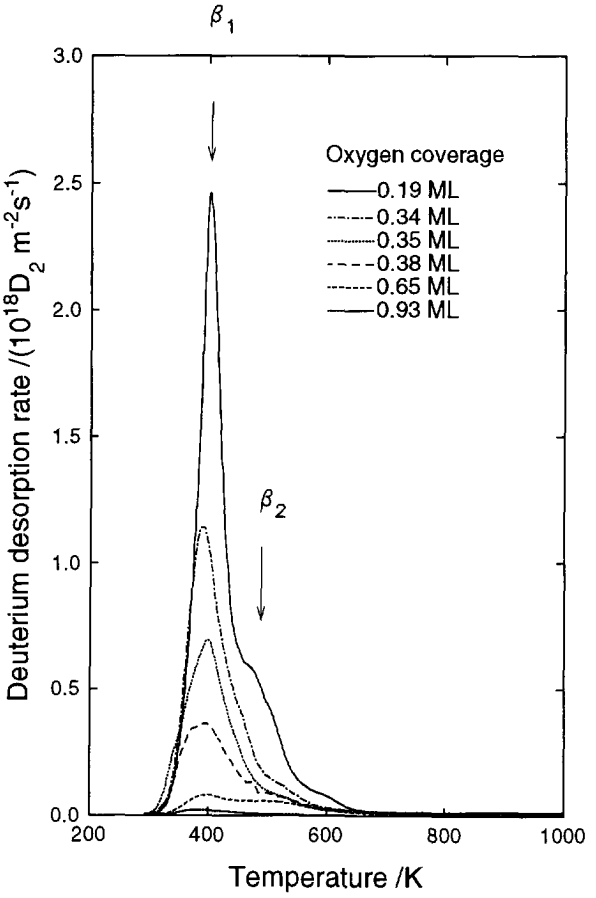

Fig. 4.3. Thermal deuterium desorption spectra. The oxygen coverage was increased, while the deuterium exposure was kept at 180 L.

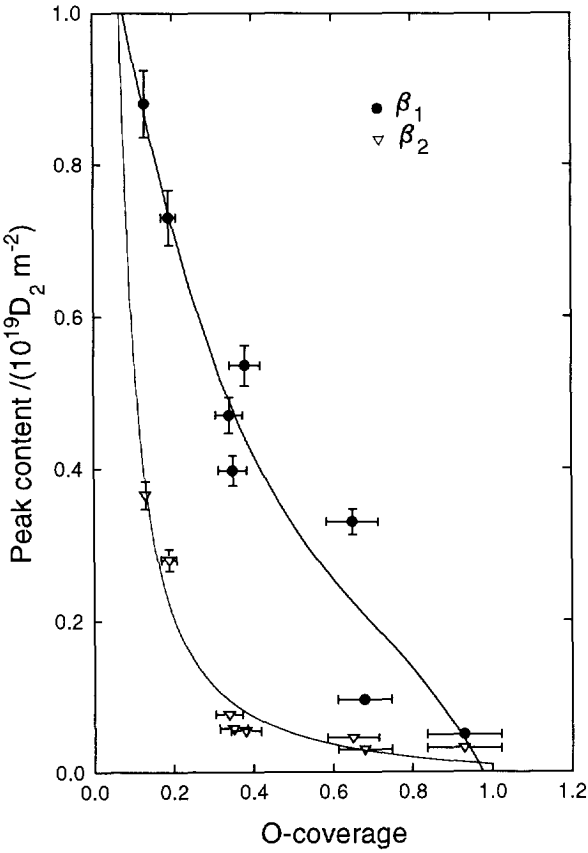

Fig. 4.4. Peak contents of the β_1 and β_2 peaks as a function of oxygen coverage. The deuterium exposure was kept at 180 L.

coverage above about 0.4 ML. However the site causing the β_1 peak remains available until the oxygen coverage increases to 0.8 ML.

When a deuterium saturated surface was exposed to H_2 gas nearly complete isotope exchange took place at 300 K. From this it can be concluded that already at 300 K adsorbed atoms can be replaced, during exposures at long times, by atoms of another gas. The surface sites are thus still available to gasatoms, which are in the vicinity of the surface. Deuterium atoms captured in point defects will not be able to be exchanged

with gas atoms supplied during an isotope exchange experiment. This will be shown in the next section.

4.3 Vacancy type defects, clean and oxygen covered surfaces

Irradiation with 1 keV D_2^+-ions gave spectra that were basically similar to those obtained by adsorption of deuterium from the gas phase. The deuterium atoms entering with approximately 500 eV kinetic energy transferred a maximum of 22 eV to the tungsten atoms, which is below the

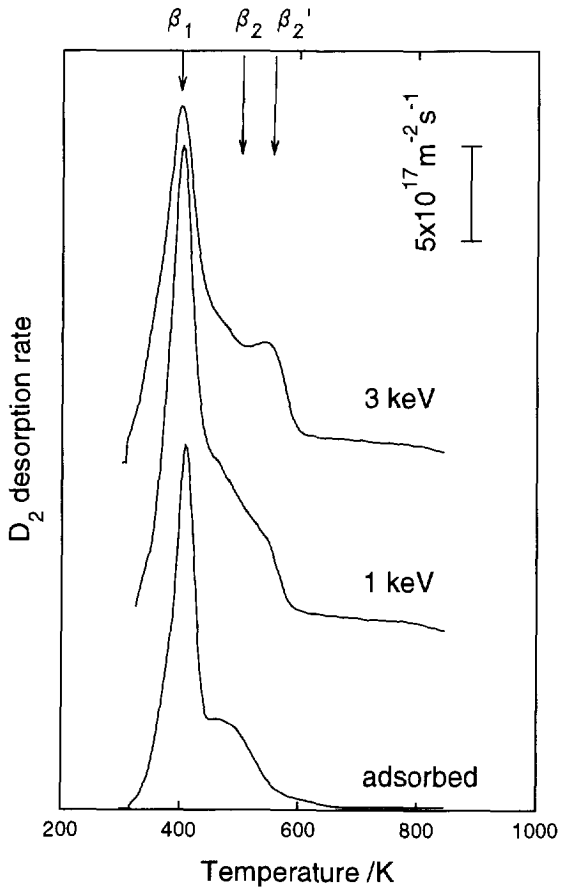

Fig. 4.5. Deuterium desorption spectra for W(100) saturated with gas from the gas phase (by adsorption) and implanted with 3.2×10^{19} m^{-2} 1 keV, and 3keV D_2-ions.

displacement threshold of 40 eV for the bulk tungsten. Therefore, most of the injected deuterium diffused back to the surface to fill the β_1 and β_2 states. An additional deuterium desorption peak at 550 K was observed, which can be related with damage close to the target surface. We will denote this peak β_2'. In the spectrum observed for 3 keV D_2^+-irradiation (maximum energy transfer 66 eV) the peak at 550 K was more pronounced indicating a relation between damaging energy and the occurrence of the latter peak. The trapped fraction amounted to some 100%. Examples of the spectra obtained for deuterium irradiated W(100) are shown in figure 4.5. The reader must be careful in interpreting the spectra as the desorption per

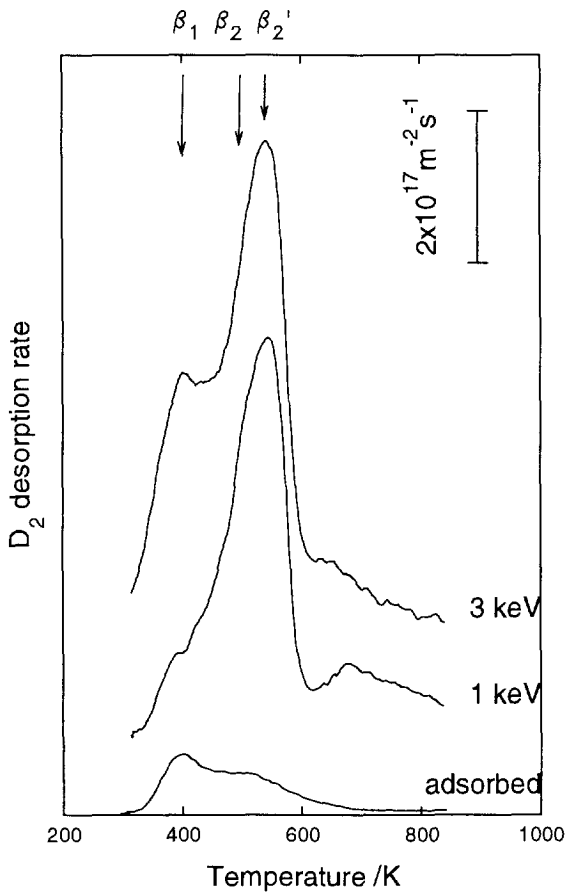

Fig. 4.6. Deuterium desorption spectra similar to figure 4.5, but here for an oxygen covered surface. The oxygen coverage was close to saturation.

area is scaled to the total area of the crystal. In this case the deuterium desorption from the adsorption sites is dominant relative to the injected part. The injected deuterium amounts to 3.2×10^{14} D_2 at an area of 1.0×10^{-5} m^{-2}, compared to an adsorption of 1.84×10^{15} D_2 at a total area of 9.2×10^{-5} m^{-2}. In the remainder of this chapter the deuterium desorption is scaled to the injected area. This is done to accomplish correspondence of the injected / adsorbed dose to the desorbed dose in the spectra. Otherwise there would be an error of a factor 9.2 or the desorption rate must be plotted in D_2 s^{-1} instead of D_2 $m^{-2}s^{-1}$.

Spectra obtained for a near to saturation oxygen covered tungsten

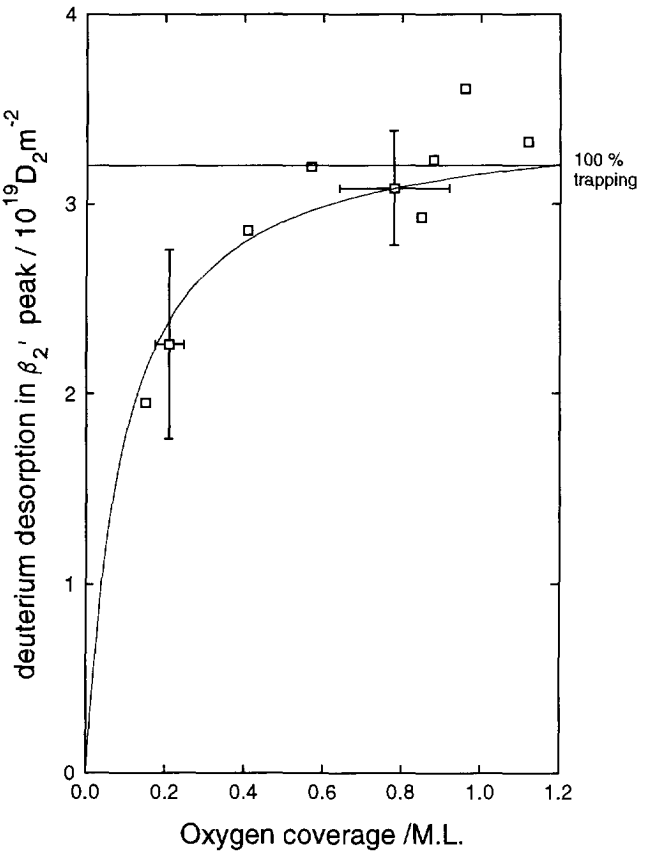

Fig. 4.7. The population of the β_2'-peak vs oxygen coverage for 1 keV D_2^+ irradiated W(100) (dose 3.2×10^{19} m^{-2}. Note the increase of the peak population for coverage < 0.6 Oxygen/surface W atom.

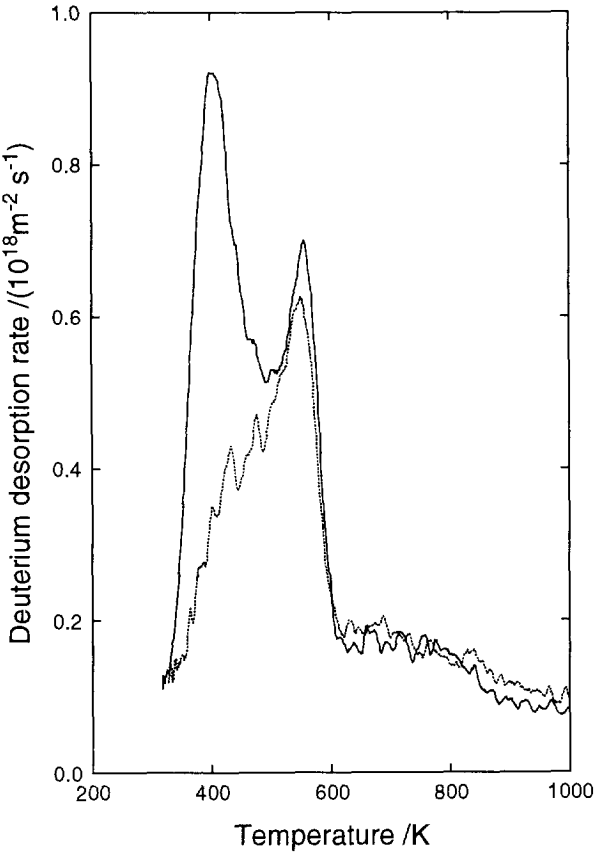

Fig. 4.8. Isotope exchange experiments: deuterium desorption spectra. The injected dose was 3.2×10^{19} D_2^+ m^{-2}. Solid line: no exchange; dotted line: exchange with 1500 L H_2.

surface shown in figure 4.6 indicate only very minor desorption of deuterium after high exposures with deuterium, also shown in figure 4.3. Irradiation with 1 keV and 3 keV D_2^+ ions resulted in a higher amount of deuterium desorbed at about 550 K in the earlier mentioned β_2' peak ascribed to ion induced damage. Besides damage caused by the deuterium ions directly, an equally important damage creation process must be considered. By recoil implantation of the oxygen (D→O→W), oxygen atoms can transfer 55 eV and 165 eV to the tungsten atoms for 1 keV and 3 keV D_2^+ ions respectively. The amount of deuterium appearing in the β_2'-peak as

a function of the oxygen coverage is shown in figure 4.7. The data for this figure are obtained by correcting the amount of the β_2- and β_2'-peak, while they are overlapping, with the deuterium in the β_2-peak at specific oxygen coverages (fig.4.4). It is observed that this amount increases with oxygen coverage and saturates at a value that corresponds with nearly 100% trapping of the implanted deuterium. This maximum can be compared to the 3 keV D_2^+ experiments. TRIM91-calculations [18], simulating the situation of a fully oxygen covered surface, showed a vacancy production of 600 appm, which is in sharp contrast with the 100% trapping. It should be remarked that TRIM assumes a random crystal/adsorbate organisation. In this case oxygen is situated (at coverages greater than 0.5 ML in fourfold hollow sites) 0.2 nm from the W atoms of the second layer, an ideal position for the proposed recoil implantation. Thus TRIM will underestimate the vacancy production.

Isotope exchange experiments with hydrogen, the results of which are given in figure 4.8, demonstrated that deuterium released in the β_2'-peak could not be exchanged. If this deuterium had been present in surface sites at the time of hydrogen exposure, this should have been possible. Therefore the deuterium giving rise to this peak must have been in sites separated by a potential barrier from the surface sites. Most likely these sites are associated with subsurface defects.

4.4 Model for deuterium desorption from subsurface defects

In order to describe the desorption of deuterium from a subsurface trapping site, the potential diagram, given in figure 3.10, of the deuterium tungsten system is adopted. The following rate diffusion model is simplified compared to the one given in chapter 3. The diffusion part is left out. Simultaneously it is extended with respect to the existence of two possible surface adsorption sites. Desorption takes place in four or more steps: (1) dissociation from the trap (e.g. vacancy), (2) bulk migration towards the surface, (3) trapping in a surface adsorption site, if available, and (4) recombination to a deuterium molecule and desorption from the surface. The model assumes two different surface sites, one for the reconstructed surface (indicated with the binding enthalpy H_2 in fig. 3.10) and one for the

unreconstructed surface (having a binding enthalpy H_1) separated by an enthalpy barrier (H_b). The following rate equations describe the above desorption process.

$$dN_1/dt = -2\frac{N_1^2}{N_0} f_1 + N_2 f_{21} - N_1 f_{12} , \tag{4.1a}$$

$$dN_2/dt = -2\frac{N_2^2}{N_0} f_2 + N_1 f_{12} - N_2 f_{21} + N_v f_v , \tag{4.1b}$$

$$dN_v/dt = -N_v f_v , \tag{4.1c}$$

Where the deuterium jumping rates are defined as follows:

$$f_x = \nu_x \exp(-\frac{H_x}{kT}) .$$

Where:
ν_x = attempt frequencies, x = 1, 2, 12, 21 and ν for the different jumps.
The corresponding enthalpies are $2H_1$, $2H_2$, $H_{12} = H_2 - H_1 + H_b$, $H_{21} = H_b$, and H_v respectively (see fig 3.10)
N_0 = total number of possible surface adsorption sites for deuterium,
N_1 = number of deuterium atoms (D) on the unreconstructed W(100) surface (1),
N_2 = number of deuterium atoms on the reconstructed W(100) surface (2),
N_v = number of deuterium in vacancies or other defects, and
N = total number of deuterium (½D_2) particles in vacuum.
In the model the deuterium migration is omitted, so that detrapped deuterium arriving at the surface virtually has not been delayed by diffusion. In tungsten the diffusion length is the solution of quasi stationary solution of (3.27) without retrapping [9]:

$$L_D = \sqrt{\frac{D}{\sum_j K_j \, c_j(z)}} . \tag{4.2}$$

Here D is the diffusion coefficient ($1.16 \times 10^{-13} ms^{-1}$ [10]), K is the rate constant for probe particles trapping at defects (section 3.5.2) and c is the

atomic fraction of defects. At 10 appm defects in tungsten, the diffusion length of the deuterium particles is 29 nm. 1 keV D_2 ions have a mean implantation depth of 6 nm. Therefore, no equation has been included for the diffusion of interstitial deuterium.

The total desorption rate is given by:

$$dN/dt = 2\frac{N_1^2}{N_0}f_1 + 2\frac{N_2^2}{N_0}f_2. \tag{4.3}$$

In the above model the possible effects of adsorbed oxygen or other impurities can be simulated by choosing low values or even negative values for H_1 and H_2, which causes suppressed adsorption of deuterium at the surface. This is in line with the model used for iron by Wampler [6-8] and Richards et al. [13].

4.5 Simulations of the adsorption and low energy D_2 irradiation experiments

In figure 4.9 results of model calculations (section 4.2) are compared with experimental results. The desorption spectrum in fig. 4.9a obtained for a W(100) oxygen-free surface, which is saturated with adsorbed deuterium, appeared to be well matched by a calculated spectrum with parameters given in table I. The activation enthalpies (H_1, H_2) and attempt frequencies (ν_1, ν_2) for the two surface adsorption peaks β_1 and β_2 following from this work and from others are listed in table I. Spectra shown in figs. 4.9b and 4.9d demonstrate that the deuterium release from small subsurface defects can be modeled rather well. In particular the β_2'-peak, obtained for vacancy type defects below an oxygen covered surface, can be described closely, using a dissociation enthalpy $E_{HV}^{D,H}$ of 1.43 ± 0.02 eV with $\nu = 1\text{x}10^{13}\text{s}^{-1}$, $N_v = 1.3\text{x}10^{14}$ cm^{-2} and $N_2 = 0.8\text{x}10^{14}$ cm^{-2}. The attempt frequency was varied to obtain the right shape of the β_2'-peak. The result agrees with the value $E_{HV}^{D,H} = 1.55$ eV found by Fransens et al. [19] at InV_2 complexes, taking into account that they assumed a higher frequency of $2\text{x}10^{14}$ s^{-1}. Furthermore it is assumed that an indium atom resembles a tungsten atom in a tungsten matrix. The calculated deuterium vacancy binding enthalpy reported by

Nordlander et al. [20] of 1.15 eV results in a deuterium vacancy dissociation enthalpy of 1.54 eV, assuming a migration enthalpy of 0.39 eV.

The model was also applied to investigate systematically the effect of surface retrapping of deuterium released from subsurface traps. Simulations were carried out varying the dissociation enthalpy of the deuterium vacancy defect from 1.1 to 1.6 eV; the attempt frequency was kept as $1x10^{13}$ s^{-1}. In figure 4.10 both the deuterium desorption rate from

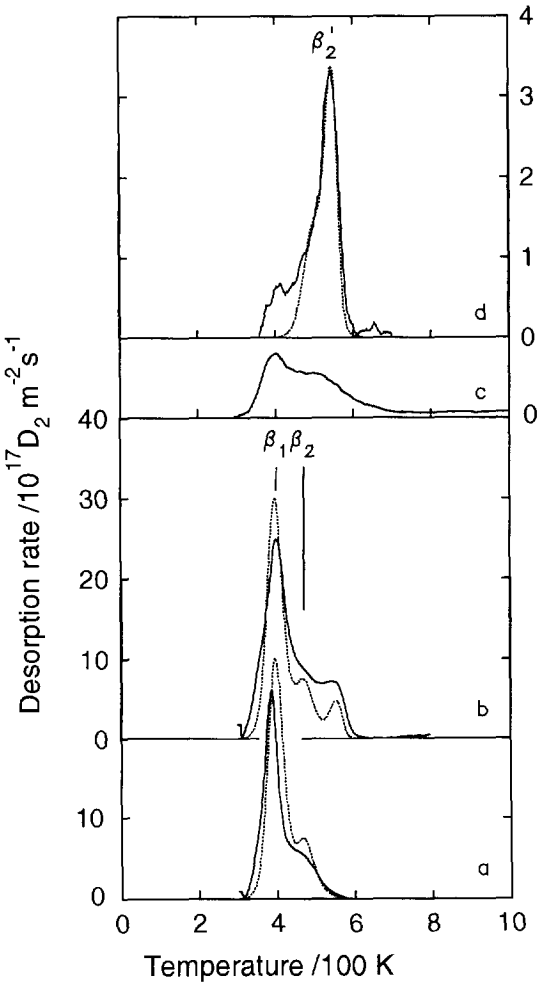

Fig. 4.9. Experimentally obtained desorption spectra———, fitted spectra ·····; a) after D_2 adsorption (180 L), b) after 3 keV $3.2x10^{19}$ D_2^+ m^{-2} irradiation of clean W(100), c) after deuterium adsorption of an oxygen covered surface, d) after 3 keV $3.2x10^{19}$ D_2^+ irradiation of an oxygen covered W(100).

vacancies as well as from the surface is shown. At enthalpies $E_{HV}^{D,H} \geq 1.3$ eV desorption is dominated by deuterium vacancy dissociation. In other words no delay is caused by surface recombination. From the above mentioned agreement with experiments with oxygen covered surfaces (fig. 4.9d and fig. 4.10) it follows that no extra barrier (> 0.1 eV) is caused by oxygen (at least for low coverages up to 1 ML). Another argument for this is given by comparing 3 keV irradiations experiments at clean surfaces (fig. 4.5) and oxidized surfaces (fig. 4.6). The β_2' peak remains at 550 K.

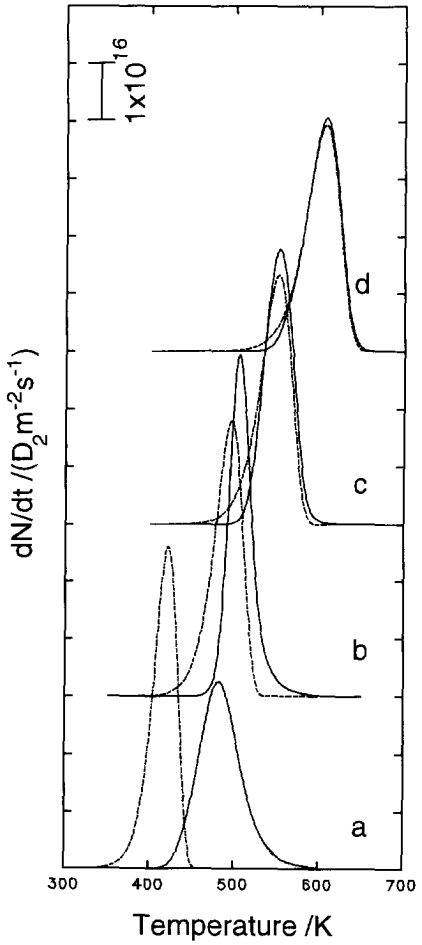

Fig. 4.10. Simulated spectra to determine the effect of surface traps on the desorption from subsurface defects. ▬▬ D_2 desorption from the surface, ▬··▬ D_2 desorption from a vacancy. Parameters used in the spectra: H_2 = 0.6 eV, N_V = $2x10^{18}m^{-2}$, N_0 = $2x10^{19}$ m^{-2} and (a) H_V = 1.1 eV, (b) H_V = 1.3 eV, (c) H_V = 1.45 eV, (d) H_V = 1.6 eV.

Table I Experimentally observed desorption temperatures for deuterium and hydrogen from tungsten and estimates (exp. and theor.) of dissociation parameters.

Temperature / K heating rate /Ks^{-1}	peak/ site	dissociation enthalpy /eV	attempt frequency / s^{-1}	ref.
400/10	β_1	0.48	$5x10^{11}$	a
450/25	β_1	0.52	$1x10^{12}$	b1
	β_1	0.49	$1x10^{10}$	b2
/isothermal	β_1	0.45	$1x10^{9}$	c
450/10	β_1	0.76	$1x10^{13}$	d
450/25	β_1	0.58	$1x10^{13}$	e
	β_1/β_2	0.58	-	j
500/10	β_2	0.60	$1x10^{13}$	a
550/25	β_2	0.92	$1x10^{18}$	b1
	β_2	0.83	$1x10^{17}$	b2
/isothermal	β_2	0.77	$1x10^{16}$	c
500/10	β_2	0.79	$1x10^{17}$	d
550/25	β_2	0.71	$4x10^{13}$	e
550/10	$\beta_2^{'}$ =DV	1.43	$1x10^{13}$	a
450/10	H InV_2	1.55	$2x10^{14}$	f
	HV	1.54^k		g
400-550/10	D_mV	< 1.43	$1x10^{13}$	a+h
400	H_2InV_2	1.38	$2x10^{14}$	f
	H_mV	<1.54		g
400-700/10	$He_iD_mV_n$	1.2-1.8	$1x10^{13}$	a
550-850/4	D_mV_n			i
610-735/ isothermal	D_mV_n	1.3-1.5	$8.4x10^{12}$	j
600-700/10	voids created by MeV H^+	>1.4 (TDS) 1.0-1.4 (PA)		l

a) [Eleveld et al.,12], b) [Horlacher Smith et al.: b1) TDS work, b2) LEED work,16], c) [Alnot et al.,17], d) [Ionaka and Yoshimori, 22], e) [Tamm and Schmidt,14], f) [Fransens et al.,19], g) [Nordlander et al.,20], h) [Eleveld et al.,11], i) Erents[24], j) [R.A. Anderl et al.,21], k) assuming a migration enthalpy of 0.39 eV, l) [van Veen et al.,23].

The absence of a barrier at the surface for the D-O-W system, supports the blocking model of Wampler [7], instead of the activation barrier model of Pick [5].

4.6 Vacancy type defects, nitrogen covered surfaces

4.6.1 Nitrogen desorption

Desorption spectra of nitrogen from surfaces exposed to nitrogen

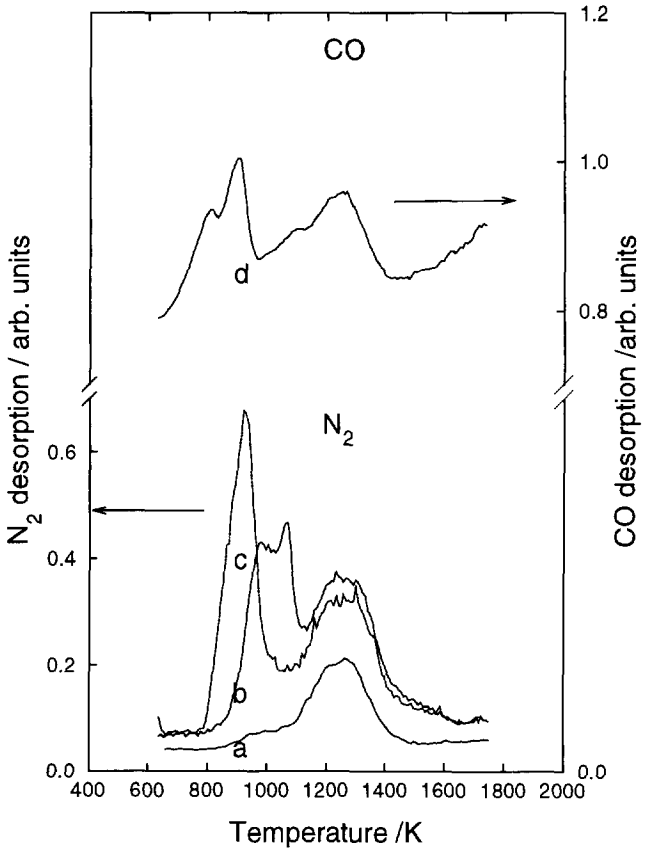

Fig. 4.11. Nitrogen desorption spectra obtained for a) saturation coverage of nitrogen adsorbed from the gas phase, b) 1 keV $3x10^{19}$ N_2^+ cm^{-2} and c) 2 keV N_2^+ (same dose as b), d) the CO desorption spectrum of a CO-covered surface.

from the gas phase (180 L) and from nitrogen ion irradiated surfaces are shown in fig. 4.11. With AES it was detected that following these treatments, nitrogen was the main impurity present at the surface. To be sure that the spectra recorded with the mass-spectrometer tuned on mass 14 (N^+) was not an effect of CO co-adsorption (CO may appear as mass 14 in a mass-spectrum as CO^{++}), spectra of CO-adsorbed surfaces were also made. With the quadrupole mass spectrometer tuned at mass 28, CO desorption spectra (fig. 4.11) could be reproduced at mass 12 (C^+ from dissociated CO), but were clearly different from spectra recorded at mass 14. The recorded CO spectrum contained the peaks reported in literature [25].

The nitrogen desorption spectra of nitrogen covered W(100) surfaces can be compared with literature results [25-27]. The broad peak centered at 1280 K is ascribed to fourfold adsorption sites of nitrogen at the W(100) surface. Irradiation with keV N_2^+-ions causes the appearance of extra nitrogen desorption peaks at temperatures lower than the 1280 K peak. In fig. 4.11 a peak at 900 K is observed for 1 keV irradiation and peaks around 1000 K for 3 keV irradiation. The peak contents increase with increasing dose. Clavenna and Schmidt [25] also found an extra peak after high nitrogen exposure at low temperatures (78 K). Sellidj and Erskine [29] using EELS-experiments described the new peak as a new surface site (bridge site). Also Lee and Madix [27] found an extra peak.

The effects shown in figure 4.11 can be explained by assuming that the amount of nitrogen implanted in excess of the saturation amount in fourfold sites at the surface has a weaker binding to the surface. When the nitrogen atoms are released from nitrogen defect complexes below the surface, they will not be retrapped at the surface, but will recombine and desorb without delay as molecules at the dissociation temperature of the defect complexes. In the 3 keV spectrum additional peaks, at higher temperatures can be seen than in the 1 keV spectrum. We ascribe this to formation of larger defect complexes.

4.6.2 Deuterium desorption from nitrogen covered surfaces

Deuterium desorption spectra of D_2-exposures and D_2-irradiation of

nitrogen covered surfaces are displayed in fig. 4.12. As with oxygen coverage (section 4.3), at full nitrogen covered surfaces no deuterium can be accommodated. On the other hand at lower coverages deuterium desorption spectra can be obtained showing β_1 and β_2-peaks. For low implantation doses of 1 keV D_2^+-ions an extra desorption peak is observed in the temperature range around 700 K because of D_2 detrapping from a nitrogen-vacancy complex. This site is rapidly saturated when the dose is increased. The major effect of deuterium implantation of nitrogen covered

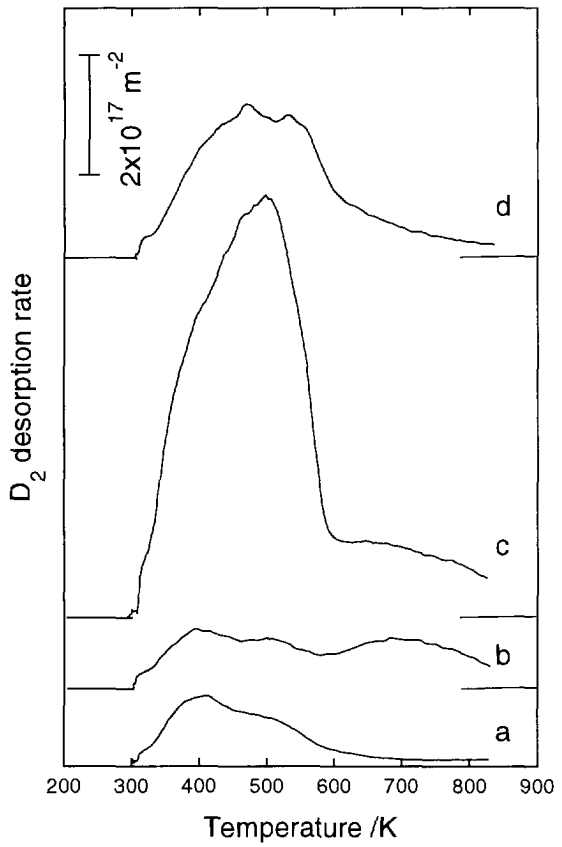

Fig. 4.12. Deuterium desorption spectra obtained for a) deuterium adsorbed on a nitrogen covered surface, b) 1 keV D_2^+ irradiated ($9x10^{18}$ m^{-2}) nitrogen covered, c) 1 keV D_2^+ irradiated ($1x10^{20}$ m^{-2}) nitrogen covered, d) 1 keV D_2^+ ($3x10^{19}$ m^{-2}), preimplanted with 1 keV N_2^+ ($3x10^{19}$ m^{-2}). Note that the spectra have been shifted vertically.

or implanted surfaces is the growth of the β_1 and β_2' desorption peaks. The β_2' peak growth can be compared with oxygen covered surfaces (section 4.4), whereas the desorption at lower temperatures can be explained by multiple filled vacancy-complexes. The binding energy is lower for deuterium trapped in a complex already occupied by a deuterium atom [20,19,30].

4.7 N-V dissociation

Nitrogen interaction with vacancies is the topic of this section. Low dose nitrogen (3 keV $5x10^{16}$ m^{-2} N_2^+) is used to create vacancy type defects. The recovery of vacancy type defects during anneal is monitored with thermal helium desorption spectrometry (THDS). To avoid creation of additional point defects by the helium ions the ion energy was kept low (300 eV $1x10^{17}$ m^{-2} He^+). In figure 4.13 the peak content versus the anneal temperature is shown. It must be remarked that the post nitrogen irradiation anneal was done at a heating rate of 40 Ks^{-1}. The sequence of actions during an experiment is described in table II.

Table II Sequence of actions during an experiment

step nr.	experimental action	intended action in crystal
1	3 KeV $5x10^{16}$ m^{-2} N_2^+ irradiation	creation of point defects (V , NV, V_2, etc.)
2	(40 Ks^{-1}) anneal to a specific temperature	removal of some point defects
3	300 eV $1x10^{17}$ m^{-2} He^+ irradiation	decoration of remaining defects with He
4	Thermal helium desorption spectrometry	He release

In figure 4.13 several observations can be made by following the contents of the E, F and G, H peaks and their totals. The peak assignments of E,F,G and H- peaks ($He_nV \rightarrow He_{n-1}V + He$ with n=5-9,4-3,2 and 1 respectively) can be found in [31]. The contents of an extra peak (H') is left out. At increasing temperatures the total peak content increases with temperature. At 700 K the total peak content is decreasing and at 1000 K it decreases faster with temperature. For the H peak the content is constant up to 700 K, before it falls off to lower values The behaviour of the H peak is modelled and will be explained below. The F and G peak contents are increasing up to an anneal temperature of 700 K but then decrease. At

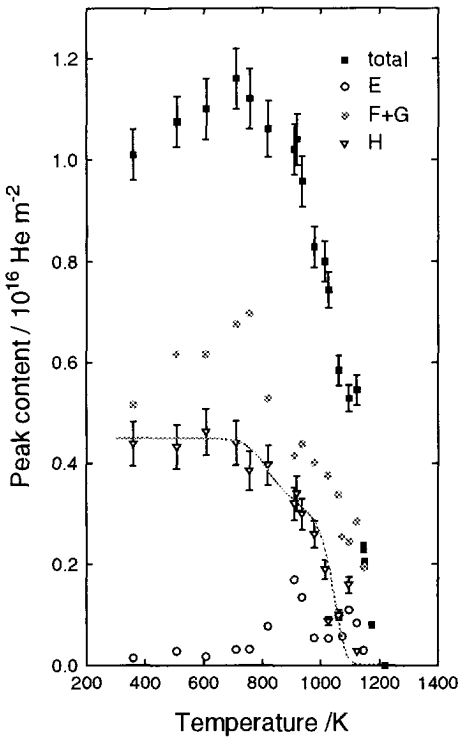

Figure 4.13 Helium peak content vs. anneal temperature. The desorption experiments followed the 4 steps procedure described in table II. The line resulted from modelling as explained in the text.

relatively low temperatures the content of the E peak is small. At 800 K the content of the E peak increases, and after a maximum at 900 K it decreases to lower values.

The behaviour of the peak contents can be explained, following the stages in the figure. At 500-550 K nitrogen is mobile in tungsten, E_N^M = 1.3eV [9]. The vacancies then become decorated with nitrogen, N + V → NV. The average He occupation of a vacancy is increased due to an increased trap probability most likely as a result of a nitrogen induced enlargment of the vacancy radius.

The second stage, the decrease of the total, F, G and H peak content at 800 K, can be ascribed to vacancy migration (V→$\tilde{V}$). For the H peak content the vacancy migration is fitted with $D_0 = 4.1\text{x}10^{-7}\,\text{m}^2\text{s}^{-1}$, using $D_0 = \lambda^2 \nu_0/6$ and $\nu_0 = 1\text{x}10^{14}$, and an activation energy of E_V^M = 1.8 eV [32]. The depth profile of the vacancies was estimated using 1.5 keV N^+ in TRIM91 [33], and was fitted with a Gaussian. The resulting profile, projected range 1.85 nm and standard deviation of 1.61 nm, and vacancy properties were used in the DIFFUSION computer code (chapter 3) solving equation (3.27 a) without the sink and source terms.

The defects surviving an anneal to 1000 K, must be ascribed to NV defects, since a V_2 (divacancy) will not survive this temperature [31]. The third stage shows a rapid decrease in the contents of the H peak. This stage indicates the reaction NV → N + V, and was modelled with a first order desorption. An activation energy was found of $E_{N,V}^D$= 2.70 ± 0.05 eV, and a attempt frequency of $1\text{x}10^{13}$ s^{-1}. From this it must be concluded that the above mentioned H peak must be ascribed to a HeNV dissociation, instead of an HeV. Figure 4.11 already showed N_2 desorption at 900-1000 K, at an desorption rate of 10 K s^{-1}, supporting the conclusion of the NV dissociation at this temperature. When melting temperatures are considered the results of the NV dissociation energy in tungsten are in good agreement with results on molybdenum in literature [34,35], where 2.55 eV was reported for the same reaction.

4.8 C-V dissociation

Carbon interaction with vacancies are studied using procedures

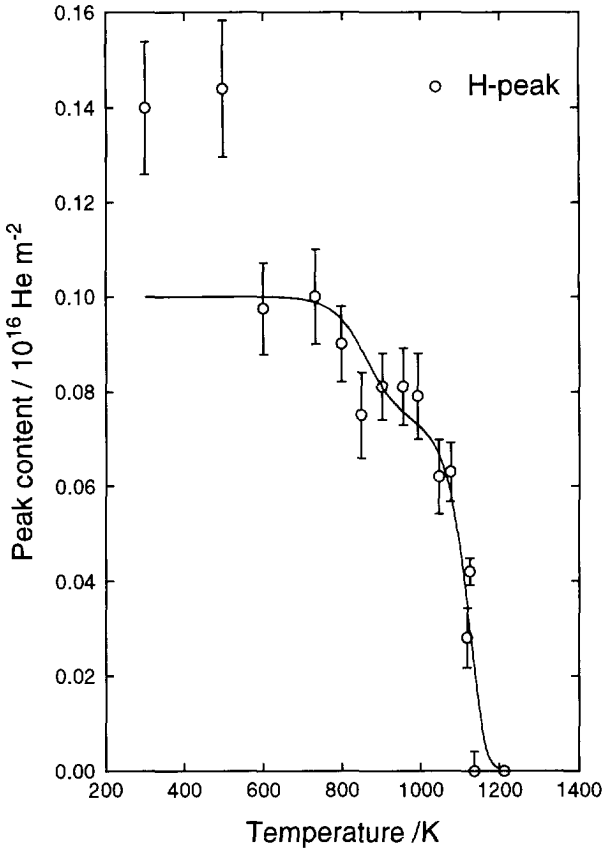

Fig. 4.14a. Helium peak (H) content vs. anneal temperature. The figure is a result of a series of experiments which followed the sequence comparable to the sequence of table II. W(100) irradiation with $8x10^{16}$ m^{-2} 3 keV CH_4^+, anneal to the indicated temperature and followed by a $1x10^{17}m^{-2}$ 300 He^+ probe injection. The line resulted from modelling as explained in the text.

analogous to those used to investigate the nitrogen vacancy interaction in the previous section (table II). Vacancies are created with 3 keV $8x10^{16}$ m^{-2} CH_4^+ ions, followed by an anneal to a predetermined temperature and a heating rate of 40 Ks^{-1}. The defects remaining at this temperature are then probed with 300 eV $1x10^{17}$ m^{-2} He^+, which is followed by thermal helium desorption spectrometry. The results of the experiments are shown in figure 4.14a and b. In figure 4.14a the content of the H peak is plotted versus the anneal temperature, in figure 4.14b the total peak content and the H peak

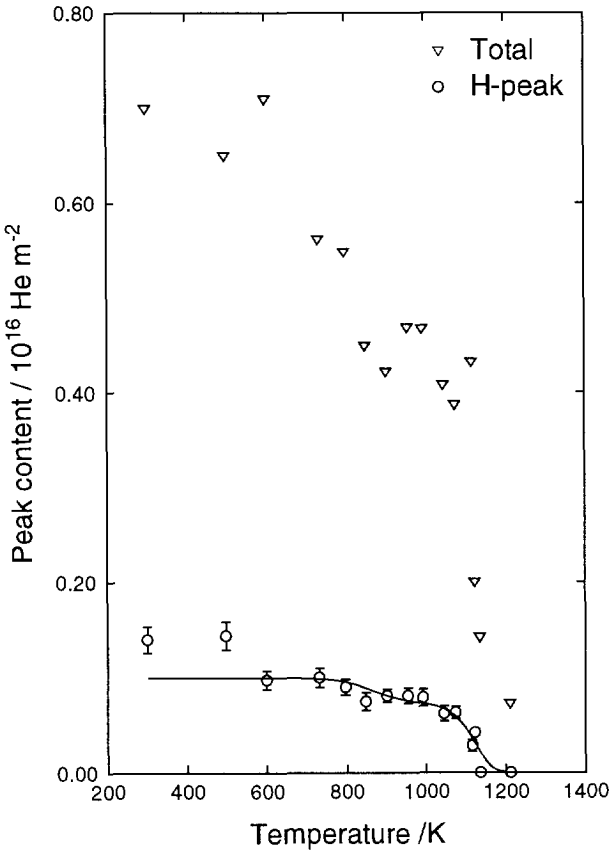

Fig. 4.14b. Helium peak content vs. anneal temperature. The figure is a result of a series of experiments which followed the sequence comparable to the sequence of table II. W(100) irradiation with $5x10^{16}$ m^{-2} 3 keV N_2^+, anneal to the indicated temperature and followed by a $1x10^{17}$ m^{-2} 300 He^+ probe injection. The line resulted from modelling explained in the text.

content vs anneal temperature are displayed.

The decrease at 600 K can be ascribed to carbon diffusion. At this temperature carbon is becoming mobile [36]. The vacancies become decorated with C atoms, and cannot be filled with helium. This is in contrast with the N decoration of vacancies.

As in the previous section the H peak content vs temperature is modelled with a diffusion and a dissociation stage. The stage at 800 K is

modelled with vacancy migration in the computer code DIFFUSION. The data for the vacancy migration are the same as in the previous section: $D_0 = 4.1\text{x}10^{-7}\ m^{-2}s^{-1}$, using $D_0 = \lambda^2 \nu_d/6$ and $\nu = 1\text{x}10^{14}$, and an activation energy of $E_V^M = 1.8$ eV. The depth profile of the vacancies was estimated using 2.25 keV C^+ in TRIM91, and was fitted with a Gaussian giving a profile with a projected range of 2.73 nm and sigma of 2.48 nm.

The stage at 1150 K is ascribed to carbon vacancy dissociation, using similar reasoning as applied in the previous section. An activation energy of $E_{C,V}^D = 2.9$ eV and a attempt frequency of $1\text{x}10^{13}\ s^{-1}$ were found for this stage.

From the above C-V dissociation reaction it must be concluded that the identified H peak in the (not shown) helium desorption spectra must be ascribed to HeCV dissociation.

In table III some point defect properties and their activation energies in tungsten are displayed.

Table III Point defect properties in tungsten.

Reaction	Temperature /K	Energy /eV	Reference
$N \rightarrow N_{mobile}$	500-600	1.24-1.56	[9]
$C \rightarrow C_{mobile}$	~600	1.65	[36]
$V \rightarrow V_{mobile}$	~900	1.8	[32]
NV→N+V	~1050	2.7	this work
CV→C+V	~1100	2.9	this work

4.9 Conclusions

Progress has been made in developing deuterium desorption spectrometry (i) as a tool for monitoring subsurface defects and (ii) for deuterium defect interaction studies. It appears that the problem of deuterium surface retrapping can successfully be overcome by covering the

surface with oxygen. This is important since detrapping of deuterium from subsurface defects then is no longer obscured by surface effects. The results obtained for detrapping from defects are generally well in line with results obtained with other techniques. A model proposed to describe the deuterium desorption from the surface and subsurface defects gave satisfactory results. A dissociation enthalpy of 1.43 eV and a attempt frequency of $1x10^{13}$ s^{-1} was found for deuterium vacancy dissociation. The model indicated that oxygen causes no extra energy barrier (> 0.1 eV). The experiments showed that vacancies can be produced by recoil implantation of the oxygen (D→O→W). The number of trapped deuterium atoms, injected with 0.5 keV per ion, depends on the oxygen coverage of the surface. Deuterium desorption experiments at nitrogen covered W(100) crystals showed a similar behaviour.

Impurity (N,C) vacancy dissociation was studied by thermal helium desorption spectrometry. After impurity ion injection the remaining defects have been annealed out in two stages. The stage at 800 K was ascribed to vacancy mobility. The anneal step was modelled with D_0 = $4.1x10^{-7}$ m^2s^{-1} and an activation energy of E_V^M = 1.8 eV. The defects residing in the crystal after heating the crystal to 1000 K are ascribed to impurity vacancy complexes (NV's and CV's). The NV and CV dissociation were modelled with activation energies of $E_{N,V}^D$ = 2.70 and $E_{C,V}^D$ = 2.90 eV respectively, while the attempt frequency was found to be $1x10^{13}$ s^{-1}.

Overall the experimental work together with the modelling has significantly improved our understanding of impurity-vacancy interactions in tungsten.

Literature

[1] S.M. Myers, P.M. Richards, W.R. Wampler and F. Besenbacher, J. Nucl. Mater. **165** (1989) 9.

[2] S.M. Myers, M.I. Baskes, H.K. Birnbaum, J.W. Corbet, G.G. DeLeo, S.K. Estreicher, E.E. Haller, P.Jena, N.M. Johnson, R. Kirchheim, S.J. Pearton, M.J. Stavola, Rev. Mod. Phys. **64** (1992) 559.

[3] W. Möller and J. Roth, Physics of plasma wall interactions in Controlled Fusion (NATO ASI series, Plenum, New York, 1986)

p.439.
[4] M.A. Pick and K. Sonnenberg, J. Nucl. Mater. **131** (1985) 208.
[5] M.A. Pick, J. Nucl. Mater. **145-147** (1987) 297.
[6] W.R. Wampler, Appl. Phys. Lett. **48** (1986) 405.
[7] W.R. Wampler, J. Nucl. Mater. **145-147** (1987) 313.
[8] W.R. Wampler, J. Appl. Phys. **65** (1989) 4040.
[9] H. Jehn, in: Gase und Kohlenstoff in Metallen, eds. E. Fromm and E. Gebhardt (Springer Verlag, Berlin , 1976).
[10] A. van Veen, J. of Trace and Microprobe Techniques **8** (1990) 1.
[11] H. Eleveld and A.T. Dijksman and A. van Veen, in Proc. 16th Symp. on fusion Technology (SOFT, London, 1990) p. 376.
[12] H. Eleveld and A. van Veen, J. Nucl. Mater **191-194** (1992) 433.
[13] P.M. Richards, S.M. Myers, W.R. Wampler and D.M. Follstaedt, J. Appl. Phys. **65** (1989) 180.
[14] P.W. Tamm and L.D. Schmidt, J. Chem. Phys. **51** (1969) 5352.
[15] D.A. King and G. Thomas, Surf. Sci. **92** (1980) 201.
[16] A. Horlacher Smith, R.A. Barker and P.J. Estrup, Surf. Sci. **136**(1984) 327.
[17] P. Alnot, A. Cassuto and D.A. King, Surf. Sci. **215** (1989) 29.
[18] J.P. Biersack and L.G. Haggmark, J. Nucl. Instr. and Meth. **174** (1980) 257.
[19] J.R. Fransens, M.S. Abd El Keriem and F. Pleiter, J. Phys. Cond. Matter. **3** (1991) 9871.
[20] P. Nordlander, J.K. Nørskov, F. Besenbacher and S.M. Myers, Phys. Rev **B40** (1989) 1990, and J. Phys. **F16** (1986) 1161.
[21] R.A. Anderl, D.F. Holland, G.R. Longhurst, R.J. Pawelko, C.L. Trybus and C.H. Sellers, Fusion Technology **21** (1992) 745.
[22] T. Inoaka and A. Yoshimori, Surf. Sci. **149** (1984) 327.
[23] A. van Veen, H.A. Filius, J. de Vries, K.R. Bijkerk, G.J. Rozing and D. Segers, J. Nucl . Mater. **155-157** (1988) 1113.
[24] S.K. Erents, Proc. 8th Symp. on Fusion Technology (SOFT) Utrecht, The Netherlands, 1974, p.895.
[25] L.R. Clavenna and L.D. Schmidt, Surf. Sci. **33** (1972) 11.
[26] T. Tamura and T. Hamamura, Bull. Chem. Soc. Jap. **49** (1976) 1780.
[27] J. Lee and R.D. Madix, Surf. Sci. **143** (1984) 626.
[28] L.R. Clavenna and L.D. Schmidt, Surf. Sci. **22** (1970) 365.

[29] A. Sellidj and J.L. Erskine, Surf. Sci. **220** (1989) 253.
[30] M.S. Abd El Keriem, D.P. van der Werf and F. Pleiter, Hyperfine Interactions **79** (1993) 783.
[31] A. van Veen, Mat. Sc. For. **15-18** (1987) 3.
[32] J. Koehler, J. Nucl. Mater. **169** (1989) 3.
[33] J.P. Biersack and L.G. Haggmark, J. Nucl. Instr. and Meth. **174** (1980) 257.
[34] H.A. Filius and A. van Veen, J. Nucl. Mater. **144** (1987) 1.
[35] A. van Veen and L.M. Caspers, Solid State Comm. **30** (1979) 761.
[36] A. Shepela, J. Less Comm. Metals **26** (1972) 33.

Chapter 5.

Vacancy cluster growth in tungsten

5.1 Introduction

An overview on hydrogen interactions with point defects and helium bubbles in tungsten and other metals has been given by Myers et al. [1]. Recent hydrogen permeation studies are performed by Longhurst [2], Anderl et al. [3] and Gervasini and Reiter [4]. Hydrogen interaction with voids in 6 MeV electron and proton irradiated tungsten was studied by van Veen et al. and Rozing et al. [5,6,7] using positron annihilation and thermal gas desorption. Earlier Erents [8] employed the thermal desorption technique to observe deuterium release after 20 keV deuterium ion injection. Andrew and Pick reported deep traps for ^3H in tungsten as a drawback for using tungsten as a plasma facing material [9]. Other aspects of deuterium interaction with point defects in tungsten are reported by some authors [10,11,12]. Experiments on microstructural evolution in molybdenum during hydrogen ion irradiation have been performed by Sakamoto et al. [13] and helium induced swelling in tungsten is reported by Chernikov [14].

In this chapter, vacancy clusters and voids are described which were created by 15 keV deuterium ion irradiation and subsequent annealing. The voids were probed by deuterium and positrons. Nitrogen is used as a model for impurities to observe the role of impurities in voids. Also, deuterium interaction with helium bubbles is studied. Diffusional rate theory is applied to describe deuterium desorption from voids.

5.2 Hydrogen interaction with voids, surface impurity coverage related trapping

In this section, the effect of deuterium dose variation, impurity surface coverage and anneal temperatures on the deuterium desorption spectra is described. The results on deuterium behaviour in tungsten reported in this and following sections are discussed in section 5.8.

Dose variation

Using 30 keV deuterium molecule ions (D_2^+) deuterium particles (D^+) are injected with 15 keV. The effect of deuterium dose variation on the peaks contributing to the thermal desorption spectra is demonstrated by the spectra shown in figure 5.1. The lowest dose shows a deuterium release peak at 550 K. At increasing dose deuterium is released in peaks at temperatures ranging from 350 K to 650 K. At high doses in excess of $5x10^{19}$ D_2^+ m^{-2} an additional desorption peak is found at 800 K.

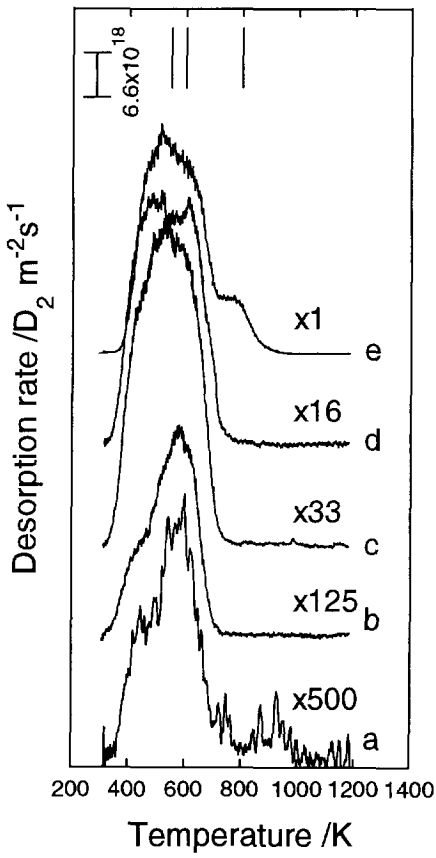

Fig. 5.1. Thermal deuterium desorption from tungsten irradiated with 30 keV D_2^+ at varying dose (a) $2x10^{17}$ m^{-2}, (b) $8x10^{17}$ m^{-2}, (c) $3x10^{18}$ m^{-2}, (d) $6x10^{18}$ m^{-2}, (e) $1x10^{20}$ m^{-2}. Note that the y-axes are shifted for every spectrum.

30 keV D_2^+ probing of annealed sample containing defects

In figure 5.2, spectra are shown for experiments where deuterium is used as a probe for defect clusters evolving during annealing of a sample pre-irradiated with a high dose: $1x10^{20}$ D_2^+ m^{-2}. From the figure, it can be seen that at the three lowest anneal temperatures 1040 K to 1290 K, D_2 subsequently desorb in a peak at 800 K. As the anneal temperature is increased, this peak quickly disappears and is replaced by a lower temperature peak at ≈ 600 K. The peak shifts to ≈ 550 K when the crystal is annealed to the higher temperatures.

In figure 5.3a, the amount of released deuterium versus the anneal

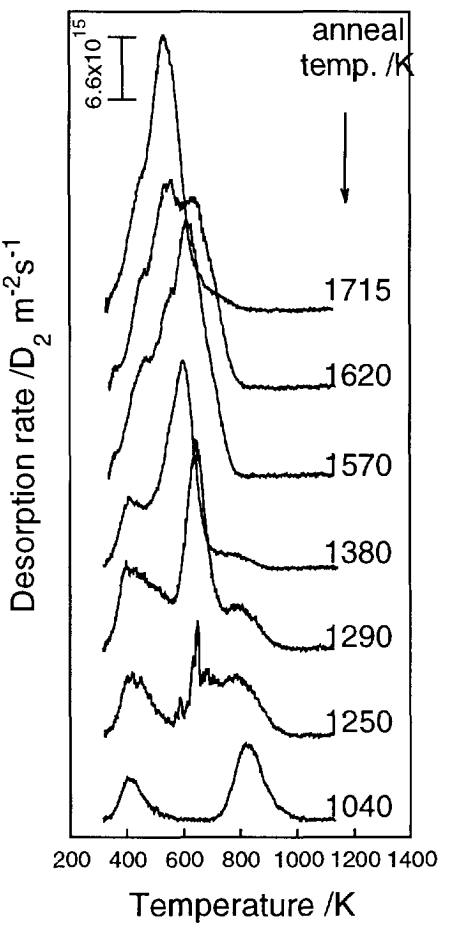

Fig. 5.2. Thermal deuterium desorption from small voids in tungsten, annealed to the indicated temperature. Note that the y-axes are shifted for every spectrum.

temperature is displayed. The data are from two series of experiments. The data of the first series were adjusted, according to the oxygen coverage of the surface (see the next subsection).

In the second series, the surface was prepared by a one minute anneal at 1600 K in oxygen prior to the experiments and thus passivated. From figure 5.3a it can be seen that the amount detrapped in the 800 K peak decreases with increasing anneal temperature. At 1350 K this peak has disappeared. Thus, the defect causing the 800 K peak has been removed by annealing. After annealing to 1350 K the peak content of the 600 K peak increases. The peak content arrives at a maximum at an anneal temperature around 1500 K. At higher anneal temperatures this peak also disappeared,

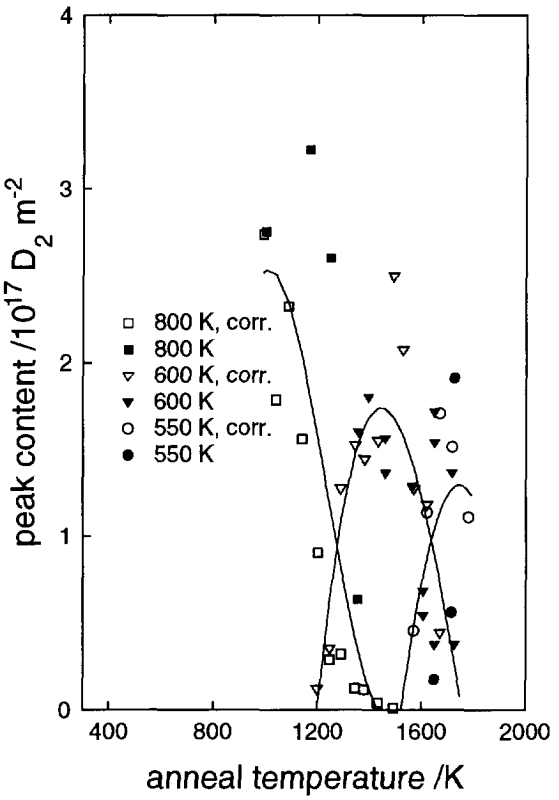

Fig. 5.3a. Populations of the 550, 600 and 800 K peaks vs anneal temperature. The probe dose was $4x10^{17}$ D_2^+ m^{-2} and the energy 30 keV. The open symbols are results from the surface coverage corrected surface. The filled symbols are results from a series with passivated surface. The lines are drawn to guide the eye.

in favour of the growth of the deuterium desorption peak at 550 K.

Impurity surface coverage dependent deuterium trapping

Oxygen coverage building up during the experiments did change the ability of deuterium to recombine at the surface. Therefore, the trapping rate of the deuterium at the defects varied considerably during the anneal. In figure 5.3b the surface coverage of the impurities oxygen, carbon and nitrogen, as measured with AES, are displayed versus the anneal temperature. The oxygen surface coverage was used to correct the data of the first series. The

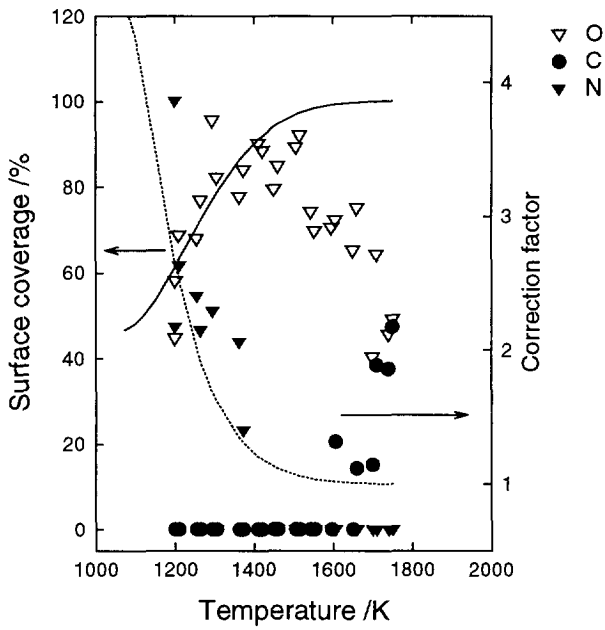

Fig. 5.3b. Impurity coverage as measured with AES vs anneal temperature of the first series of 30 keV deuterium probe experiments. The oxygen coverage is fitted with a polynomial. The fit is used in a correction factor that is plotted with respect to the right axis.

oxygen coverage vs temperature was therefore fitted with a 5th order polynomial. The applied correction of the termal desorption data was as follows:

$$corrected\text{-}data(T) = measured\text{-}data(T) \times (polynomial(T))^{-2}.$$

The correction term, $(polynomial(T))^{-2}$, is also shown in figure 5.3b, which shows that the measured data at relatively low anneal temperatures had to be corrected with a factor 4. At temperatures above 1600 K the correction factor dropped to 1. The correction term implies that oxygen coverage enhances the deuterium content of the crystal during implantation.

The effect of the oxygen coverage of the surface is in agreement with the results shown in section 4.5, where is was stated that oxygen coverage leads to blocking of surface sites. Accordingly, when oxygen is present, deuterium cannot penetrate the surface from vacuum to the bulk or back.

5.3 Positron annihilation experiments

In this section the recovery of the tungsten crystal from defects during anneals is monitored by the positron annihilation technique. A description of the positron annihilation technique can be found in chapter 2. As is described in the previous section for the thermal desorption experiments, the tungsten (100) crystal is pre-irradiated with 30 keV $1x10^{20}$ D_2^+ m^{-2}. The PA experiments were carried out to relate the peak content behaviour with temperature, displayed in fig. 5.3, to open volumes.

The results with the PA technique are given in figure 5.4. The

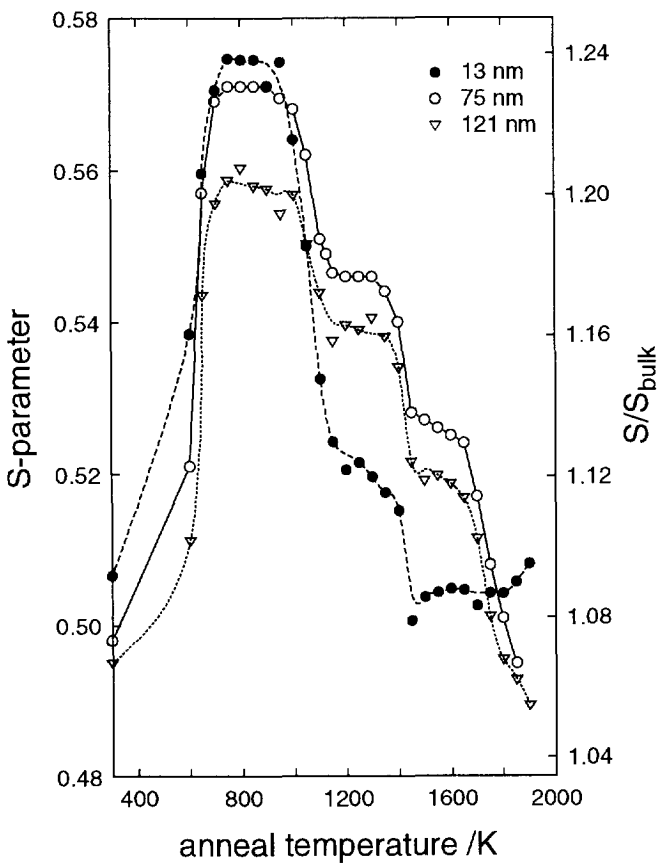

Fig. 5.4. Results from positron beam experiments; S-parameter versus annealing temperature for positrons implanted with energies of 3.1, 9.2 and 12.3 keV, corresponding with average depths of 13, 75 and 121 nm respectively.

Doppler broadening parameter S versus annealing temperature is shown. In the graph several features are observed. Three zones centred around depths, of 13, 75 and 121 nm, are probed with positrons with energies of 3.1, 9.2 and 12.3 keV respectively. The deuterium ions have been stopped at a depth of 75 nm with a straggling of 34 nm as calculated with TRIM [15]. The annealing curves show a sharp increase of the S parameter at 650 K. Two further anneal steps for all three curves can be seen at 1000 K and at 1450 K. For the curves with 75 nm and 121 nm probe depths, an additional annealing stage is seen at 1700 K.

5.4 Results of atomistic calculations on vacancy clusters

In the previous section it was clear that several stages exist during the anneal of a tungsten crystal containing defects. As the variation of the S-parameter in the PA experiments indicates different types of open volumes, it is interesting to note that calculations has been carried out on vacancy clusters in tungsten. From these calculations on vacancy cluster dissociation using the Atom Embedded Method performed by Van Veen and Heringa [16,17], dissociation energy levels versus number of vacancies are available. These energy levels are with relative maxima associated with symmetric cluster configurations. The maxima are found for the cluster configurations $V_{4\text{-}10}$, $V_{11\text{-}16}$ and $V_{40\text{-}60}$.

5.5 Nitrogen filled vacancy clusters

The influence of impurities on the deuterium trapping in voids and desorption of hydrogen from voids is studied in this section. Voids in the crystal are created by 30 keV $1\text{x}10^{20}$ m^{-2} D_2^+ and a subsequent annealing for one minute to 1526 K. Nitrogen is used as the impurity and is injected in the crystal to increase the local impurity concentration. Probing took place with 30 keV $4\text{x}10^{17}$ D_2^+ m^{-2}. Deuterium release from these voids is expected around 600 K as can be seen in figures 5.2 and 5.3.

In figure 5.5 results are shown of deuterium probing experiments at nitrogen pre-irradiated tungsten. The nitrogen dose is varied in the experiments. The ion energy was kept at 3 keV N_2^+, i.e. about 1.5 keV per N atom, while the crystal temperature was kept at 460 K to mobilize the nitrogen so it can migrate to the void containing region. Figure 5.5 shows that deuterium desorption still takes place around 600 K, although the temperature at maximum desorption rate decreases. The total peak amount of deuterium is decreased at increasing dose, see also figure 5.6. However when the nitrogen dose is increased beyond $8x10^{18}$ m^{-2}, the deuterium peak amount is increased.

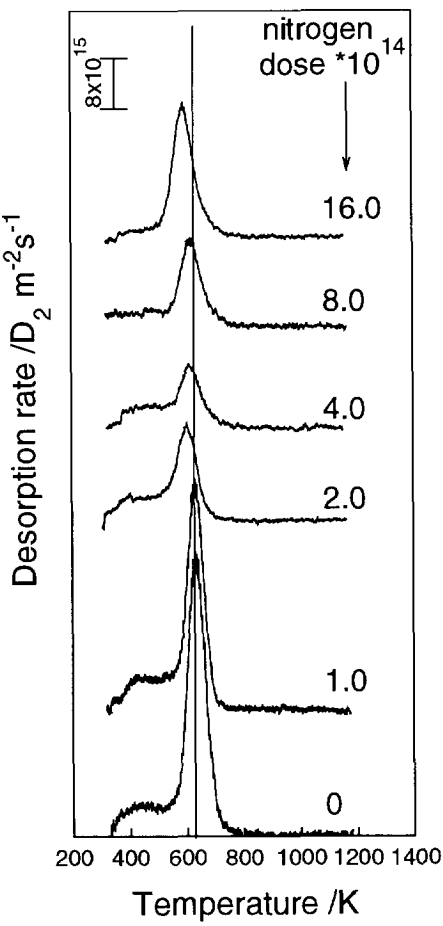

Fig. 5.5 Deuterium probing of nitrogen irradiated tungsten containing voids. The deuterium probe dose was kept at 30 keV, $4x10^{17}$ m^{-2}. The nitrogen is injected at 460 K and the ion energy was kept at 3 keV.

The effect of an anneal of the voids containing crystal and nitrogen on the deuterium desorption is shown in figure 5.7. In this case voids were created as mentioned above, which was followed by 3 keV $2x10^{18}$ N_2^+ m^{-2} at 460 K. Before deuterium probing, carried out with 30 keV $4x10^{17}$ D_2^+ m^{-2}, the crystal was annealed to the indicated temperature (at 10 K s^{-1}). The figure shows that an increase of the anneal temperature results in an increase of the deuterium peak amount.

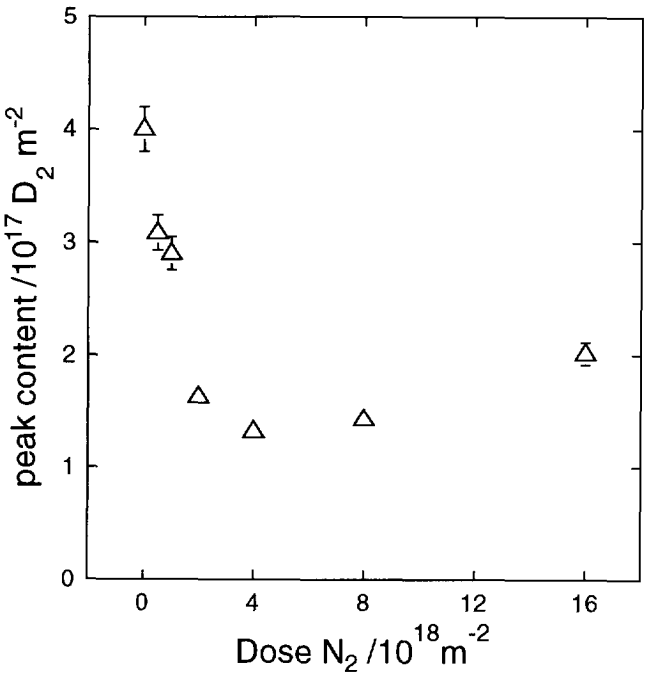

Fig. 5.6. Deuterium peak content vs nitrogen dose. Nitrogen is injected at 460 K and the ion energy was kept at 3keV. Deuterium probing with 30 keV $4x10^{17}$ D_2^+ m^{-2}.

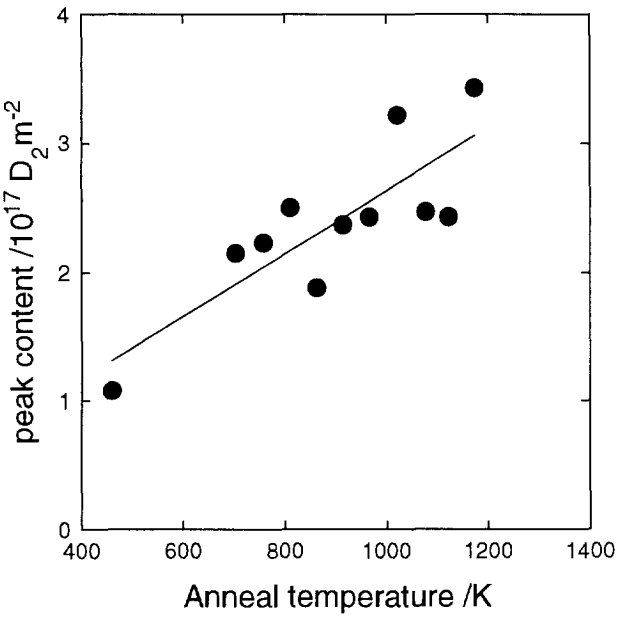

Fig. 5.7. Deuterium peak content vs anneal temperature. Prior to the annealings nitrogen is injected at 460 K, 3 keV ion energy and $2x10^{18}$ m^{-2}.

5.6 Deuterium interactions with helium bubbles

This section deals with the results of deuterium desorption experiments at helium bubbles in tungsten. Helium bubbles are produced with 3 keV He^+ $2x10^{19}$ m^{-2} and a subsequent heating to a high temperature (>1600 K) [16]. The target with helium bubbles, pre-annealed to specific temperatures, is probed with 600 eV D_2^+ to prevent creation of defects with deuterium.

In figure 5.8 thermal deuterium desorption results are shown of deuterium dose variation at a helium bubble containing sample. The helium bubbles were created with 3 keV He^+ $2x10^{19}$ m^{-2} and a subsequent heating to 1590 K (40 Ks^{-1}). It can be seen that at the lowest deuterium dose deuterium is released around 380 K. When the deuterium dose is increased to $2.2x10^{18}m^{-2}$ deuterium is also released around 700 K. At higher probe doses deuterium is found to release at 450 K and 530 K and at the previous mentioned temperatures. Comparable thermal desorption results are found

for deuterium ion (D_2^+) energies of 1 and 3 keV at these helium bubbles. Deuterium injected with 3 keV showed relative more desorption at 400 K.

Results of thermal desorption experiments of deuterium probed helium bubbles pre-annealed to 1935 K (120 seconds at this temperature) are shown in figure 5.9a. At the deuterium dose of $2x10^{18}$ m^{-2} deuterium desorption takes place at 400 K. At higher doses desorption peaks are also found at 500 and 530 K. The latter desorption peak was also present in figure 5.8. When the crystal is heated to 2065 K (120 seconds at this temperature) deuterium desorption is found around 380 K, see figure 5.9b. In figure 5.9b also the result of an adsorption experiment is included to

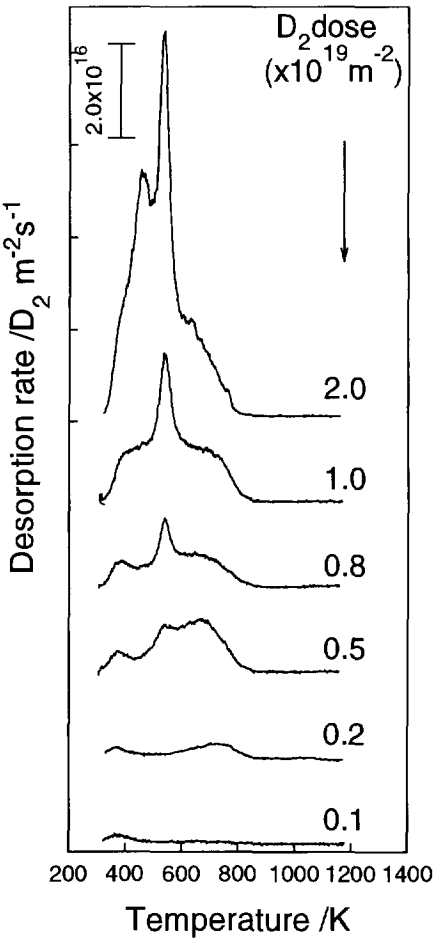

Fig. 5.8. Thermal deuterium desorption spectra of deuterium decoration of helium bubbles. The W(100) crystal with helium bubbles is pre-annealed to 1590 K. The D_2^+ ion energy was kept at 600 eV, while the dose was varied.

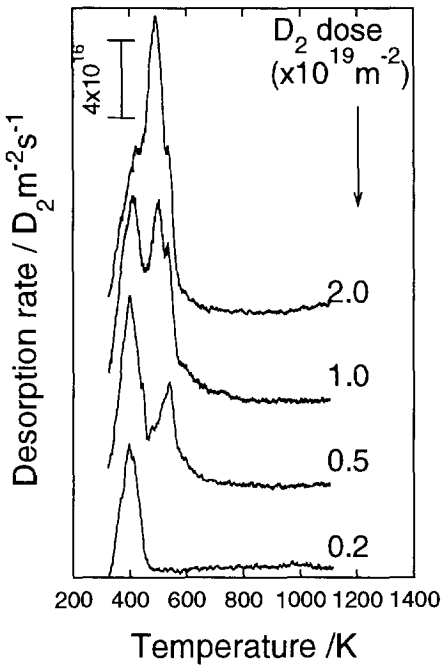

Fig. 5.9a. Thermal deuterium desoprtion spectra of deuterium decoration of helium bubbles. The W(100) crystal with helium bubbles was pre-annealed to 1935 K. The D_2^+ ion energy was kept at 600 eV, while the dose was varied.

show that the deuterium peak at 380 K is not an effect of deuterium desorption from adsorption sites.

The helium bubbles could be annealed out by flashing the crystal several times to 2200 K.

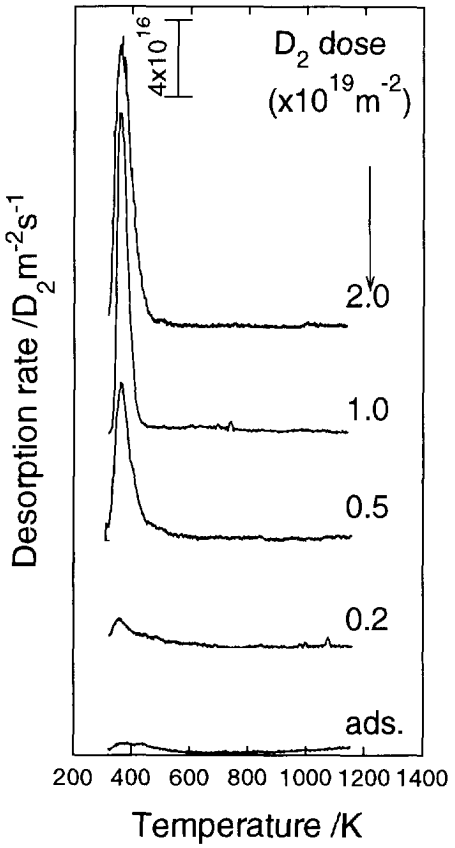

Fig. 5.9b. Thermal deuterium desoprtion spectra of deuterium decoration of helium bubbles. The W(100) crystal with helium bubbles was pre-annealed to 2035 K. The D_2^+ ion energy was kept at 600 eV, while the dose was varied.

5.7 Deuterium interactions with defects using diffusional rate theory

To understand the deuterium desorption from tungsten described in section 5.2, simulations with DIFFUSION, a model based on diffusion rate theory, were carried out. The diffusion rate theory is explained in chapter 3. In figure 5.2 the results of experiments showed deuterium release at lower temperatures when the crystal was pre-annealed to high temperatures.

When it is assumed that the deuterium concentration $c_{H,eq}$ (that is in balance with the concentration of adsorbed deuterium at internal sites and deuterium in the gas phase in the voids) is negligible compared to the concentration available sites for H interstitials, then formulae (3.1) and (3.2) can be simplified to

$$\frac{\theta}{1-\theta} = e_{eq} f_{eq} = c_{H,H_2} f_{H_2}, \tag{5.1}$$

with $f_{eq} = exp(H_D^D - H_H^M)$ and $f_{H2} = exp(H_I + \frac{1}{2}\mu_{H2})$. Using

$$N_s\theta + c_{H,eq} + 2\,c_{H,H_2} = \frac{c_{H,total}}{c_{voids}}, \tag{5.2}$$

the diffusion equation can be solved faster. From (5.1) it can be derived that

$$\theta = \frac{c_{H,eq} f_{eq}}{1 + c_{H,eq} f_{eq}},$$

and

$$c_{H,H_2} = c_{H,eq} f_{eq} / f_{H_2}.$$

When θ and c_{H,H_2} are substituted in formula (5.2) $c_{H,eq}$ can be found solving the quadratic equation. Only the positive definite solutions are used. Also, the concentration of hydrogen molecules in voids can be determined. The concentration of hydrogen adsorbed internally at voids and the interstitial hydrogen concentration are to be solved by the diffusion equation. Model calculations to understand this behaviour can be done with two assumptions.

First, one can assume that deuterium desorption at lower temperatures, when the crystal is probed after a high anneal temperature, is caused by a higher deuterium concentration in the voids. At increased deuterium pressures the chemical potential will rise and therefore deuterium will be released at lower temperatures. Calculations in chapter 3 showed that either a high deuterium/void ratio or a high impurity concentration must be assumed. Both options seem not to be very likely. A calculation of the vacancy cluster concentration at the implantation zone of 2.6×10^{19} m^{-2}, when it is assumed that every deuterium ion creates 8 vacancies and a 1

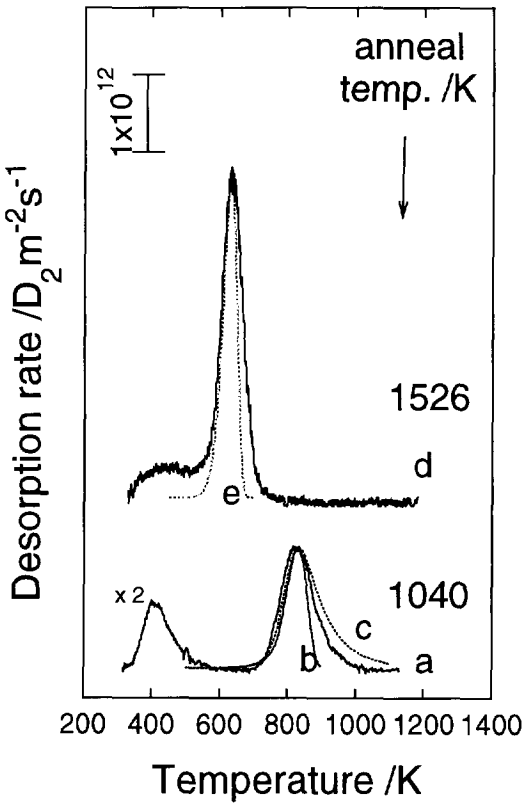

Fig. 5.10. Simulations and experimental deuterium desorption spectra. Selected TDS experiments of fig. 5.2. and fig. 5.5 a) TDS experiment after an anneal to 1040 K, b) simulation using a Gaussian depth profile of voids with a concentration of 2.6×10^{19} m^{-2} in the FWHM range, c) simulation using a depth independent void distribution with a concentration of 2.6×10^{19} m^{-2}, d) TDS experiment after an anneal to 1290 K and e) simulation using a Gaussian profile of voids with a concentration of 5×10^{15} m^{-2} in the FWHM range.

minute anneal to 1060 K creates an average of 12 vacancies per cluster and a factor 5 of the vacancies are lost to the surface. The deuterium probe will lead to a concentration of at most $4x10^{17}$ m^{-2}, giving a maximum deuterium/void ratio of 0.015. This ratio must be more than a factor 100 times the number of available sites per void higher to create a certain deuterium pressure in a void.

A second approach is to ascribe the lower deuterium desorption temperatures to lower void concentrations. Then (the diminishing) retrapping of deuterium by the voids is the origin of the deuterium desorption behaviour. A lower concentration of voids leads to a lower deuterium desorption temperature. In figure 5.10 simulations are performed using the diagram of figure 3.1.
The following parameters are used: $D_0^H = 4.1x10^{-7}$ m^2s^{-1}, $H_H^M = 0.39$ eV, $H^S =$ 1.0 eV [18], $H_D^D = 1.8$ eV and the chemical potential is derived with (3.11) and (3.13) using a diameter of the void of 1 nm, $2.6x10^{19}$ m^{-2} void concentration (i.e. concentration of available adsorption sites) in the FWHM range of the Gaussian depth profile (curve b in fig. 5.10), $2.6x10^{19}$ m^{-2} void concentration uniformly distributed (curve c in fig. 5.10) and $5x10^{15}$ m^{-2} void concentration in the FWHM range of the Gaussian profile (curve e). The number of injected hydrogen atoms is taken to be $4x10^{17}$ m^{-2}.

5.8 Discussion

The discussion of the results of the preceding sections is divided in vacancy cluster growth, nitrogen interactions with voids, diffusional rate calculations and helium bubbles.

Vacancy cluster growth

From the thermal desorption spectrometry (TDS) and positron annihilation (PA) results the following can be derived. During irradiation with 30 keV $1x10^{20}$ D_2^+ m^{-2} mono- and di-vacancies and some small vacancy clusters are created. At 550 K (10 K/s: referring to TDS isochronal anneals) deuterium is released from the monovacancies [10-12]. At approximately 600 K (0.8K/s referring to PA isochronal anneals) vacancies become

mobile [19] and form vacancy clusters. This is observed by an increase of the S parameter in figure 5.4. It is well documented that an increase of S indicates creation of open volumes [20]. Thus open volume formation followed deuterium leaving the vacancies and clustering of the mobile vacancies. From the same figure it can be seen that the S value remains constant from 750 up to 1000 K, indicating a stable situation. From calculations on vacancy cluster dissociation using the Atom Embedded Method performed by Van Veen and Heringa [16,17], dissociation energy levels versus number of vacancies are available. From [16] it can be concluded that clusters containing 4 to 10 vacancies can survive a one minute anneal only for temperatures lower than 1000 K. This stable configuration is not observed by thermal desorption merely because a post-irradiation anneal to 1200 K (isochronal annealing rate: 10K/s) was applied before performing the deuterium probing experiments. At increasing temperatures (1000 K - 1150 K) the small vacancy clusters dissociate and form clusters containing 11-16 vacancies (V_{11-16}). Decoration with deuterium of these vacancy clusters causes the deuterium desorption at 800K. This desorption peak was also observed by Erents [8]. Van Veen et al. [6] published results from thermal desorption of hydrogen detrapping from voids at temperatures ranging from 400K up to 1000 K. The maximum temperature corresponds with the findings of this work and the results of Erents. The next anneal stage takes place at approximately 1400 K. The V_{11-16} clusters break up or migrate until vacancy clusters are formed containing 40-60 vacancies. The numbers again are derived from the calculations presented in [16]. The experiments with deuterium decorated V_{40-60} show deuterium release at 600 K. This desorption peak was also found earlier [8]. At 1700 K the last annealing stage occurs. The V_{40-60} clusters have disappeared leaving no detectable defects. When the sample is probed by deuterium, desorption takes place at 550 K indicating deuterium detrapping from vacancies produced by the probe. Erents did not observe this effect as he used a probe dose equal to our damaging dose. The S value dropped after 1700 K to the bulk value, thus indicating that the positrons also observed no defects. An interesting result is that positrons implanted at a depth of 13 nm are not able to detect the clusters containing 40-60 vacancies. In this case the near surface V_{11-16} clusters have broken up and reached the surface before clustering could occur. A summary of the above

discussion is given in the table.

Table I
Results obtained for annealing of vacancy clusters and hydrogen interactions with vacancy clusters.

anneal temperature /K	cluster	deuterium desorption at /K	references
300	V_1 some V_{4-10} and V_{11-16}	550	[10-12]
600-750	V migrating /clustering		[**,21]
750-900	V_{4-10}		[**,16]
1150-1350	V_{11-16}	800	[**,16]
1500-1650	V_{40-60}	600	[**,16]
>1700 K	no defects	550*	[**,16]

[**] = this thesis and [21], * deuterium desorbing from vacancies produced by the probe.

In spite of the rather convincing results as described above, care has to be taken. The fact that the deuterium release is found at lower temperatures when the crystal is annealed to higher temperatures (and thus larger clusters have been formed) might point to an alternative explanation. Clusters containing 11-16 vacancies might become decorated with impurities (like nitrogen and oxygen). In this manner the deuterium dissociation energy can be lowered, because surface deuterium adsorption is prevented and deuterium is present as deuterium molecules. In this case the condition must be that oxygen stabilizes the V_{11-16} cluster. Impurity decoration of cavities at high temperatures in molybdenum has been reported by Nielsen et al. [22]. The influence of nitrogen (impurities) on the spectra is discussed below.

Nitrogen interactions with voids

When V_{11-16}'s are created and filled with nitrogen by 3 keV 1.5×10^{18} N_2^+ m^{-2} at a temperature of 443 K, probing with deuterium showed (not presented here) two interesting features. The desorption peak content of the peak at 800 K showed a decrease of a factor 20, whereas desorption took place in a peak at 800 K. Repeated probing experiments demonstrated some recovery of the peak content, although the peak shifted 50 K to lower temperatures.

When voids are created with the size of V_{40-60} and filled with nitrogen by bombardment at 3 keV and at an elevated temperature of 460 K, thermal deuterium desorption experiments showed similar behaviour. The deuterium peak content decreases with increasing nitrogen dose. The desorption peak remained at 600 K. At the two highest nitrogen doses the deuterium content increased again, while the desorption peak shifted to lower temperatures.

These experiments indicate that nitrogen atoms occupy sites at or in the vacancy clusters, preventing deuterium from trapping at the vacancy clusters. High nitrogen dose irradiation creates vacancies that can be decorated by the deuterium probe, see also figure 4.12. Deuterium desorption then shifts to lower temperatures, as deuterium vacancy dissociation takes place at 550 K (chapter 4). Therefore the possibility can be exluded that a high impurity concentration causes the temperature shift from 800 K to 600 K by decorating the vacancy clusters.

Deuterium interactions using diffusional rate theory

The diffusional rate calculations of section 5.7 also indicated that deuterium release is dominated by retrapping processes in the crystal. The annealing, to higher temperatures, of the crystal results in a lower void concentration, each void containing more vacancies. The modelled concentration of the adsorption sites at vacancy clusters varied from 2.6×10^{19} m^{-2} at an one minute anneal at 1060 K, to 5×10^{15} m^{-2} at an one minute anneal at 1526 K.

Helium bubbles

Helium bubbles are created by 3 keV $2x10^{19}$ He^+ m^{-2} and subsequent annealing. This helium dose creates HeV's, V's and some small helium filled vacancy clusters. After an anneal to 1600 K, HeV's dissociate [16] and with the other vacancies small helium bubbles will be formed.

Generally, from the results presented in section 5.6 it can be seen, using thermal deuterium desorption spectrometry, that at increasing anneal temperatures deuterium is released at lower temperatures. This result can be compared with the results at vacancy clusters. Also here we assume that the helium bubbles will increase in size, while the concentration of the helium bubbles decreases. TRIM calculations show that 3 keV He^+ irradiation creates vacancies at a depth of 8 nm. In the case of vacancy clustering experiments as discussed above, positrons implanted at a depth of 13 nm could not detect clusters containing 40-60 vacancies. For helium bubbles it is not clear at present which cluster sizes are favoured, if any. The deuterium peaks indicate that specific sites can be occupied.

The deuterium release in a peak at 700 K, found in the helium bubbles containing crystal heated to 1590 K, can possibly be ascribed to desorption of deuterium from internal adsorption sites. The desorption peak at 530 K resembles the peak resulting from deuterium dissociating from vacancies (fig 4.9). Possibly deuterium is forced by helium in the bubble to sit at the site which resembles the deuterium site in a vacancy. Desorption peaks at lower temperatures can be ascribed to a combination of effects. The desorption found at the highest dose in figure 5.8 can be ascribed to deuterium release from multiple deuterium filled helium bubbles. The peak at 400 K of the figures 5.9a and fig5.9b can be ascribed to deuterium release from helium bubbles at the sub-surface region.

5.9 Conclusions

The application of thermal desorption spectrometry and positron annihilation has proven to be successful in observing the annealing behaviour of single crystalline tungsten containing vacancy clusters of different sizes and helium bubbles. The deuterium probe was useful as a

nondestructive probe, taking advantage of the lower temperature desorption of deuterium compared to the dissociation of the vacancy clusters. The probe can therefore be used as a valuable complement (where appropriate) to the better established use of helium as a defect probe in metals [20].

Four anneal stages could be identified. In the first stage, vacancies were found to cluster at ≈650 K and form $V_{4\text{-}10}$ clusters. In the 2nd and 3rd stage, at ≈1050 K and ≈1400 K, the experimental results showed the growth of voids in two distinct steps. According to the AEM calculations by van Veen [16], the expected growth reactions were in the size ranges ($V_{4\text{-}10} \rightarrow V_{11\text{-}16}$) and ($V_{11\text{-}16} \rightarrow V_{40\text{-}60}$) respectively. A final stage leading to defect-free tungsten occurs at temperatures at approximately 1700 K.

Experiments with nitrogen filling of the vacancy clusters showed that the anneal stages must not be identified with impurity filling of the clusters. Deuterium desorption took place at the same temperature, whereas the deuterium peak content decreased with increasing nitrogen dose.

The diffusional rate calculations, simulating the deuterium desorption experiments, indicated that deuterium release is dominated by retrapping processes in the crystal. The annealing, to higher temperatures, of the crystal results in a lower void concentration. The modelled concentration of the adsorption sites at vacancy clusters varied from 2.6×10^{19} m^{-2} at an one minute anneal at 1060 K, to 5×10^{15} m^{-2} at an one minute anneal at 1526 K.

Deuterium desorption from helium bubbles showed a similar behaviour as the deuterium desorption from vacancy cluster growth. Increased annealing temperature of the helium bubble containing crystal displayed deuterium desorption at decreasing temperatures. The crystal must be heated several times to 2200 K in order to anneal the helium bubbles out.

References

[1] S.M. Myers, P.M. Richards, W.R. Wampler and F. Besenbacher, J. Nucl. Mater. **165** (1989) 9.

[2] G.R. Longhurst, J. Nucl. Mater. **212-215** (1994) 1015.

[3] R.A. Anderl, R.J. Pawelko, M.R. Hankis, G.R. Longhurst and R.A. Neiser, J. Nucl. Mater. **212-215** (1994) 1416.

[4] G. Gervasini and F. Reiter, J. Nucl. Mater. **212-215** (1994) 1379.

[5] A. van Veen, J. de Vries, D. Segers and G.J. Rozing, Positron Annihilation, Ed. P.C. Jain, R.M. Singru and K.P. Gopinathan (World Scientific Publ. Co. Singapore 1985) p.543.

[6] A. van Veen, H.A. Filius, J. de Vries, K.R. Bijkerk, G.J. Rozing and D. Segers, J. Nucl. Mater. **155-157** (1988) 1113.

[7] G.J. Rozing, A.W. Weber, P.E. Mijnarends, A. Van Veen, J. de Vries and H. Schut (proc. 9th ICPA, Hungary, 1991).

[8] S.K. Erents, Proc. 8th Symp. on Fusion Technology (SOFT, The Netherlands, 1974) 895.

[9] P.L. Andrew and M.A. Pick, J. Nucl. Mater. **212-215** (1994) 111.

[10] H. Eleveld, A.T. Dijksman and A. van Veen, Proc. 16th Symp. on Fusion Technology (SOFT, London, 1990).

[11] H. Eleveld and A. van Veen, J. Nucl. Mater. **191-194** (1992) 433.

[12] J.R. Fransens, M.S. Abd El Keriem and F. Pleiter, J. Phys. Cond. Mater **3** (1991) 9871.

[13] R. Sakamoto, T. Muroga and N. Yoshida, J. Nucl. Mater. **212-215** (1994) 1426.

[14] V.N. Chernikov, J.V. Lakhotkin, H. Ullmaier, H. Trinkaus, P. Jung and H.J. Bierfeld, J. Nucl. Mater. **212-215** (1994) 375.

[15] J.P. Biersack and L.G. Haggmark, J. Nucl. Instr. and Meth. 174 (1980) 257.

[16] A. van Veen, Mater. Sci. For. **15-18** (1987) 3.

[17] J.R. Heringa and A. van Veen, to be published.

[18] H. Jehn, H. Speck, E. Fromm and G. Hörz, in: Gase und Kohlenstoff in Metallen, eds. E. Fromm and E. Gebhardt (Springer Verlag, Berlin, 1976).

[19] I.A. Schwirtlich and H. Schultz, Phil. Mag. **A42** (1980) 601.

[20] A. van Veen, J. Trace Microprobe Techn. 8 (1990) 1.

[21] H. Eleveld and A. van Veen, J. Nucl. Mater. **212-215** (1994) 1421.
[22] B. Nielsen, A. van Veen, L.M. Caspers, H.A. Filius, H.E. Hansen and K. Petersen, Positron Annihilation, eds. P.G. Coleman, S.C. Shorma and L.M. Diana, Amsterdam , North Holland, p. 438.

Chapter 6.

Helium interaction with beryllium

6.1 Introduction

As already mentioned in chapter 1, Beryllium is used as a plasma facing material in JET because of its low Z value, high thermal conductivity, and hydrogen recycling coefficient [1,2]. In addition, reference was made to the use of beryllium as a neutron multiplier where potential problems arise from the associated helium production. Thus the understanding of both hydrogen and helium behaviour in beryllium will require research effort in the future.

Some work in these areas are already covered in the literature. The area on neutron and helium interaction with beryllium is reviewed by Gelles et al. [3]. Results on hydrogen are reviewed by Wilson [4] and recent publications on hydrogen transport and release can be found in [5-7]. Barnes and Redding published results of 40 MeV helium irradiation in 1959 [8]. They studied helium bubble growth during annealing. Macaulay-Newcombe et al. and Zakaria et al. [9,10] used 30 keV helium and measured helium release. Recently Jung used 28 MeV alpha particles to study diffusion and retention of helium implanted beryllium [11]. Wampler [12] showed deuterium release from helium bubbles.

Our interest has focused on the interaction of helium with beryllium. Thermal desorption spectrometry was performed on a 3 keV helium ion implanted sample, while neutron depth profiling, scanning electron microscopy and positron annihilation were used to analyze 30 keV helium ion irradiated samples. Preliminary thermal desorption results have been presented in [13]. Reference [14] has been the basis of this chapter.

6.2 Experimental

The beryllium foils, obtained from Highways International, had a quoted purity of 99.5%, BeO being the major impurity. The surface of the

sample used in the THDS experiments was not specially prepared, apart from preannealing to high temperatures. The NDP- and PA-samples were argon sputter cleaned. With 150 eV argon ion bombardment, a surface layer of 1 μm was removed. After sputtering, the samples were annealed to ~900 K. For 3 keV ^{4}He and 30 keV ^{3}He irradiations the mean implantation depths were calculated, using TRIM91 [15], to be 35 and 206 nm respectively with stragglings of 12 and 32 nm respectively.

Helium release after implantation was measured in a thermal helium desorption spectrometer (THDS) as described by Van Veen [16]. The background pressure was better than $1x10^{-7}$ Pa. The desorption spectrometer was equipped with an E x B mass filtered 0.1-6 keV ion beam. A calibrated quadrupole mass analyzer was used as a detector. In case of helium desorption, linear heating with a heating rate of 10 Ks^{-1} was applied. For NDP and PA, isochronal heating at a rate of 0.05 Ks^{-1} and 0.83 Ks^{-1} was applied, respectively. The isochronal heating rate of 0.05 Ks^{-1} was achieved by annealing with temperature steps: 1000 s at a specific temperature, followed by a 50 K temperature step; the heating rate of 0.83 Ks^{-1} was realized by 60 s annealing at a specific temperature and 50 K steps.

Neutron depth profiling (NDP) [17], see also chapter 2, was used to monitor the helium depth profile after annealing the sample. Three beryllium foils were irradiated with 30 keV ^{3}He ions at the following doses: $1x10^{19}$, $9.5x10^{19}$, and $7.7x10^{20}$ He m^{-2}. The samples were subsequently annealed together in a high vacuum chamber at a pressure of $2x10^{-4}$ Pa. After heating and subsequent cooling, the samples were transported through air to the NDP apparatus. After the last annealing step at 1075 K the samples were broken in two and studied with scanning electron microscopy (SEM).

Positron beam analysis was used to monitor the depth distribution of vacancy type defects. The variable energy positron (VEP) beam and technique are described in chapter 2, and in more detail by Schut and Van Veen [18,19]. The base pressure in the apparatus during the experiments was $1x10^{-6}$ Pa.

6.3 THDS results of helium irradiated beryllium

Helium was injected with an energy of 3 keV, at varying dose, to study dose related effects. The desorption spectra are shown in figure 6.1. At the lowest dose, helium is released mainly in a broad peak centered around 800 K (peak C). Increasing the dose led to movement of this peak towards 900 K, and the development of the D-peak at 1000 K and indications of an E-peak at 1150 K.

To relate the results of the THDS experiments to the NDP and PA results, knowledge about the helium concentrations in the implanted zones,

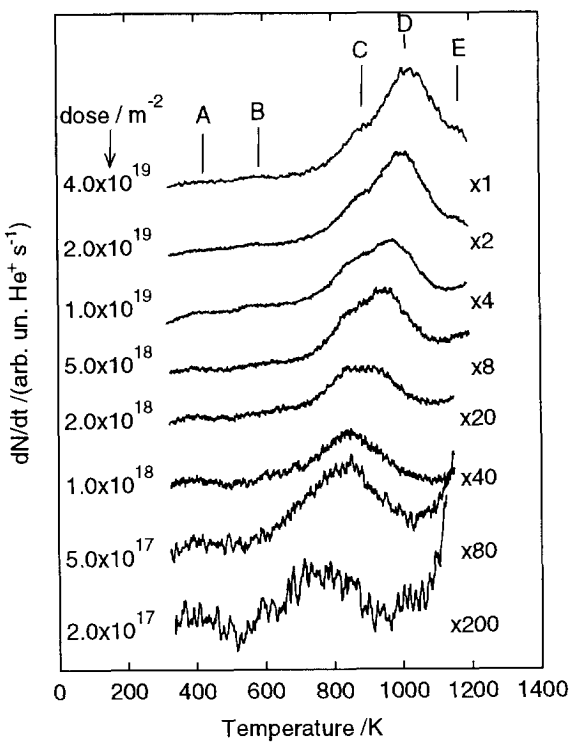

Fig. 6.1. Thermal helium desorption spectra on beryllium showing the effect of varying the 3 keV helium dose. A linear heating rate of 10 Ks^{-1} was applied. Note that the spectra have been scaled with the indicated factor.

before the thermal desorption, is required. At the lowest and highest helium dose, $2x10^{17}$ m^{-2} and $4x10^{19}$ m^{-2} respectively, the helium concentration in the implanted zone is calculated to be about $40x10^{-6}$ and $8x10^{-3}$ He/Be. For the calculation the helium (TRIM91) distribution is fitted by a Gaussian profile and 67 % of the helium is assumed to be in the zone within the standard deviation.

6.4 Neutron depth profiling results of post irradiation anneals

Neutron depth profiling was used to determine the remaining helium concentration during post irradiation annealing. The 30 keV implanted helium dose was $1x10^{19}$, $9.5x10^{19}$ and $7.7x10^{20}$ m^{-2}. The resulting helium concentrations in the implanted zone were calculated to range from $9x10^{-4}$ to $7x10^{-2}$ He/Be. The total amount of helium remaining in the foils versus anneal temperature is displayed in figure 6.2. Obviously, the amount of helium remained constant for the three samples up to 850 K. The sample

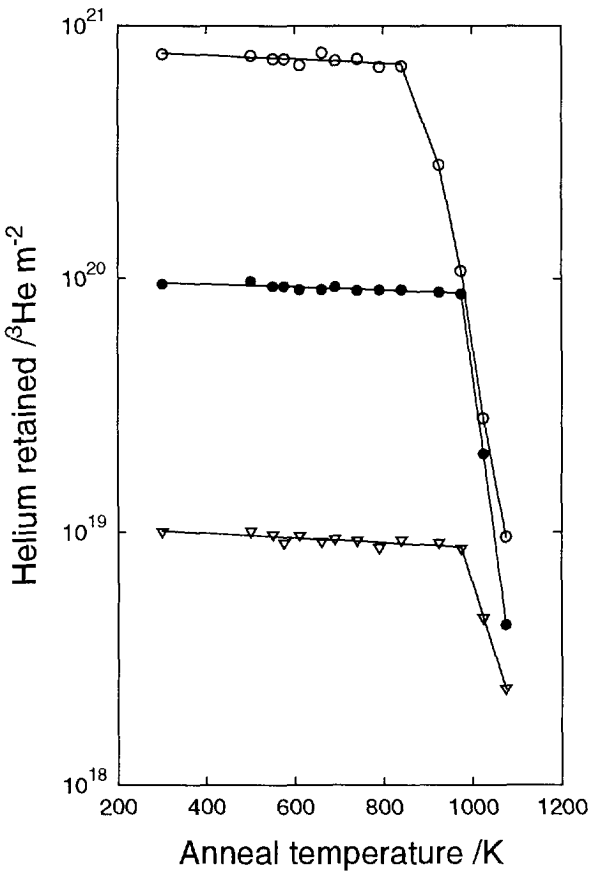

Fig. 6.2. Results from analyzed NDP experiments on samples implanted with 30 keV $^3He^+$ ions showing retained amount of helium versus anneal temperature (isochronal anneal, 0.05 Ks^{-1}). Open circles: sample with $7.7x10^{20}$ ^3He m^{-2}; filled circles: sample with $9.5x10^{19}$ ^3He m^{-2}; open triangles: sample with $1x10^{19}$ ^3He m^{-2}.

containing the highest dose released helium in the temperature interval from 850 K to 1075 K, whereas the other samples released helium at clearly higher temperatures, i.e. from 975 K to 1075 K.

In figure 6.3 the normalized helium concentration versus depth is shown for the case of the highest dose after specific annealing treatments. The concentrations were scaled to have the same maximum in order to depict the broadening of the helium depth profile. For the as-implanted result, the distribution agrees with the TRIM calculations quoted in section 2, when the broadening caused by convolution with the NDP response function is taken into account. A point relevant to the higher temperature anneals is that, as will be discussed in section 6.7, considerable swelling took place.

A simple approach to derive the deconvoluted helium concentration profiles was followed. Assuming Gaussian profiles for both the NDP

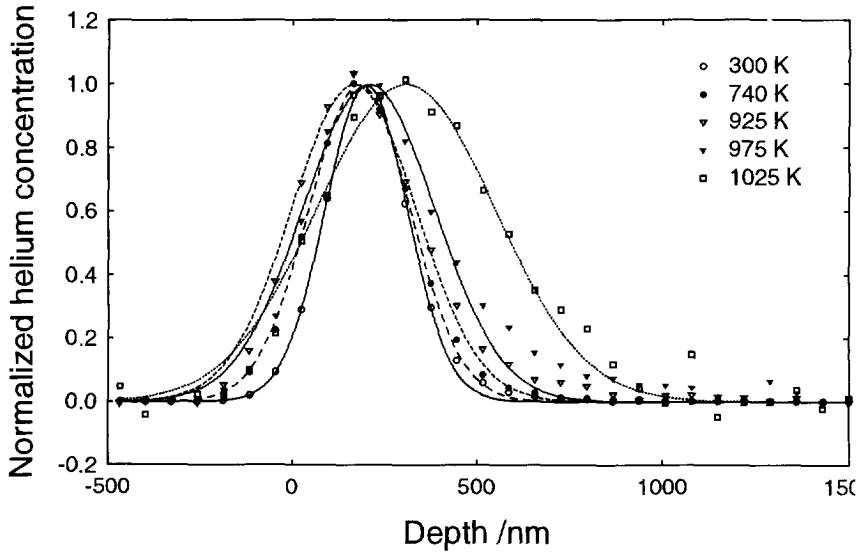

Fig.6.3. Results from NDP-measurements, showing the variation of normalised helium depth profiles with anneal temperature. The sample was implanted with 30 keV 7.7×10^{20} $^{3}He^{+}$ m^{-2}. The data points are fitted with a Gaussian. Open circles: 300 K; filled circles: 740 K; open triangles: 925 K; filled triangles: 975 K; open boxes: 1025 K.

response function and helium concentration profile, it can be shown that $FWHM^2_{measured} = FWHM^2_{NDP} + FWHM^2_{helium}$. Using this approach, FWHM values for the deconvoluted helium profile have been calculated and are plotted versus anneal temperature in figure 6.4. It can be observed that the helium distribution was broadened, changing from a FWHM value of 85 nm at 300 K to 630 nm at 1075 K. This large increase started at ~ 600 K and continued upward with suggestion of a plateau at 650 - 800 K subdividing the increase into two stages as marked in figure 6.4.

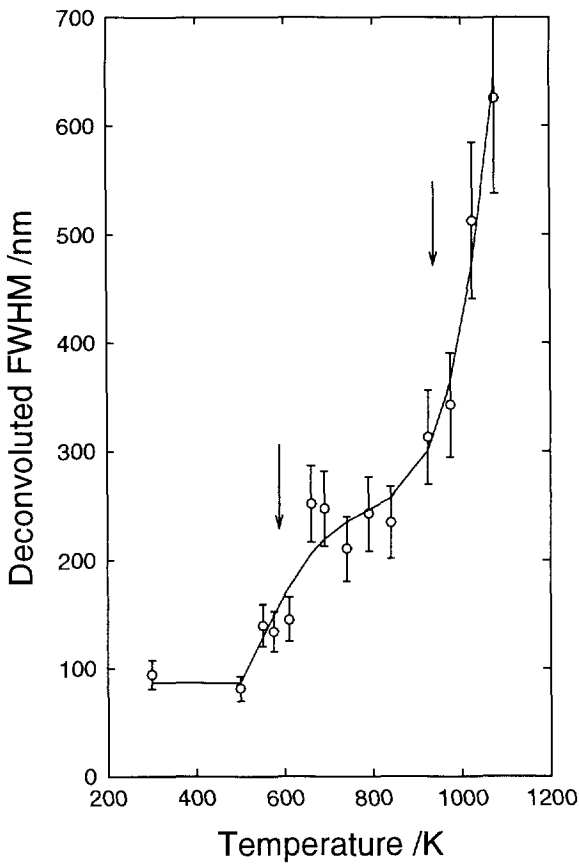

Fig.6.4. Results from NDP-measurements, showing the variation of deconvoluted full width half maxima with anneal temperature for the 30 keV 7.7×10^{20} $^3He^+$ m^{-2} irradiated sample. The arrows indicate the two apparent stages in the increase of the FWHM.

6.5 Scanning electron microscopy results

After the anneal to 1075 K the NDP samples were broken in order to examine the cross-section with SEM. An observation from the highest dose sample is given in figure 6.5 where it can be seen that the irradiated side contains cavities stretching from the surface to 4 μm below the surface. The size of the cavities in the highest dose sample are, as can be seen from figure 6.5, about 7x3x3 μm^3. Therefore extensive swelling took place, the implanted layer being swollen to 10 times its original thickness. At the

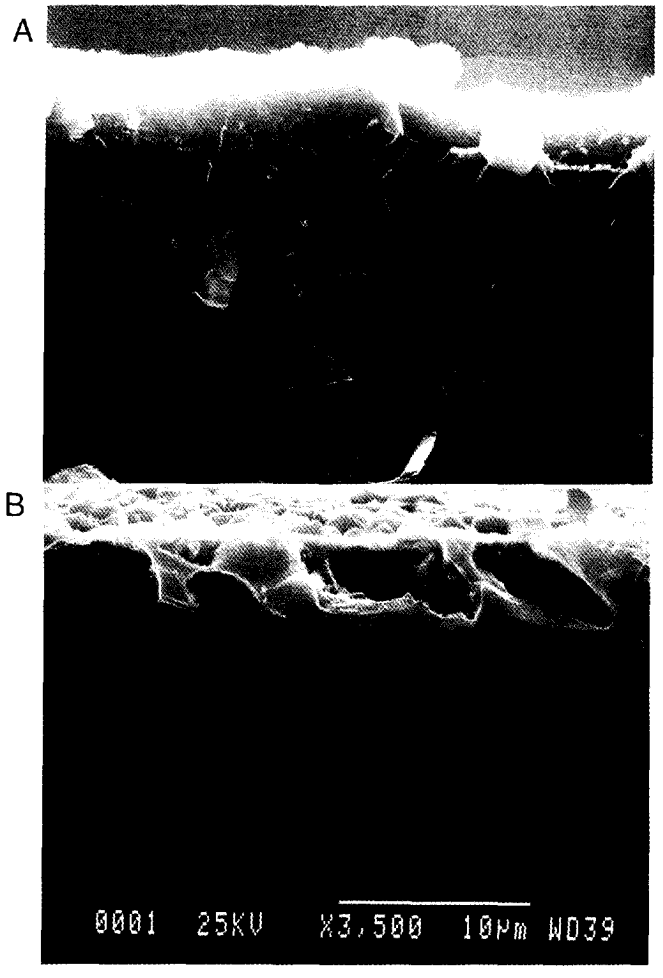

Fig. 6.5. Scanning electron micrographs, (a) beryllium sample unimplanted and (b) beryllium sample implanted with 30 keV 7.7×10^{20} $^3He^+$ m^{-2} and subsequently isochronally annealed to 1075 K.

lowest dose cavities were also observed, but with lower density and smaller sizes ($\approx$2x2x2 μm^3).

There is some evidence that the cavities are situated near grain boundaries. Top view micrographs, not presented here, showed the formation of an oxide layer, either as a result of transportation through air or annealing of the samples in relatively poor vacuum ($2x10^{-4}$ Pa). It is known that there is a considerable oxide growth in an oxygen atmosphere, but for temperatures up to 700 K the sticking coefficient drops to zero at an oxygen coverage of 7 monolayers [20].

6.6 Positron annihilation results of post-irradiation anneals

Measurements using variable energy positrons are shown in figure 6.6. The S-parameter versus anneal temperature is shown for a 30 keV ^{3}He with a dose of 4.6x10^{20} m^{-2} injected foil. The helium concentration in the implanted zone, before the annealings, was calculated to be about 0.04 He/Be. As mentioned in chapter 2, a high S value can be related to open volumes or cavities. The positron energies were selected to probe defects at average depths of 66 nm, 250 nm and 720 nm, corresponding with average

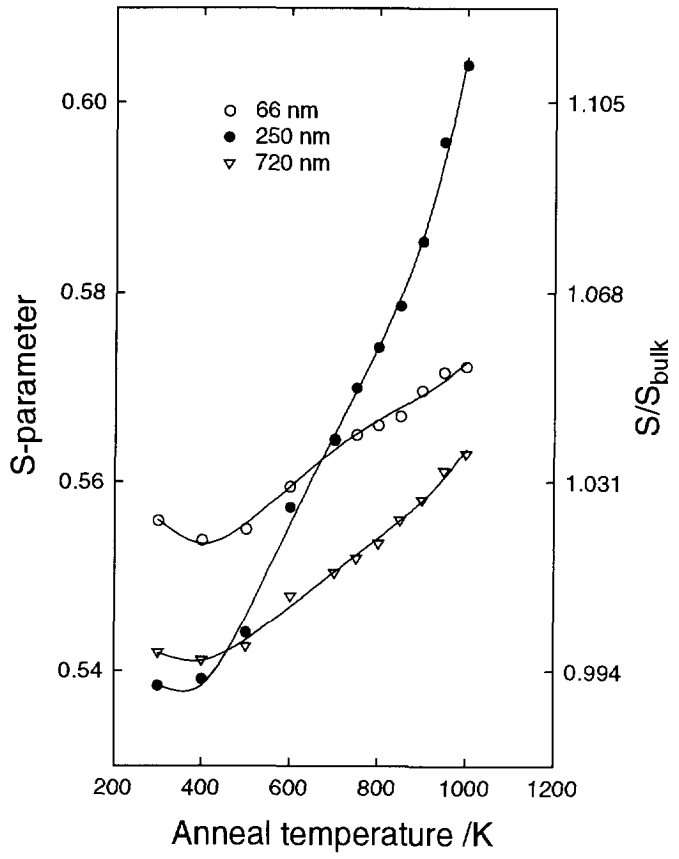

Fig. 6.6. Results from positron annihilation, S-parameter versus anneal temperature (isochronal anneal 0.8 K s^{-1}). The sample was implanted with 30 keV 4.6x10^{20} ^{3}He$^+$ m^{-2}. Positron probing of indicated depth regions. Open circles: 66 nm; filled circles: 250 nm; open triangles: 720 nm.

probe depths before, at, and beyond the maximum helium concentration. It should be remarked that the width of the positron depth profile is of the same magnitude as the average depth. From the figure it can be seen that the curve taken for the 66 nm probe starts with the highest S-value. Futhermore it is clear that the curve taken for the probe depth corresponding with the maximum helium concentration shows the largest increase of the S-value at T>500 K. VEPFIT [21] analysis of the data indicated the presence of cavities at a depth of 200 nm after the 950 K anneal. This is consistent with the SEM-results of section 3.3.

6.7 Discussion

When the results of the techniques are compared, we arrive at the following description of the helium behaviour. At temperatures from 600 K to 800 K, implanted helium becomes mobile. The THDS near-surface experiments (average implantation depth being 35 nm) showed helium release at these temperatures, and in case of the NDP and PA experiments (much larger average implantation depth: 206 nm), a broadening of the helium profile and an increase of the S-parameter respectively, are observed.

From the large width of the desorption peak C (THDS) at low helium doses it was concluded that helium was not released by a first order proces, but by a thermal vacancy assisted diffusion mechanism [13,22]. With the used two lowest helium doses in the THDS experiments, resulting in a helium concentration of about 40 to 100 appm only vacancy type defects are expected to be created, such as HeV's, V's and V_2's. The desorption spectra for low argon dose irradiated beryllium could be simulated with (self) diffusion data reported by Schumacher [23]. The used activation energy was E^{SD} = 1.66 eV and (self)diffusion coefficient of $D_0 = 1.8 \times 10^{-5}$ m^2s^{-1}, the implantation profile was taken from TRIM91 and fitted with a Gaussian. Jung [11] reported low helium diffusion coefficients, which he ascribes to trapping and dissociation processes at low temperatures (< 800 K). These results are in agreement with our data.

During implantation to high doses for the NDP and PA experiments, small helium vacancy clusters are formed. These helium vacancy clusters

can grow at temperatures > 600 K to helium bubbles possibly by the mechanism, which governs the helium release in the low dose THDS experiments : by thermal vacancy induced HeV migration. Another option is that, due to the high helium concentration ($9x10^{-4}$-$7x10^{-2}$ He/Be), only small helium bubbles are formed during implantation, so that growth is regulated by the helium and vacancy migration along the grain bounderies. The scanning electron micrographs show cavities at grain boundaries, which is also found in the literature [3,8], supporting this argument.

At 900 K the bubble growth become faster by gas pressure driven swelling. Helium is not released until the helium bubbles are extended to the surface. This results in the temperature of helium release eventually decreasing at higher doses. During release the PA data suggests that remaining bubbles are still growing with increasing temperature. This is consistent with the higher temperature stage in the NDP results, fig. 6.4. Furthermore, Jung [11] stated helium diffusion coefficients to be less than the self diffusion at temperatures > 1000 K; this is ascribed to clustering.

In table I the found helium behaviour in beryllium at various temperatures and concentrations are summarized.

Table I Behaviour of helium in beryllium at specific temperatures and He/Be concentrations at the mean implantation depth.

temperature /K	from low dose THDS experiments $4x10^{-5}$ - $1x10^{-4}$ He/Be	from NDP, PA SEM $9x10^{-4}$ - $7x10^{-2}$ He/Be
<600	no helium mobility	no helium mobility
600-800	vacancy assisted diffusion	* vacancy assisted diffusion * helium + vacancy mobility along grain bounderies
900-1000		gas pressure driven swelling, formation of cavities at grain boundaries

Obviously, the doses used by us were below the threshold dose for blistering as Verbeek and Eckstein [24] reported blisters at higher dose and lower energy. Terreault et al. [25] and Ross and Terrault [26] found blistering at 2-3x10^{21}m^{-2} at 20 keV ^{4}He-ion irradiation, with kbar He pressure in the blisters.

Comparing our 30 keV results with those obtained by Macaulay-Newcombe et al. [9], using about the same dose (1x10^{21} m^{-2}), energy (but for ^{4}He$^+$) and heating rate (in case of the NDP-results), we observe that in their experiments helium desorption took place at lower temperatures (from 600 K). This difference may be attributed to a different purity, or different grain sizes of the foils. Zakaria et al. [10] also found helium desorption at lower temperatures when the irradiation dose was increased from 1x10^{20} to 1x10^{21} He m^{-2}, the release took place at roughly the same temperatures as in figure 6.2. They ascribed the helium desorption as a helium-vacancy dissociation mechanism with an activation energy of 2.95(±0.25) eV (using Redhead's formula [27], which has already been abandoned by van Gorkum [28], as also the shapes of the spectra must be simulated/fitted). This cannot be true as the helium concentrations of the implanted series are, as in our experiments, in the percentage range. After heating, first coalescence of the HeV's will take place, before helium is desorbed. At low dose Ar and He implantation, we already found evidence of thermal vacancy assisted diffusion.

Barnes and Redding [8] reported swelling due to helium bubble growth at ~1000 K in extruded beryllium and at 1100 K in cast beryllium. The atomic helium concentration in the implanted region was reported to be 2000 appm, which corresponds with the lowest dose of the NDP-experiment. The difference in temperature in their experiments was ascribed to different grain sizes. The smaller the grain size, the lower the temperature at which the onset of swelling due to helium bubble growth was observed.

6.8 Conclusions

From the low helium and argon dose THDS near-surface experiments (3 keV ^{4}He$^+$ irradiated sample), it is concluded that helium is released (starting at 600 K) by a vacancy assisted diffusion mechanism. NDP

experiments with 30 keV $^3He^+$ irradiated samples showed a broadening of the helium distribution starting at 600 K. Thus small helium vacancy complexes become mobile at this temperature. Positron annihilation results also indicated an increase of open volume defects starting at the same temperature. Apart from vacancy assisted diffusion, an explanation can be found in the helium and vacancy mobility along the grain boundaries at temperatures around 600 K. Furthermore the release of helium from high dose implanted foil at lower temperatures (NDP-measurements) indicated bubble growth prior to release, driven by gas pressure driven swelling. Comparison with earlier results reported by Macaulay-Newcombe showed that in our experiments helium release took place at higher temperatures. Barnes and Redding reported helium induced swelling at temperatures which were in line with our SEM results. Our results can be compared with the general behaviour of helium in beryllium reported in the review of Gelles [3].

Literature

[1] The JET team: presented by P.R. Thomas, J. Nucl. Mater. **176-177** (1990) 3.

[2] R. Satori, G. Saibene, D.H.J. Goodall, E. Usselmann, P. Coad and D. Holland, J. Nucl. Mater. **176-177** (1990) 624.

[3] D.S. Gelles, G.A. Sernyaev, M. Dalle Donne and H. Kawamura, J. Nucl. Mater. **212-215** (1994) 29. and D.S. Gelles and H.L. Heinisch, J. Nucl. Mater. **191-194** (1992) 194.

[4] K.L. Wilson et al., J. Vac Sci. Technol. **A8** (1990) 1750.

[5] R.A. Causey and K.L. Wilson, J. Nucl. Mater.**212-215** (1994) 1436.

[6] E.A. Denisov, T.N. Kompaniets, A.A. Kurdyumov, S.N. Mazayev and Y.G. Prokofiev, J. Nucl. Mater. **212-215** (1994) 1448.

[7] D. Kéroack and B. Therrault, J. Nucl. Mater. **212-215** (1994) 1443.

[8] R.S. Barnes and G.B. Redding, J. Nucl. Energy **A10** (1959) 32.

[9] R.G. Macaulay-Newcombe, D.A. Thompson and W. Smeltzer, Fusion Eng. and Design **18** (1991) 419.

[10] Y.M. Zakaria, R.G. Macaulay-Newcombe and D.A. Thompson, preprint of article presented at Be-workshop Karlsruhe, Germany,

1993.
[11] P. Jung, J. Nucl. Mater. **202** (1993) 210.
[12] W.R. Wampler, J. Nucl. Mater. **196-198** (1992) 981.
[13] H. Eleveld, A. van Veen, M. Clement and M. de Moor, Plasma Devices and Operations **3** (1994) 65.
[14] H. Eleveld, A. van Veen, F. Labohm, M.W. de Moor, J. Nucl. Mater. **212-215** (1994), 971.
[15] J.P. Biersack and L.G. Haggmark, J. Nucl. Instr. and Meth. **174** (1980) 257.
[16] A. van Veen, A. Warnaar and L.M. Caspers, Vacuum **30** (1980) 109.
[17] R.G. Downing, J.T. Maki and R.F. Fleming, J. of Rad. and Nucl. Chem. **112** (1987) 33.
[18] H. Schut, PhD. Thesis, Delft, The Netherlands (1990).
[19] A. van Veen, J. of Trace and Microprobe Techniques **8** (1990) 1.
[20] D.E. Fowler and J.M. Blakely, Surface Science **148** (1984) 265.
[21] A. van Veen, H. Schut, J. de Vries, R.A. Hakvoort and M.R. IJpma, AIP Conf. Proc. **218** (AIP, New York, 1990), 171.
[22] A. van Veen, Mater. Sci. For. **15-18** (1987) 3.
[23] D. Schumacher, in Proc. of the Int. Conf., Jülich, Germany, eds. A. Seeger, D. Schumacher, W.Schilling and J. Diehl (1968).
[24] H. Verbeek and W. Eckstein, (Proc. of the Int. Conf. on Appl. of ion beams to metals, 1974 Plenum Press, New York).
[25] B. Terreault, G. Ross, R.G. St.-Jacques and G. Veilleux, J. Appl. Phys. **51** (1980) 1491.
[26] G. Ross and B. Terreault, J. of Nucl. Mater. **89** (1980) 383.
[27] P.A. Readhead, Vacuum **12** (1962) 203.
[28] A.A. van Gorkum, PhD. Thesis, Delft, The Netherlands (1981).

Chapter 7.

Helium interaction with V and Nb

7.1 Introduction

Vanadium alloys are considered as candidates for use as structural materials in fusion reactors. Some of the advantages over other alloys are the low degree of activation, good irradiation damage resistance and low thermal stress factor [1]. Vanadium is a basic constituent in a class of so called low activation materials (LAM). Studies on the mechanical properties of irradiated alloys have shown that impurities and precipitates may play an important role in the observed behaviour [2,3]. More details about V-alloys are given in chapter 1.

For vanadium little is known about the early stages of nucleation of helium vacancy clusters and helium bubbles. Mansur et al. [4] realized that the formation and growth of microstructures, such as cavities, depends on helium interaction with impurities in V-alloys. In addition, basic information on the diffusion of helium and vacancies must also be important. In V (and in Nb, another group 5 element) diffusion results for helium are reported by Lewis [5] and Vassen et al. [6] and Jung [7] and show helium migration at low temperatures. However, calculated, measured or derived vacancy migration energies vary widely from 0.5 to 1.3 eV [8-12].

One outcome of the present work was to give clear evidence for vacancy migration at low temperatures but the main aim was to obtain some fundamental insight into the first stages of the formation of helium bubbles in vanadium. In order to understand the results concerning vanadium we also performed some helium desorption experiments on niobium. The results are compared with earlier helium desorption work on the group 6 elements Mo and W [13,14].

7.2 Energy considerations of the He-O-V(/Nb) system

In order to get some insight into the reactions described in this chapter, we will start with an energy consideration regarding the dissociation/association reaction of the OV-defect:

$$OV \rightleftharpoons O + V$$

The binding energy of the vacancy to an OV-defect can be written in terms of dissociation and migration energies :

$$E_{OV}^{B,V} = E_{OV}^{D,V} - E_V^M \tag{7.1}$$

The formation energy is the energy that is needed to place a specific particle in a structure. The binding energy of the oxygen atom to an OV-defect, in terms of formation energies is thus given by :

$$E_{OV}^{B,O} = E_O^F + E_V^F - E_{OV}^{F,V} = E_{OV}^{B,V} \tag{7.2}$$

Compared to (7.1) the dissociation energy of a oxygen-vacancy complex can be written as:

$$E_{OV}^{D,O} = E_{OV}^{B,O} + \min(E_O^M, E_V^M) = E_{OV}^{B,V} + \min(E_O^M, E_V^M) \tag{7.3}$$

The vacancy migration energy has been reported to be E_V^M = 0.5-1.3 eV [8-12], while the oxygen migration energy is given by E_O^M = 1.3 eV [15]. So the dissociation of a oxygen-vacancy complex is probably dominated by the lower vacancy migration energy. In the next sections this is also studied.
Energy considerations of the association/dissociation of a HeOV complex are also interesting with respect to the possible reactions during heating of the crystal. The difference in binding of oxygen and helium to the HeOV complex can be written as:

$$E^{B,O}_{HeOV} - E^{B,He}_{HeOV} = (E^{F}_{HeV} + E^{F}_{O} - E^{F}_{HeOV}) - (E^{F}_{OV} + E^{F}_{He} - E^{F}_{HeOV}) =$$

$$= E^{F}_{HeV} - E^{F}_{He} - E^{F}_{OV} + E^{F}_{O} = E^{B,O}_{OV} - E^{B,He}_{HeV} = E^{B,V}_{OV} - E^{B,He}_{HeV} \qquad (7.4)$$

The differences of the dissociation energies of O and He from HeOV can be written as differences of the dissociation energies of vacancies and He from OV and He respectively corrected by the difference of migration energies of oxygen and vacancies:

$$E^{D,O}_{HeOV} - E^{D,He}_{HeOV} = (E^{B,O}_{HeOV} - E^{B,He}_{HeOV}) + E^{O}_{M} - E^{M}_{He} = E^{D,V}_{OV} - E^{D,He}_{HeV} + E^{M}_{O} - E^{M}_{V} \qquad (7.5)$$

In this way it is therefore possible to analyse the dissociation of the HeOV-complex interms of the dissociation of the smaller complexes OV and HeV and migration energies.

7.3 Vanadium

7.3.1 Dose variation of 1 keV helium

In fig.7.1 typical helium desorption spectra are shown for a wide range of helium doses. At low doses (less then $1x10^{16}$ $He^{+}m^{-2}$) the desorption is centred at 550 K. At least two peaks, denoted peak 1 and 2, contribute to the desorption spectrum. When the dose is increased to $2x10^{16}He^{+}m^{-2}$ a desorption peak denoted as peak 3 at 650 K is also found. At doses higher than $2x10^{16}He^{+}m^{-2}$ and up to $8x10^{16}$ $He^{+}m^{-2}$ 4 additional peaks denoted 4,5,6 and 7 are observed at temperatures ranging from 700 K to 950 K. At still higher doses another 4 desorption peaks (13,14) are observed at temperatures ranging from 950 K to 1200 K. The peak population versus dose is displayed in figure 7.2.

Compared with BCC-metals like molybdenum and tungsten (fig.7.3), vanadium shows an anomalous behaviour: an H-peak (HeV -> He + V) at 0.4 T_m as observed for Mo and W, is not found in the case of vanadium and the E,F,G- peaks (He_nV -> $He_{n-1}V$ + He with n=5-9,4-3 and 2

respectively) seem to be absent. Furthermore the wide variety of peaks occurring at doses higher than $1x10^{17}$ $He^{+}m^{-2}$ is not observed for Mo and W [13,14].

It is worth mentioning that vacancies in vanadium are calculated [12-14] to be mobile at the irradiation temperatures in these experiments. Furthermore, the coming sections 7.3.6 and 7.3.7 will point out that vacancies are mobile at 300 K. So, as at this temperature both helium and vacancies are mobile in an otherwise perfect crystal, very low helium trapping is expected. The trapped fraction of 12 % found at the lowest dose in figure 7.2. can be explained by assuming that impurities immobilise part

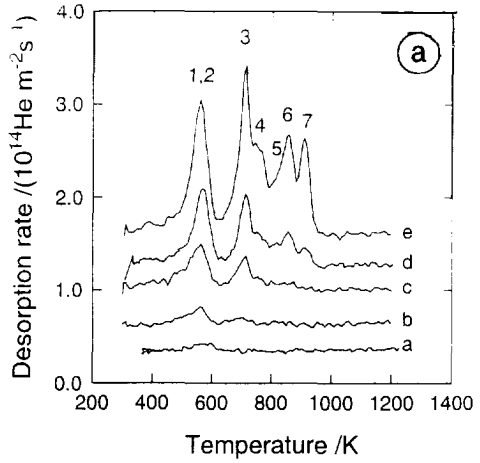

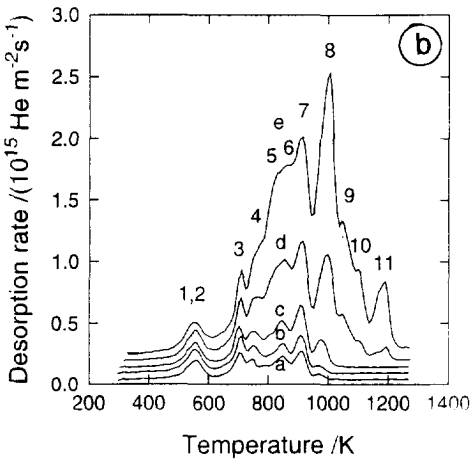

Fig.7.1a. Helium desorption spectra from 1 keV He^{+} irradiated vanadium. Doses used: a) $5x10^{15}m^{-2}$, b) $1x10^{16}m^{-2}$, c) $2x10^{16}m^{-2}$, d) $4x10^{16}m^{-2}$, e) $8x10^{16}m^{-2}$.

Fig.7.1b. The same as in fig. 7.1a. Note the difference in scaling. Doses used: a) $1.2x10^{17}m^{-2}$, b) $1.6x10^{17}m^{-2}$, c) $2.4x10^{17}m^{-2}$, d) $5.3x10^{17}m^{-2}$, e) $1x10^{18}m^{-2}$.

of the monovacancies. Therefore we ascribe peak 1+2 to HeXV defects with X being an impurity (C, O, N). Desorption peaks corresponding with larger defectcomplexes appear at higher doses. The peak populations of these peaks grow much faster than linear with dose than peak 1+2, indicating the formation of complexes consisting of more than one vacancy and one helium atom.

Atomistic calculations (with the RELAX-code [16]) using the atom embedded method according to Finnis and Sinclair, modified by Rebonato [17], were performed in this thesis to estimate helium vacancy dissociation energies. The calculated helium vacancy dissociation energy (HeV -> He + V) amounts to 3.42 eV. Fitting of the desorption peak at 550 K assuming a

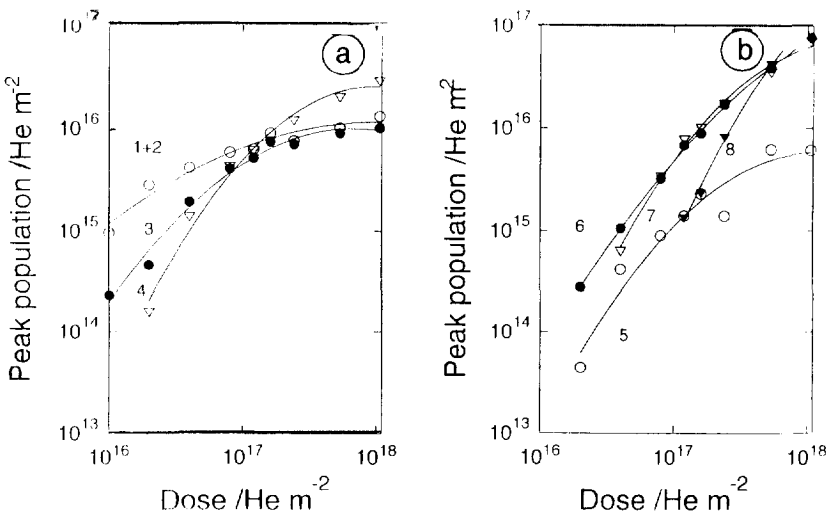

Fig.7.2a Helium captured in defects in vanadium at the specified dose; the helium ion energy was 1 keV. Peaks 1+2, 3 and 4.
Fig.7.2b The same as in fig. 2a. Peaks 5,6,7 and 8.

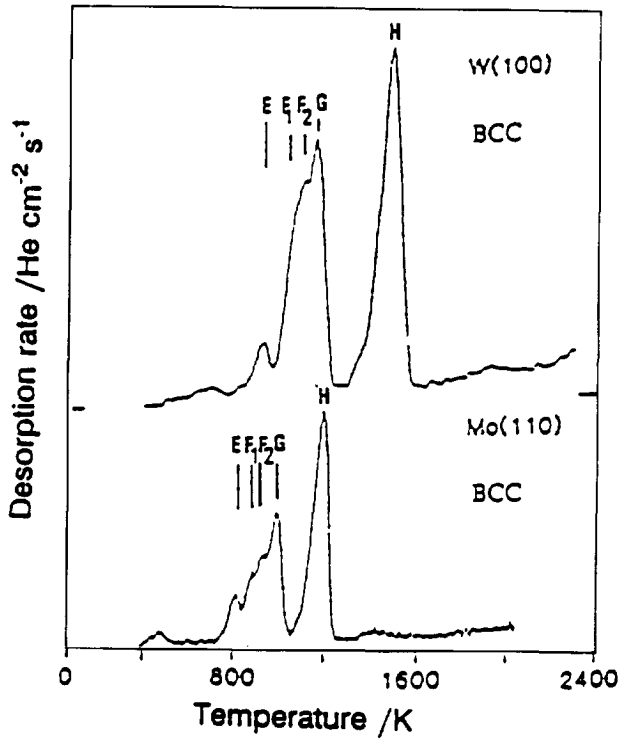

Fig.7.3. Characteristic helium desorption spectra obtained for tungsten: W(100) and molybdenum: Mo(110). The doses used were 10^{16} m^{-2}. The spectra were previously published in [13,14].

first order desorption process yields a much lower desorption energy of approximately 1.5 eV. The absence of an H-peak at 0.4 T_m as mentioned above can be explained by impurity capture during the irradiation or the desorption; (N and O being mobile in vanadium at ~500 K [15]). For example an interstitial oxygen impurity becoming mobile at 450 K can be trapped by HeV's: HeV + O -> HeOV thus causing a lowering of the helium desorption temperature.

7.3.2 Helium energy variation

In figure 7.4 helium desorption spectra are shown which have been obtained after irradiation with varying helium ion energies at a fixed dose of $2x10^{17}$ He m^{-2}. At low energy the helium desorbs from the crystal at low

temperatures and the amount desorbed is small. At increasing energies, up to 500 eV, it is observed that the helium trapping in the defect giving rise to peak 1+2 is increasing. At energies above 1 keV helium is captured in defects causing desorption at temperatures up to 900 K (defects 5-7), while at increasing energy the helium capture in the defect corresponding with peak 1+2 is decreasing in favour of defects corresponding with peaks 3-7.

The above observations can be explained as follows: surface trapping occurs at helium ion energies < 200 eV. Vacancies are created at helium ion energies ≥ 200 eV; with the displacement energy being 25 eV, a helium ion with an energy of 200 eV will produce about one vacancy and one self interstitial, assuming $0.27E_0$ as the maximum energy

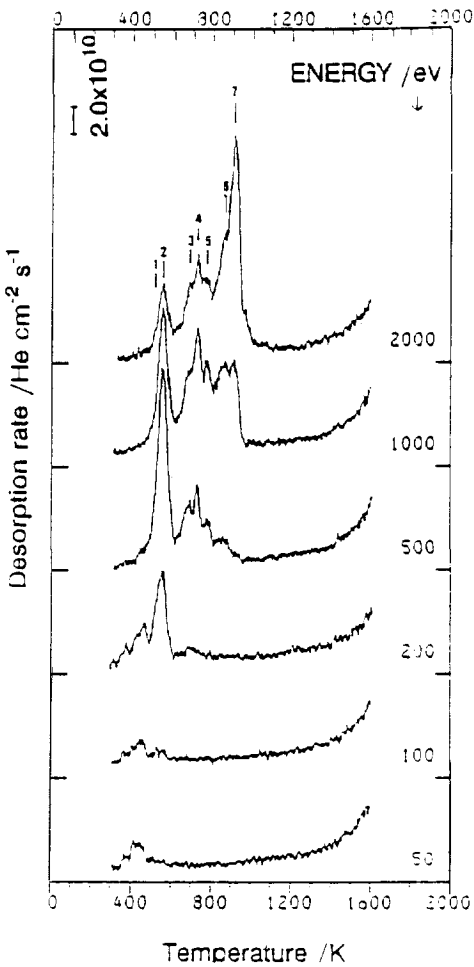

Fig.7.4. Helium desorption spectra of experiments on vanadium in which the helium ion energy was varied. The ion energies are displayed in the figure. The dose was kept constant at $2x10^{17} m^{-2}$.

transferred by helium to vanadium, with E_0 the primary helium energy. At higher helium ion energies an increasing amount of vacancies is produced, promoting the formation of vacancy clusters, thereby leading to helium desorption at higher temperatures.

7.3.3 Helium filling of vacancies produced by 1 keV He^+

Pre-irradiation using 1 keV $2x10^{16}$ He^+ m^{-2} and subsequent filling with 100 eV $1x10^{17}$ He^+m^{-2} resulted in a strong increase in desorption at 550 K, compared with an experiment without pre-irradiation. From fig.

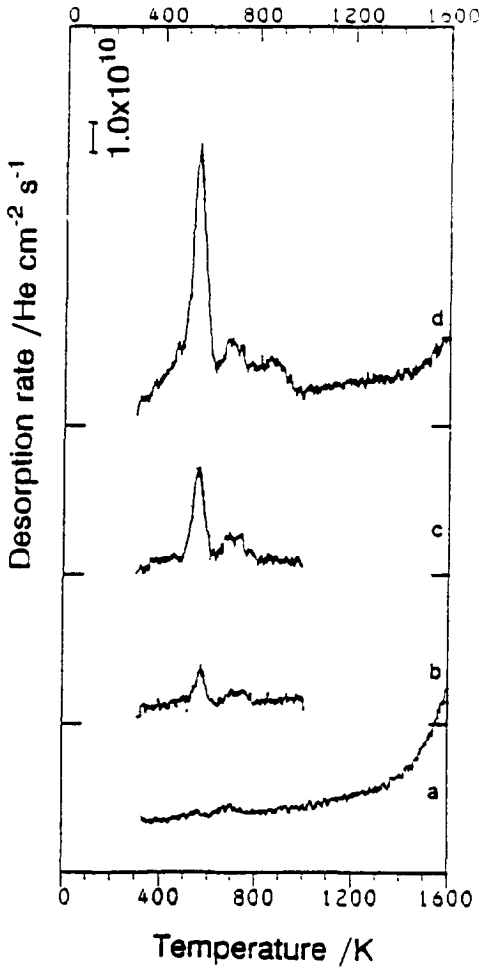

Fig.7.5. Helium desorption spectra (for vanadium) obtained by: a)$1x10^{17}$ He^+m^{-2} 100 eV, b)$2x10^{16}$ He^+m^{-2} 1 keV, c) as in b) + $1x10^{17}He^+m^{-2}$ 100 eV, d) as in b) + $5x10^{17}$ He^+m^{-2} 100 eV.

7.5a it can be seen that irradiation with 100 eV helium ions hardly causes trapping in the crystal; see also fig. 7.4 where the helium ion energy has been varied. The 1 keV helium ion beam creates vacancies and vacancy complexes (XV and HeXV), as explained above. Then subsequent filling with 100 eV helium as shown in fig. 7.5c causes a strong increase of the helium population of peak 1+2. When the helium dose of 100 eV helium is increased to $5x10^{17}$ He^+m^{-2} defects are created giving rise to desorption at temperatures up to 950 K. From these experiments and the linear behaviour during filling of peak 1+2 it can be concluded that vacancies produced by 1 keV He^+ irradiation were still present at room temperature. These vacancies must have been trapped at impurities in the crystal, since the vacancies are mobile at room temperature as discussed before. In a following sub-section the capture of vacancies by impurities is further explored. The observed occurrence of high temperature peaks is ascribed to helium induced trapmutation of the vacancies.

7.3.4 Annihilation of vacancy type defects by self-interstitial implantation

In the following experiment the vanadium crystal was irradiated by 1 keV $2x10^{16}$ He^+ m^{-2} in order to produce vacancy type defects (XV and HeXV) as described in previous sub-sections. Argon injection of 50 eV resulted in a decrease of retained helium in the defect giving rise to peak 1,2. The observed reaction can be described as the conversion reaction: HeXV + I -> He + X. At a dose of $1.2x10^{19}$ Ar^+ m^{-2} nearly no helium was detected during an anneal of the vanadium sample, indicating that all vacancies had recombined with self interstitial atoms.

7.3.5 Impurity delayed vacancy migration

Figure 7.6 shows results of an annealing experiment where 1 keV $2x10^{16}$ He^+m^{-2} (at room temperature) is used to produce vacancies, followed by an anneal (10 Ks^{-1}) to the indicated temperature. Finally the remaining vacancies were decorated by helium. The amount detrapped in the 550 K desorption peak is displayed. The results indicate a dissociation

reaction of XV : XV → X+V at temperatures from 350 to 550 K. The vacancy migration resulting from this reaction has clearly been delayed by trapping at impurities. Such trapping and later vacancy release can probably explain the recovery in this region being mistakenly attributed to vacancy migration by Janot et al. [8].

The effect might be the origin of the anomalous behaviour of vanadium. It implies that helium is trapped in XV's rather than in V's and therefore might dissociate via the reaction HeXV → He + XV. Apparently the alternative dissociation reaction HeXV → X + HeV → X + He + V does not occur, else helium release should have been found at higher temperatures.

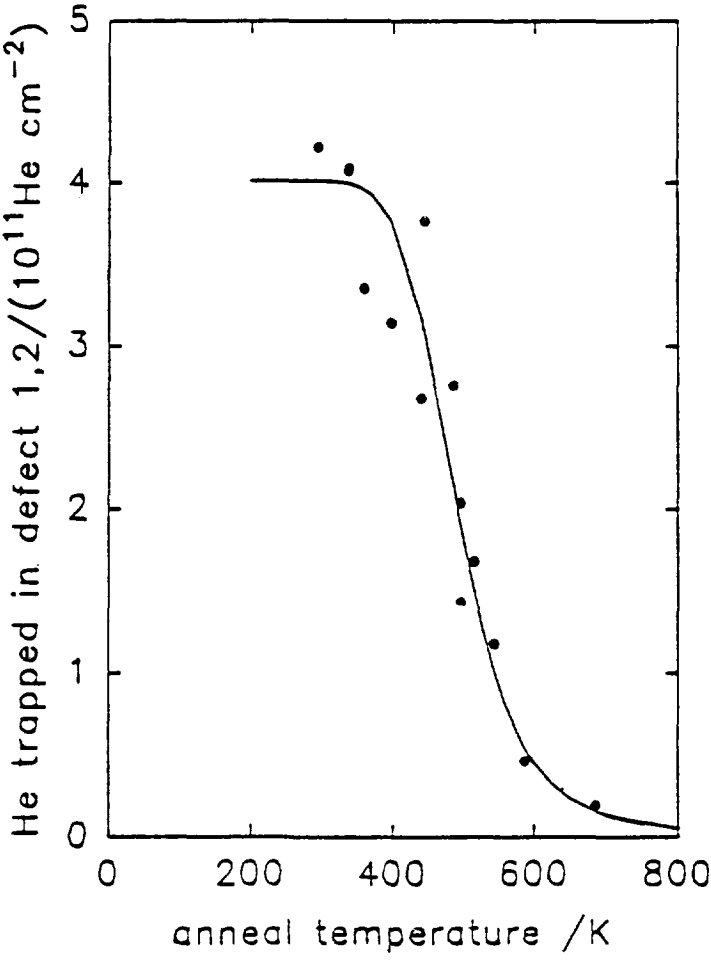

Fig.7.6. Amount trapped in the defect corresponding with peak 1+2 (HeXV) in vanadium as a function of anneal temperature. The experiment included: preirradiation: 1 keV $2x10^{16}$ He^+m^{-2}, anneal to the specified temperature, filling of the remaining defects with $1x10^{17}He^+m^{-2}$.

Vassen et. al. [6] (using 28 MeV α particle irradiation) reported helium diffusion by a dissociative mechanism, giving a dissociation enthalpy of 1.4 (±0.3) eV. It is possible that diffusion reported by these authors could be ascribed to detrapping and retrapping in the reaction HeVX ⇄ He + XV. The quoted activation energy found is close to the energy found in this work for HeXV dissociation.

7.3.6 Results of irradiation at temperatures ranging from 115 to 700 K

In figure 7.7a helium desorption spectra are shown for 1 keV $1x10^{18}$

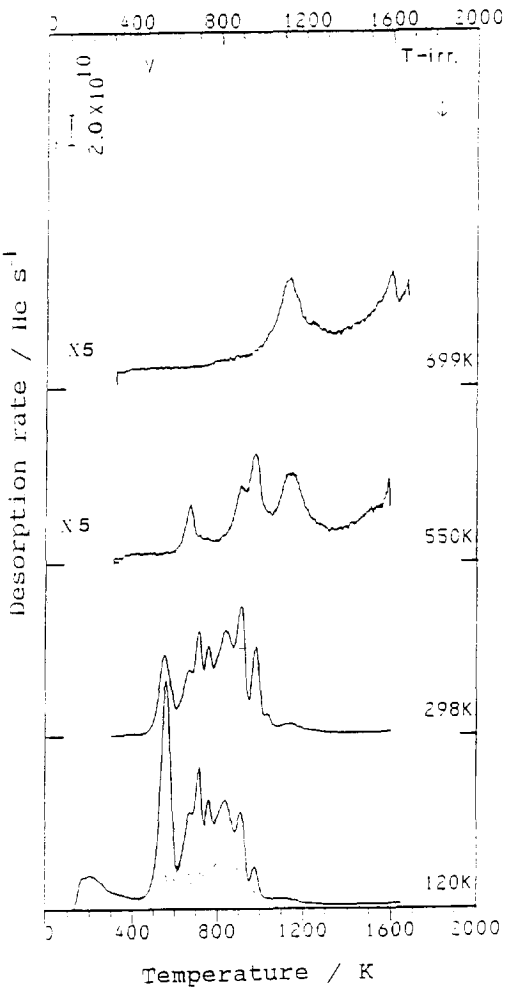

Fig.7.7a. Helium desorption spectra obtained for vanadium at the specified irradiation temperatures. The irradiation dose was 1 keV $1x10^{18}He^{+}m^{-2}$.

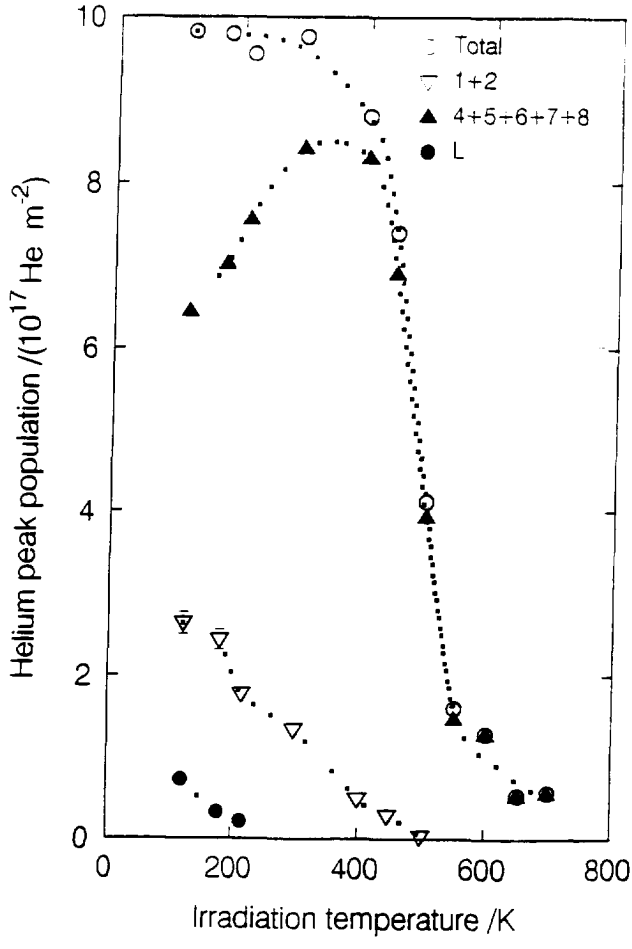

Fig.7.7b. Peak populations at various irradiation temperautures. Helium is injected with 1 keV energy and a dose of $1x10^{18}$ m^{-2}. a) total amount of trapped helium, b) helium trapped at defect 1,2, c) helium trapped at interstitials/surface (L) defects, d) helium trapped by defects corresponding with peaks 4,5,6,7 and 8.

He^+ m^{-2} irradiation of vanadium at varying temperatures. Figure 7.7b gives

an overview of the trapped helium amount. The helium concentration in the top layers of the crystal was 1000 ppm. First it can be seen that the total amount trapped in the crystal remains constant for irradiation temperatures ranging from 120 K to 300 K. A desorption experiment after injecting helium at a low temperature of 120 K shows helium desorption in the peak denoted L at temperatures ranging from 125 K to 300 K, possibly due to trapping of helium by interstitial impurity atoms or surface trapping.

The spectrum illustrates the dominance of the defect resulting in desorption in peaks 1,2 at 550 K. The peak population of peaks 1,2 decreases when the crystal temperature is increased to 215 K. From this we may conclude that vacancies become mobile above 200 K. The temperature region between 100 K and 300 K is the subject of the next section, in order to estimate the diffusion coefficient of a vacancy in vanadium. The total amount trapped is still the same because the amount captured in defects giving rise to peaks 6,7,8 and 9 are increasing. This may be explained by vacancy clustering during irradiation or by helium induced trapmutation [18]. At an irradiation temperature of 550 K a drastically lower trapping percentage is observed. So the HeXV-defect dissociating at this temperature is an important nucleation site for larger defect complexes or helium bubbles. At irradiation temperatures up to 700 K still some helium remains in the crystal (5% of the initial trapped amount), possibly due to small helium bubbles formed upon annealing, i.e. clustering of small defects.

7.3.7 Vacancy mobility in vanadium

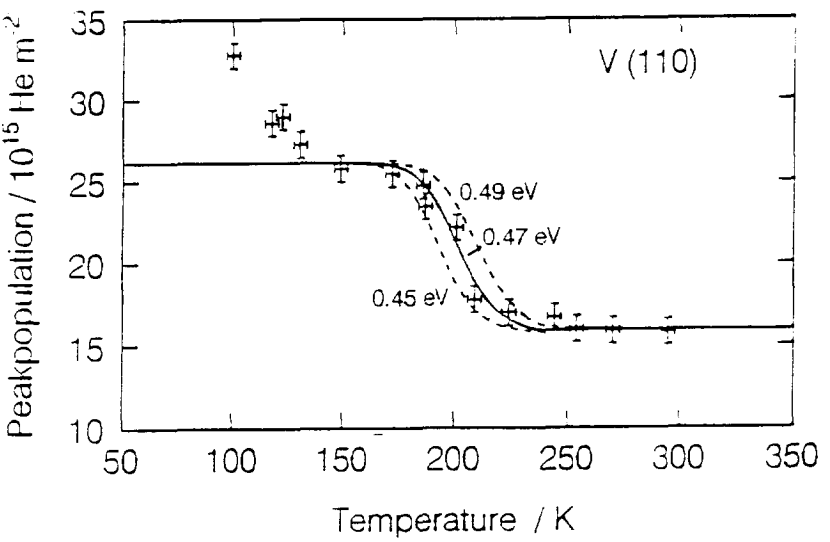

Fig.7.8. Peak population of the peaks 1,2 ascribed to HeV and HeO dissociation in vanadium versus the temperature during irradiation with 1 keV He^+ ions. The solid and the dotted curves correspond with results of model calculations on migration of irradiation induced vacancies while a concentration of 20 appm O is present. The dose rate amounts to $5x10^{14}$ He m^{-2} s^{-1}.

In the previous section the irradiation temperature was varied with large steps in order to obtain a insight into damage build up at various temperatures. Also the decrease of the helium desorption in the 1,2 peak and the increase of the desorption in the 4-8 at increasing irradiation temperatures suggested that vacancies become mobile at around 200 K. In this section we concentrate on the region around 200 K. The peak population of the 1,2 peak versus the irradiation temperature is shown in figure 7.8. A partial reduction of the peak population is observed at ~ 200 K, which is ascribed to loss of vacancies because they become mobile at this temperature. The stage at 100 K is related with mobility of interstitial helium, but will not be discussed here. Some 60% of the vacancies appear to survive the increase in irradiation temperature at 200 K, and therefore must be immobilized by impurity trapping (oxygen). Modelling of the process with depth-dependent rate and diffusion theory, as described in chapter 3, yields a theoretical curve for the annealing stage with a diffusion coefficient of $D_V = 1\times10^{-7} \exp\{-0.47(\pm0.02)[eV]/kT\}\ m^2s^{-1}$, where k is Boltzmann's constant. The concentration of impurities (oxygen) that was assumed to explain the vacancy retention was ~ 20 appm. The formed defects dissociate at 450 K as discussed in section 7.3.5.

7.3.8 Ne, Ar and Kr irradiation of the vanadium crystal

Thermal desorption spectrometry using the inert gases neon, argon and krypton was applied in order to compare the results with the helium desorption in the preceding sections. When impurity atoms are involved in the relatively low temperature helium desorption, it can be expected that other inert gases are also released at relatively low temperatures.

Desorption results of the vanadium crystal irradiated by neon, argon and krypton ions are shown in fig. 7.9. The ions were injected with an energy of 2 keV. An interesting feature is the desorption of all these inert gas ions taking place in peaks at ~ 1000 K. One of the peaks of the argon desorption spectrum could be fitted with a first order desorption process yielding an energy of 3.17 eV and a attempt frequency of $1\times10^{15}\ s^{-1}$. Using RELAX (based on potentials of [17]) we found dissociation energies varying from 5.74 eV (Ne) to 8.14 eV (Kr). These values are too large to

hold Ne, Ar or Kr dissociation from a vacancy responsible for the observed release. Probably, as with helium, impurities are involved either by capturing the migrating vacancy or by jumping into the NeV ,ArV or KrV during the anneal. Further experiments are necessary to clarify the desorption mechanisms.

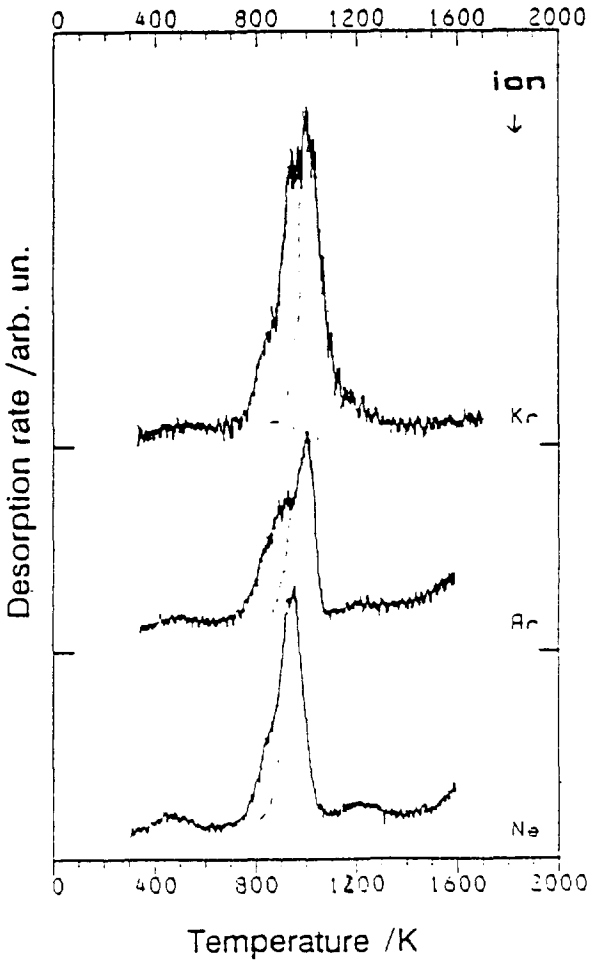

Fig. 7.9. Neon, argon and krypton desorption spectra for vanadium; ion energy 2 keV and dose $2x10^{16}$ ions m^{-2}.

7.4 Niobium

7.4.1 Helium in monovacancies

The results of the experiments with 1 keV helium ions injected in niobium are shown in figure 7.10. From the figure it is clear that at low doses helium desorption takes place at around 740 K, denoted as the H-peak. At increasing dose, helium is also released at lower temperatures, denoted as the G,F, and E-peaks.

The result of the experiments on niobium can be compared with the

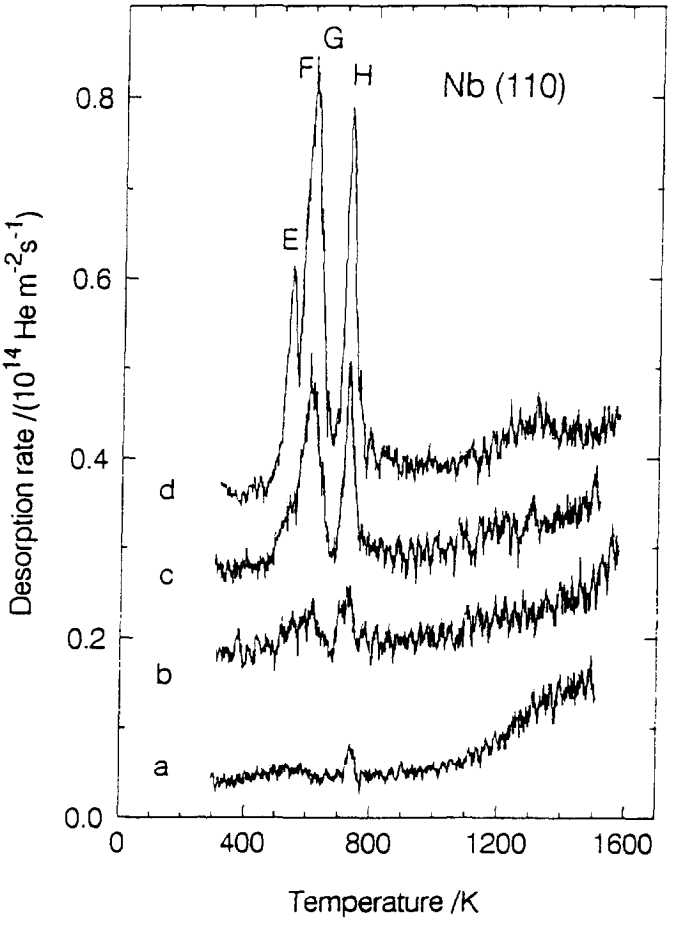

Fig. 7.10. Helium desorption spectra obtained for 1 keV He^+ irradiated niobium. The doses used are a) $6x10^{15}$ m^{-2}, b) $1x10^{16}$ m^{-2}, c) $5x10^{16}$ m^{-2}, d) $1x10^{17}$ m^{-2}.

helium desorption experiments on molybdenum and tungsten [13,14], see fig. 7.3. The desorption from the helium-vacancy type defect is found at the same relative temperature $T/T_m \simeq 0.25$ as in V, in contrast with $T/T_m \simeq 0.4$ for the case of the other BCC metals Mo and W [13,14]. Thus we expect also here that impurity vacancy interactions play a dominant role.

7.4.2 Oxygen migration and OV dissociation in niobium

For niobium the results of an annealing experiment are shown in figure 7.11. After irradiation with a low dose of 3 keV He ions, annealing and helium probing (200 eV) was performed. Peak populations ascribed to impurity-decorated vacancies show two recovery stages at 500 K and 750 K.

The first annealing stage, at 500 K, has been ascribed by us to the mobility of oxygen in niobium. The fitted activation energy amounts to $E_O^M = 1.2(\pm 0.1)$ eV, $D_{0,O} = 8\times10^{-6}$ m^2 s^{-1}, and an oxygen concentration of 30 appm. This activation energy corresponds well with the literature value of oxygen migration energy being 1.16 eV [20]. Also Kögel et al. reported decoration of defects by oxygen [21]. The annealing stage cannot be ascribed to vacancy migration, as vacancies are mobile in niobium already at room temperature [22-25]. Therefore it is proposed that multiple oxygen atoms can decorate the vacancies or helium-vacancy complexes in niobium so that vacancies then act as nucleation centers for growth of oxide precipitates. The effect of oxygen decoration is a reduced trapping of helium. Similarly in another experiment, it was observed that reduction reactions of the type HeV + I → He take place in as-irradiated niobium, but little reduction seems possible after annealing to 630 K. Apparently the defect has been modified by oxygen trapping.

The second annealing stage, at 750 K, is ascribed to VO dissociation. The stage was fitted with a first order desorption process with a dissociation energy of 2.0(±0.15) eV and attempt frequency 10^{13} s^{-1}.

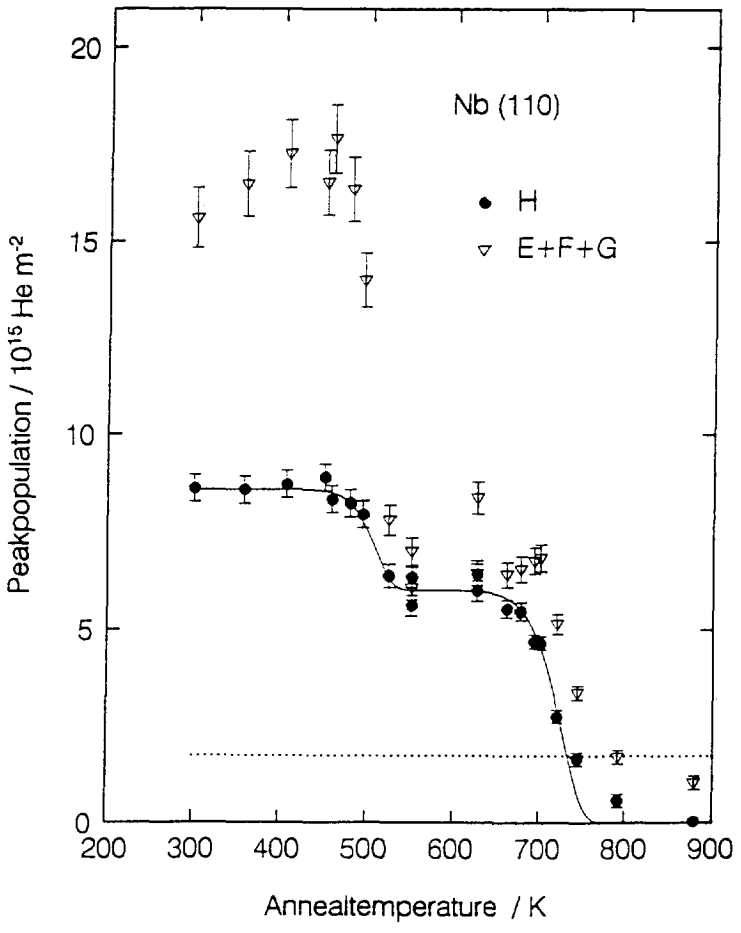

Fig. 7.11. Peak populations of the peaks H and E+F+G versus the annealing temperature for niobium pre-irradiated with $1x10^{16}$ He^+ m^{-2}, ion energy 3 keV. After annealing the defects have been probed with $1x10^{17}$ He^+ m^{-2} at 100 eV ion energy. The solid curve is the result of model calculations including the effect of oxygen mobility at 500 K and OV dissociation at 700 K. The dotted line indicates the H-peak population when there is neither annealing nor the addition of any helium probe doses.

7.5 Conclusions

The thermal desorption experiments presented in this work have led to the following new insights into helium behaviour in vanadium and niobium. An overview of defect reactions of self-interstitial atoms, vacancies, oxygen, nitrogen and helium in vanadium and niobium and THDS peaks is given in table I.

i) The helium desorption spectra are clearly different from spectra obtained for impurity free molybdenum and tungsten [13,14]. Helium desorption from vacancy type defects in vanadium is observed at a relatively low temperature: 0.25 T_m. Similar behaviour is observed in the case of niobium. Also the wide variety of peaks is not observed in other metals. The effects are ascribed to strong binding of impurities at the defects.

ii) At room temperature created vacancies are trapped by impurities (C,O,N) present in vanadium.

iii) Vacancy type defects in vanadium can be annihilated by introducing self-interstitials using 50 eV argon surface bombardment.

iv) Helium filling of the vacancy type defect results in helium assisted trap mutation: $HeVX+He_n \rightarrow He_{n+1}XV_2 + I$ (X = impurity , V = vacancy, I = self interstitial).

v) Helium implantation experiments at low temperatures in vanadium show vacancy migration around 215 K. A diffusion coefficient of $D_V = 1x10^{-7} \exp\{-0.47(\pm0.02)[eV]/kT\}$ m^2s^{-1} was deduced from the measurements, with an assumed oxygen concentration of 20 appm. The value of 0.47 eV for the migration energy compares well with the calculated or extrapolated values in the literature [12,14]. But it disagrees with Janot et al. [8] and Maier et al. [9].

vi) As a result of the inhibition of HeXV formation, suppression of helium trapping at irradiation temperatures higher than 550 K was observed.

vii) The dissociation $XV \rightarrow X + V$ in vanadium takes place at temperatures ranging from 350 K to 550 K; this causes impurity delayed vacancy migration.

viii) Neon, argon and krypton desorb at temperatures around 1000 K. The desorption peaks could be fitted with a first order desorption transient, but energies did not agree with those obtained with RELAX calculations. This is attributed to the involvement of impurities.

ix) In niobium, oxygen decoration of vacancies ocurred prior to helium release. The migration energy and diffusion coefficient of oxygen were fitted to be $E_O^M = 1.2(\pm0.1)$ eV, $D_{0,O} = 8x10^{-2}$ m^2 s^{-1}. These data compared well with literature values.

Table I. Defect reactions of self-interstitial atoms, vacancies, oxygen, nitrogen and helium in vanadium and niobium. Helium desorption peaks corresponding with the reactions are indicated.

	Vanadium			Niobium		
Reaction	peak	T/K	E^D/eV	peak	T/K	E^D/eV
$I \rightarrow I_{mobile}$		~8			~10	
$He \rightarrow He_{mobile}$		<100	0.16		<100	
$HeX \rightarrow He + X$ (X = I,O,N,C)	$L_{1,2,3,4}$	100-300		$L_{1,2,3}$	100-300	
$V \rightarrow V_{mobile}$		200	0.47(7)		280	0.545(5)
$V_{mobile} + O \rightarrow OV$		>200			>280	
He-surface desorption	S_1 S_2	<400 620		S_2	550	
$OV \rightarrow O+V_{mobile}$		450			700	1.90(15)
$O \rightarrow O_{mobile}$		>480	1.3		>450	1.17(5)
$HeV+O_{mobile} \rightarrow HeOV$		480-600				
$He_nO_mV+O_{mobile} \rightarrow He_nO_{m+1}V$					450-550	
$HeOV + m\ O_{mobile} \rightarrow HeO_{m+1}V_{k+1} + k\ I$		480-600				
$He_nO_2V \rightarrow He_{n-1}OV+O_{mobile}$ $He_nOV \rightarrow He_{n-1}OV+He\ (n \geq 2)$				E,F,G	500-680	
$HeOV \rightarrow OV + He$ $HeNV \rightarrow NV + He$	1 2	540 580	1.40(15)	H	740	1.90(15)
$He_nO_mV_k \rightarrow He_{n-1}O_mV_k + He$	3-12	600-1200		I,J,K	750-1200	
He desorption from surface oxide	S_3	1200-1500		S_3	1200-1500	

Literature

[1] S. Yano, M. Tada and H. Matsui, J. Nucl. Mater. **179-181** (1991) 779.

[2] B.A. Loomis and D.L. Smith, J. Nucl. Mater. **191-194** (1992) 84.

[3] H.M. Chung and D.L. Smith, J. Nucl. Mater. **191-194** (1992) 942.

[4] L.K. Mansur, E.H. Lee, P.J. Maziaz and A.P. Rowcliffe, J. Nucl. Mater. **141-143** (1986) 633.

[5] M.B. Lewis, J. Nucl. Mater. **152** (1988) 114.

[6] R. Vassen, H. Trinkaus and P. Jung, Phys. Rev. **B44** (1991) 4206.

[7] P. Jung, in Diffusion Processes in Nuclear Materials, ed R.P. Agarwala (Elsevier, Amsterdam, The Netherlands) 236.

[8] C. Janot, B. George, P. Delcroix, J. Phys. F **12** (1982) 47.

[9] K. Maier, M. Peo, B. Saile, H.E. Schaefer and A. Seeger, Phil Mag. **A40** (1979) 701.

[10] Calculation by H. Schultz, Point Defects and Defect Interactions in Metals (1982) 183, edited by J. Takamura, M. Doyama and M. Kiritani.

[11] Extrapolation by M. Tietze, S. Takai, I.A. Schwirlitz and H. Schultz, ib idem, 265.

[12] Extrapolation by F. Philippe, B. Saile and K. Urban, ib idem, 261.

[13] A. van Veen, Mater. Sci. For. **15-18** (1987) 3.

[14] W. Th. Buters, J.H. Evans, A. van Veen and A. van den Beukel, Defect and Diffusion Forum **57-58** (1988), 75.

[15] G. Hörz, H. Speck, E. Fromm and H. Jehn, Physics Data **5-7** (1981).

[16] R.H.J. Fastenau, L.M. Caspers and A. van Veen, Phys. Stat. Sol. (a) **34** (1976) 277.

[17] R. Rebonato, D.O. Welch, R.D. Hatchers and J.C. Bilello, Philisophical Magazine **A55** (1987) 655.

[18] L.M. Caspers, A. van Veen and T.J. Bullough, Radiation Effects **78** (1983) 67.

[19] A. Van Veen, W.Th.M. Buters, G.J. van der Kolk, L.M. Caspers, J. Nucl. Instr. Meth. **194** (1982) 485.

[20] E. Fromm and E. Gebhardt, Gase und Kohlenstoff in Metallen (Springer Verlag, Berlin, 1976).

[21] G. Kögel, P.Sperr, J. Störmer and W. Triftshäuser, Condens. Matter

5 (1993) 3987.

[22] H. Schultz, in Point Defects and Defect Interactions in Metals, eds. J. Takamura, M. Doyama and M. Kiritani (1977) 183.

[23] K. Faber and H.Schultz, Rad. Eff. **31** (1977) 157.

[24] P. Hautojärvi, in Mat. Sci. For. **15-18** (1987) 81.

[25] P. Hautojärvi, H. Huomo, M. Puska and A. Vehanen, Phys. Rev. **B32** (1985) 4326.

Hydrogen and helium in selected fusion reactor materials

Summary

In this thesis selected fusion reactor materials are studied mainly with the aid of thermal gas desorption spectrometry and simulations using diffusional release of hydrogen. Surface effects, point defects and the onset of microstructural evolution in specific materials are studied. Regarding the experimental method, the development of the hydrogen probe technique is considered in this thesis.

In chapter 1 an overview is given of the materials used at present in fusion devices of candidate materials for the International Thermonuclear Experimental Reactor (ITER). The overview focuses on the metals tungsten, beryllium and vanadium, investigated in this thesis. Niobium was used for comparison with vanadium as a member of the group 5 elements. Also, the purpose of the development of the deuterium probe within the gas desorption technique is described.

Chapter 2 deals with experimental details. The gas desorption technique in ultra high vacuum systems and Auger Electron Spectroscopy (AES) are extensively discussed. Other techniques such as positron annihilation (PA) and neutron depth profiling (NDP) are briefly introduced. The sample preparation of the tungsten and vanadium monocrystals and the beryllium foils concludes this chapter.

Diffusion and rate theory are discussed in chapter 3. The influence of the concentration of microcavities and its depth dependence on the thermal desorption of hydrogen from these cavities is simulated. Also, the effects of surface recombination and of the hydrogen pressure in the microcavities on the thermal desorption are studied.

Hydrogen, nitrogen and carbon interactions with point-defects in tungsten are the subject of chapter 4. Experiments using the thermal desorption technique showed that the problem of surface (re-) trapping of deuterium can be overcome successfully by covering the surface with oxygen. Experimental results simulated with simplified rate calculations yield deuterium binding energies to the surface of 0.6 eV for the reconstructed surface and 0.48 eV for the unreconstructed surface). The

binding energy of deuterium to a vacancy is found to be 1.43±0.02 eV. The attempt frequencies can be found in table 1 of chapter 4. It turns out that deuterium release from tungsten is dominated by deuterium vacancy dissociation, as opposed to surface-recombination dominated release. The deuterium capture of the crystal after bombardment with 1 keV deuterium ions shows trapping behaviour which increases with oxygen coverage. This can be ascribed to recoil implantation: deuterium is captured by vacancies created by the H→O→W collission process. Nitrogen and carbon dissociation from vacancies are studied with the aid of thermal helium desorption and are found to require 2.7 eV and 2.9 eV, respectively.

In chapter 5, vacancy cluster growth in tungsten is studied with the aid of thermal desorption and positron annihilation. Results obtained with both techniques and atom embedding calculations show that vacancy cluster growth takes place in three stages. Finally, the clusters disappear due to annealing. When tungsten crystals are irradiated with 30 keV deuterium ions, vacancies are created. At 600 K, vacancies become mobile (stage one) and form V_{4-10}; at 1000 K (stage two) these clusters dissociate in favour of the formation of V_{11-16}; at 1400 K, the third stage, these medium size clusters coalesce to form V_{40-60} vacancy clusters. At 1700 K the vacancy-clusters are annealed out, or at least they become invisible to deuterium and positrons. Nitrogen filling of the V_{40-60} clusters did not change the deuterium desorption characteristics, only the amount of the deuterium probe trapped was influenced. The deuterium interaction with helium bubbles in tungsten is also described in chapter 5. Helium bubbles were created by a high dose of 3 keV helium ion irradiation of the crystal, which was subsequently annealed to 1500 K. Deuterium desorption took place in the temperature range from 400 K to 800 K. Helium bubbles could be annealed out at 2200 K.

In chapter 6 the behaviour of helium in beryllium is explored. In the case of a low concentration HeV type defects, helium is released by a thermal vacancy assisted diffusion mechanism (V_{th} + HeV → HeV_2). At higher implantation energies (30 KeV) small helium filled vacancy clusters are created. Upon heating, PA and NDP results indicated that helium bubbles nucleate and increase in size, starting at 550 K, until helium is released at T > 950 K. Scanning electron micrographs of the samples heated to 1075 K showed extensive swelling of the beryllium surface to ten times its original thickness. Rather than to go into resolution and to permeate to the surface, helium remains trapped inside the growing bubbles

until these penetrate the surface.

The group 5 elements vanadium and niobium are the subjects of chapter 7. The results indicate that impurities (probably oxygen) play an important role in the helium interactions with point defects. In both vanadium and niobium decoration of vacancies by oxygen invokes helium desorption to take place at relatively low temperatures 0.25 Tm, when compared to other BCC metals as molybdenum and tungsten (0.4 T_m). Fitting of the results reveals an activation energy of the vacancy migration of 0.47 eV, and 0.55 eV and a diffusion coefficient D_0 of $1x10^{-7}$ m^2s^{-1} and $8x10^{-6}$ m^2s^{-1} in the case of vanadium and niobium respectively. Impurity delayed vacancy migration is found in both metals. Furthermore, vacancies could be annihilated by introduction of self-interstitials. As a result of the inhibition of vacancy type defect formation at irradiation temperatures above 550 K, helium trapping in vanadium is suppressed.

It can be concluded that the hydrogen probe technique has proven to be successful as (i) a tool for observing subsurface defects, (ii) for deuterium point defect interaction studies and (iii) in observing annealing behaviour of single crystalline tungsten containing voids. It was succesful as a nondestructive probe, taking advantage of the lower temperature desorption of deuterium compared to the dissociation of vacancy clusters. The probe can therefore be used as a valuable complement (where appropriate) to the better established use of helium as a probe in metals.

What is the importance of the results on the selected materials to the fusion community ? In order to use tungsten parts facing the plasma in a fusion reactor it is important that those parts periodically can be annealed to high temperatures (~1700 K). Defect accumulation in tungsten can then be suppressed. For beryllium, severe problems will occur due to the immobility of helium at relatively high temperatures (<600 K). Therefore it is expected that defect accumulation can not be avoided while beryllium is facing the plasma. Thus, beryllium can be used in a fusion environment, because of its properties as mentioned in chapter 1, but beryllium erosion must be accepted. Concerning defect accumulation in vanadium, it can be advised, as in the case of tungsten, to repeatedly anneal the vanadium parts to high temperatures (>700K). That would be sufficient to suppress defect evolution.

Waterstof en helium in geselecteerde fusiereactor-materialen

Samenvatting

In dit proefschrift worden fusiereactor-materialen, die van belang zijn voor de ontwikkeling van de kernfusietechnologie, bestudeerd met een aantal defectanalysetechnieken, waarvan thermische gasdesorptie spectrometrie de belangrijkste plaats inneemt. In aanvulling op de bestaande heliumdesorptie-techniek wordt de toepassing van waterstof als sonde voor het aantonen van defecten verder ontwikkeld en beschreven in dit proefschrift. Oppervlakte-effecten, puntfouten en het ontstaan van microholten en gasdefectagglomeraties zijn onderzocht in specifieke materialen. De kinetiek van gas-defect interacties wordt beschreven door middel van numerieke modellen voor diffusie, vangst en desorptie.

In hoofdstuk 1 wordt een overzicht gegeven van de gebruikte materialen in de huidige fusiereactoren en van kandidaat materialen voor de nog te bouwen internationale tokamak (ITER). Het overzicht is toegespitst op de metalen wolfraam, beryllium en vanadium, die in dit proefschrift aan bod komen, niobium is gebruikt als vergelijkingsmateriaal voor vanadium. V en Nb zijn beide groep 5 elementen. Ook het doel van de toepassing van de deuteriumsonde voor het desorptieonderzoek wordt beschreven.

Experimentele details worden behandeld in hoofdstuk 2. Zo worden de gasdesorptie-techniek in een hoog-vacuum systeem en Auger electronen spectroscopie (AES) uitvoerig toegelicht. Andere technieken als positronen-anihilatie (PA) en neutronen diepteprofilering (NDP) worden kort geïntroduceerd. Het hoofdstuk wordt afgesloten met de beschrijving van de preparatie van wolfraam - en vanadiumkristallen alsmede berylliumfolies.

Het modelleren van de waterstofdesorptie uit metalen met defecten wordt beschreven in hoofdstuk 3. Hierbij wordt de beïnvloeding van de waterstofdesorptie door de diepteverdeling en de concentratie van de microholten gesimuleerd. Ook de effecten van de oppervlakterecombinatie en de waterstofdruk in de microholten op het waterstofdesorptie spectrum

worden behandeld.

Waterstof-, stikstof- en koolstofinteracties met puntdefecten in wolfraam zijn de onderwerpen van hoofdstuk 4. Er wordt vastgesteld dat het probleem voor de waterstofdesorptie-techniek, teweeggebracht door adsorptie van waterstof aan het oppervlak, voorkomen kan worden door de bedekking van het oppervlak met zuurstof. De bindingsenergieën van waterstof aan het oppervlak (0.6 en 0.48 eV voor een gereconstrueerd en ongereconstrueerd oppervlak respectievelijk) en van waterstof aan een vacature (1.43±0.02 eV) konden worden bepaald door middel van simulaties van de experimentele resultaten. De sprongfrequenties zijn terug te vinden in tabel I van hoofdstuk 4. Verder kon worden vastgesteld dat waterstofdesorptie van wolfraam wordt gedomineerd door waterstof-vacature dissociatie, in tegenstelling tot oppervlakte-gedomineerde desorptie. De deuteriumvangst van het kristal na beschieting van het kristal met 1 keV deuteriumionen vertoont een toename met de zuurstofbedekking van het oppervlak. Dit duidt op het aanmaken van vacatures door het verplaatsen van een wolfraamatoom via een zuurstofatoom (het H→O→W botsingsproces). Stikstof- en koolstofdissociatie van vacatures is bestudeerd met behulp van heliumdesorptie. Het bleek dat de processen respectievelijk 2.7 en 2.9 eV vergen.

Vacatureclustergroei wordt bestudeerd in hoofdstuk 5 met behulp van thermische desorptie en positronenannihilatie. Resultaten, behaald met beide technieken en met 'atom embedding' berekeningen, geven aan dat vacaturecluster-groei tijdens uitgloeien plaatsvindt in drie stappen. In een laatste stap verdwijnen de clusters. Vacatures worden aangemaakt door bestraling van wolfraam met 30 keV deuteriumionen. Bij 600 K worden vacatures mobiel (stap één) en vormen $V_{4\text{-}10}$'s (clusters van 4 tot 10 vacatures). Bij 1000 K (stap twee) dissociëren deze clusters, waardoor $V_{11\text{-}16}$'s worden aangemaakt. Bij 1400 K, de derde stap, verdwijnen deze $V_{11\text{-}16}$'s ten gunste van $V_{40\text{-}60}$'s. Bij 1700 K konden de grootste clusters worden uitgegloeid, of werden zij in ieder geval onzichtbaar voor de gebruikte technieken. Het vullen van de $V_{40\text{-}60}$-clusters gaf geen verandering te zien in het waterstofdesorptie spectrum. Alleen de hoeveelheid van de gevangen waterstof werd beïnvloed. De deuteriuminteractie met heliumbellen in wolfraam wordt eveneens beschreven in hoofdstuk 5. De heliumbellen werden aangemaakt door middel van een bestraling van het

kristal met een hoge dosis van 3 keV helium ionen. Het kristal werd vervolgens verhit tot 1500 K. Deuteriumdesorptie vond plaats in het temperatuurgebied van 400 tot 800 K. De heliumbellen werden uitgegloeid door een verhitting van het kristal tot 2200 K.

In hoofdstuk 6 wordt het gedrag van helium in beryllium behandeld. Bij een helium bestraling van berylliumfolies met een lage dosis (10^{17} He m^{-2}) en lage energie (< 3 keV) gaven thermische desorptiespectra aan dat helium het folie verlaat door een diffusieproces waarbij thermische vacatures een rol spelen. (V_{th} + HeV $\rightleftharpoons$ HeV_2). Bij hogere implantatie-energieën (30 keV) worden kleine met helium gevulde vacatureclusters gecreëerd. PA - en NDP resultaten tonen dat heliumbellen ontstaan tijdens de verhitting, te beginnen bij 550 K, totdat helium het folie verlaat bij 950 K. Rasterelectronenmicroscopie-opnamen van de berylliummonsters die verhit waren tot 1075 K, gaven een enorme zwelling te zien van het berylliumoppervlak tot 10 keer de originele (bestraalde) dikte. In plaats van op te lossen en via het oppervlak te verdwijnen blijft het helium gevangen in de bellen totdat die aan het oppervlak verschijnen.

De groep-5 elementen vanadium en niobium zijn de onderwerpen van hoofdstuk 7. De resultaten geven aan dat onzuiverheden (waarschijnlijk zuurstof) een belangrijke rol spelen bij de heliuminteracties met puntdefecten. Zowel bij vanadium als niobium zorgt de zuurstofdecoratie van de vacatures voor verlaging van de heliumdesorptietemperatuur tot een kwart van de smelttemperatuur. Ter vergelijking, heliumdesorptie uit andere BCC-metalen als molybdeen en wolfraam vindt plaats bij 0,4 van de smelttemperatuur. Vacature-migratie energieën van 0,47 eV en 0,55 eV met een diffusiecoëfficient D_0 van $1x10^{-7}$ m^2s^{-1} en $8x10^{-6}$ m^2s^{-1} voor respectievelijk vanadium en niobium zijn gevonden door het aanpassen van een model aan de heliumdesorptie spectra. Door onzuiverheden vertraagde vacature-migratie werd gevonden voor beide metalen. Verder konden vacatures worden geannihileerd door introductie van zelf-interstitiëlen. Door het afwezig zijn van vacature-type defecten, bij bestralingstemperaturen hoger dan 550 K, kan heliumvangst in vanadium worden onderdrukt.

Er kan geconcludeerd worden dat de waterstofdesorptie techniek een succesvolle techniek is (i) als gereedschap voor het observeren van onderhuidse defecten, (ii) voor deuterium-puntdefect interactie studies en

(iii) van het observeren van het uitgloeigedrag van vacatureclusters in wolfraamkristallen. Waterstof kan verder succesvol worden gebruikt als een niet-destructieve sonde door het toepassen van waterstofdesorptie uit monsters bij temperaturen die relatief laag zijn in vergelijking met de dissociatietemperatuur van vacatureclusters. De waterstofsonde kan daarom worden toegepast als een niet-destructieve methode voor defectonderzoek. Als zodanig is het een waardevolle aanvulling op de bestaande helium-desorptie-techniek in metalen.

Hoe belangrijk zijn de behaalde resultaten met de geselecteerde materialen voor de kernfusietechnologie-gemeenschap ? Voor het toepassen van wolfraamonderdelen in een fusiereactor is het belangrijk dat die periodiek uitgegloeid kunnen worden tot hoge temperaturen (~1700 K). Op die manier kan accumulatie van defecten voorkomen worden. Bij gebruik van beryllium kunnen ernstige problemen ontstaan door de immobiliteit van helium bij relatief hoge temperaturen (<600K). Daarom lijkt accumulatie van defecten onvermijdelijk wanneer beryllium blootgesteld wordt aan het fusieplasma. Door zijn eigenschappen zal beryllium weliswaar kunnen worden toegepast in een fusiereactor, erosie van het beryllium zal moeten worden geaccepteerd. Om defectaccumulatie te voorkomen in het geval van vanadium wordt geadviseerd om, net als met wolfraam, de vanadium-onderdelen regelmatig te verhitten tot hoge temperaturen (>700 K). Dat zal voldoende zijn om defect-evolutie te voorkomen.

Nawoord

Hier wil ik een ieder bedanken die heeft bijgedragen bij het totstandkomen van dit proefschrift. Allereerst bedank ik Prof. dr. ir. H. van Dam voor de gelegenheid die hij me bood voor het verrichten van promotiewerk in de vakgroep Reactorfysica bij het Interfacultair Reactor Instituut.

Tevens bedank ik prof. dr. A. van Veen voor zijn dagelijkse begeleiding en als grote inspiratiebron voor het experimentele werk.

Dr. John Evans ben ik dank verschuldigd voor zijn commentaar in de conceptversie van het proefschrift.

Bob Heijenga, Jan de Roode en Kees Westerduin bedank ik voor hun steun bij het in orde brengen van vacuum-apparatuur. In dat opzicht zal ik de douche-actie van de HDS3-ketel niet vergeten. Henk Schut bedank ik voor zijn VEP-activiteiten en de prettige omgang die ik met hem heb gehad. Bij het programmeren in Fortran heeft Maurits IJpma me goed ondersteund. Karl Roos bedank ik voor de technische uitvoering van ontwerptekeningen. Rini Purmer en Sonja Jobse bedank ik voor de goede samenwerking en het leuke contact.

De studenten Arjen Dijksman, Maarten Clement, Mathijs de Moor en Gert-Jan Busker hebben bijgedragen aan mijn onderzoek. Hun inzet en enthousiasme heb ik zeer gewaardeerd. Met Mathijs in het bijzonder heb ik nogal wat vrije uren doorgebracht met voetballen, fietsen en hardlopen.

Het bestuderen van het boek 'Solid State Physics' van Ashcroft en Mermin gezamenlijk met o.a. Tom Piters en Adrie Bos was nuttig en een waar genoegen.

De discussies over uiteenlopende onderwerpen met Rudi Hakvoort en Hans Filius heb ik als prettig ervaren.

De leden van de werkgroep 'Atomic Defect Simulations', die bestond uit Tom van Veen, Maurits IJpma, Rien Breeman, Dirk Peter van der Werf, Jeff de Hosson, Frits Pleiter en Alfons Molenbroek wil ik bedanken voor de kennisoverdracht met betrekking tot 'atom embedding'-modellering.

Van de RIVM-ers wil ik met name de leiding van het Laboratorium voor Stralingsonderzoek (LSO) bedanken voor hun begrip voor mijn promotiewerk.

Mary-Anne, jou bedank ik in het bijzonder voor de steun en geduld

tijdens al die jaren. Voor mijn promotiewerk heb ik menig verlofdag verbruikt, wat ten koste ging van onze gezamenlijke tijd met Daan. Ook mijn ouders wil ik bedanken voor hun goede zorg en betrokkenheid.

Curriculum Vitae

De schrijver van dit proefschrift werd geboren op 3 april 1965 te Veendam. Het VWO-diploma werd behaald in 1983 aan het Oosterlicht College gevestigd te Utrecht. In datzelfde jaar werd begonnen met de studie Natuurkunde aan de Rijksuniversiteit Utrecht. Na het uitvoeren van experimenteel werk bij de vakgroep Moleculaire Biofysica werd in 1989 het doctoraaldiploma gehaald. Met ingang van maart 1990 is begonnen met het onderzoek beschreven in dit proefschrift. Per september 1994 is hij met zijn werkzaamheden begonnen bij het RIVM. Deze zijn achtereenvolgens verricht bij de laboratoria voor Stralingsonderzoek (LSO), Luchtonderzoek (LLO) en Afvalstoffen en Emissies (LAE).